Preparation and characterisation of a magnetomechanical system

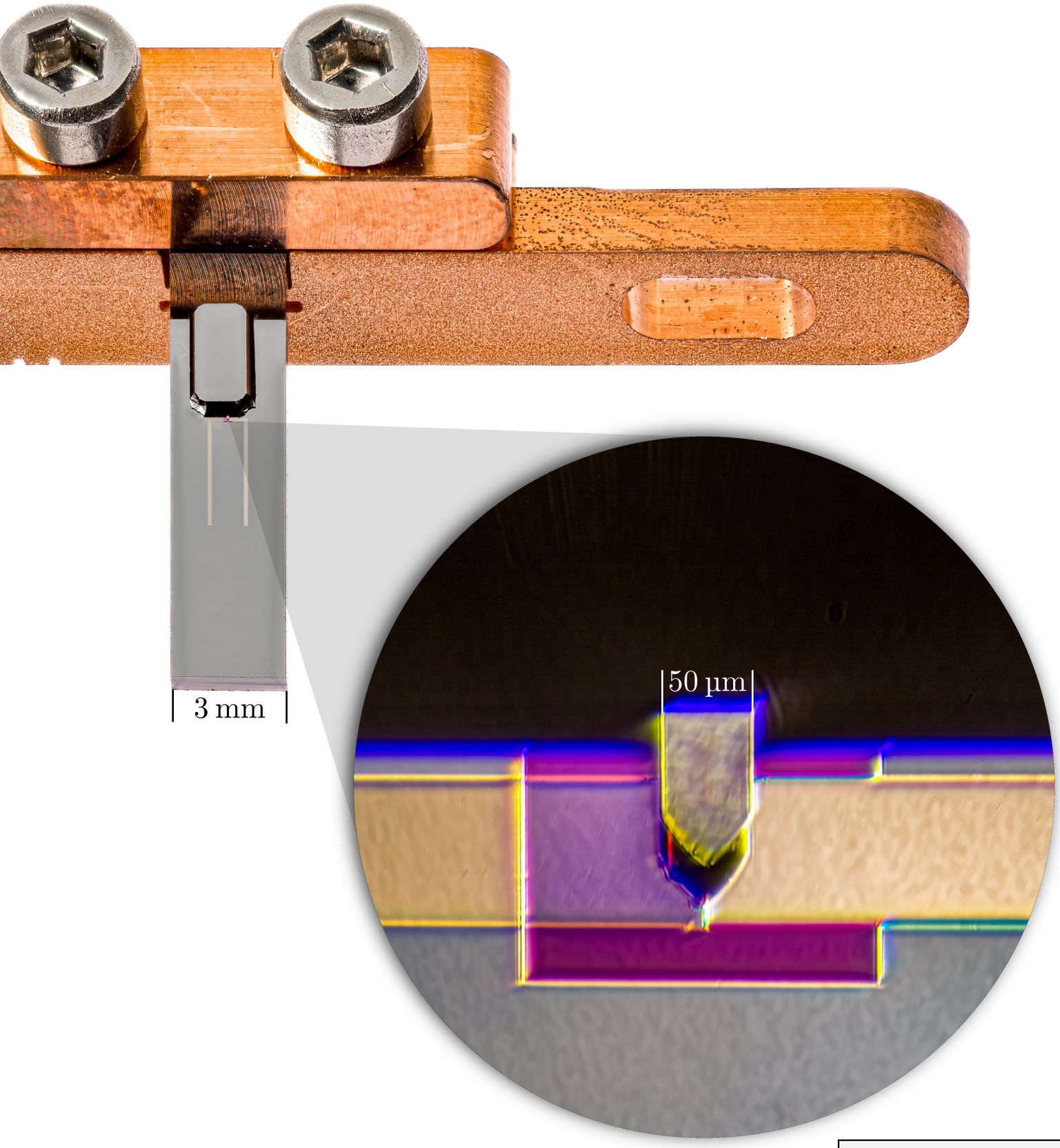

Christian Dejaco

universität innsbruck

Preparation and characterisation of a magnetomechanical system

Christian DEJACO, 11808490

Innsbruck, July 2025

Master thesis

submitted to the Faculty of Mathematics, Computer Science, and Physics of the University of Innsbruck in partial fulfilment of the requirements for the degree of

Master of Science (MSc)

supervised by:

Univ. Prof. Dr. Gerhard KIRCHMAIR

Institute of Experimental Physics
Faculty of Mathematics, Computer Science, and Physics

Abstract

The approach of inductively coupling the centre of mass motion of an AFM cantilever to a SQUID microwave cavity allows for strong, in-situ tunable optomechanical coupling [1–5]. With such a system, optomechanical cooling at the single microwave photon level has been demonstrated [6]. Furthermore, it was shown that the SQUID's intrinsic Kerr nonlinearity can be utilised to enhance backaction cooling in the unresolved-sideband regime [7–9]. However, the sideband resolved regime, which allows ground state cooling and exploration of macroscopic quantum effects [10], remained unattainable with the microwave cavity quality factor of only about $5{\cdot}10^3$.

In this thesis, a new batch of frequency-tunable niobium SQUID cavities with intrinsic quality factors of up to $35{\cdot}10^3$ was characterised. A fitting routine for the observed hysteretic frequency tuning behaviour was worked out to determine the SQUID participation ratio and the flux shielding parameter. Fitting high-power scattering data with an implemented routine allows reliable extraction of the Kerr constant. The obtained parameters of the nominally identical samples show a significant spread, with SQUID participation ratios varying between 0.27 % and 1.82 %, shielding parameters from 0.15 to 0.36, and Kerr constants at the flux sweetspot ranging from 8 Hz to 250 Hz.

Despite the initial improvement in cavity quality factor, the losses introduced upon mounting an AFM cantilever with a magnetic particle above the SQUID still place our system in the sideband unresolved regime. We find that the doped silicon cantilever chip and the magnetic particle with a bias field of up to 100 mT are the main contributions to loss. These limitations currently still preclude access to the sideband resolved regime.

We have considerably streamlined the assembly of such magnetomechanical devices. A mounting stage custom-designed by L. F. Deeg significantly improved cantilever alignment and survival rate and increased the yield of devices with adequate optomechanical coupling. We measured a mechanical signature on four out of five prepared samples. We observe variations in mechanical and cavity properties with thermal cycling and discuss possible explanations. Despite challenges with thermalisation of the mechanical mode after moving the setup to a different laboratory, backaction cooling on a new sample is demonstrated with a single-photon coupling strength of up to 0.24(3) kHz.

To isolate the mechanical mode from vibrations of the pulse tube cooler, the experiment is suspended on a spring within the cryostat [9]. By implementing a mechanical heat switch and annealed copper braids, thermalisation of the suspended setup was improved, enabling faster thermal cycling.

Kurzfassung

Der Ansatz, die Bewegung eines AFM-Kantilevers induktiv mit einem SQUID Mikrowellenresonator zu koppeln, ermöglicht starke, in-situ verstellbare optomechanische Kopplung [1–5]. Mit einem solchen System wurde optomechanisches Kühlen im Ein-Photon-Regime demonstriert [6]. Zudem ließ sich zeigen, dass die intrinsische Kerr-Nichtlinearität des SQUIDs effizienteres Kühlen bei nicht aufgelösten Seitenbändern ermöglicht [7–9]. Das Auflösen der Seitenbändern, was Kühlen in den Grundzustand sowie Untersuchen makroskopischer Quanteneffekte erlauben würde [10], war jedoch mit dem Mikrowellenesonator Gütefaktor von etwa $5{\cdot}10^3$ nicht möglich.

In dieser Arbeit wurde eine neue Charge frequenzabstimmbarer Niob SQUID Resonatoren mit Gütefaktoren von bis zu $35{\cdot}10^3$ charakterisiert. Zur Bestimmung des SQUID Beteiligungsverhältnis und des magnetischen Abschirmparameters wurde eine Fitroutine für das hysteretische Frequenzabstimmverhalten entwickelt. Durch Fitten von Streuparamtern bei hohen Signalleistungen mit einer implementierten Routine, kann die Kerr-Konstante zuverlässig bestimmt werden. Die erhaltenen Paramter der nominell identischen Resontatoren weisen eine signifikane Streung auf, mit SQUID Beteiligungsverhältnissen zwischen 0.27 % und 1.82 %, Abschirmparametern von 0.15 bis 0.36 sowie Kerr-Konstanten am Sweetspot zwischen 8 Hz und 250 Hz.

Trotz der anfänglichen Verbesserung des Gütefaktors führen Mikrowellenverluste, nach dem Montieren eines Kantilevers mit magnetischem Partikel über dem SQUID, dazu, dass in unserem System die Seitenbänder weiterhin nicht aufgelöst werden können. Wir stellen fest, dass ein Großteil dieser Verluste durch den dotierten Silizium-Kantileverchip sowie das magnetische Partikel, welches ein Feld von bis zu 100 mT am Ort des SQUIDs erzeugt, entstehen.

Die Präparierung solcher Proben konnte erheblich vereinfacht werden. Eine von L. F. Deeg entwickelte Montagevorrichtung verbesserte sowohl die Ausrichtung als auch die Überlebensrate der Kantilever deutlich und erhöhte die Ausbeute an Proben mit hinreichend optomechanischer Kopplung. In vier von fünf präparierten Proben konnte ein mechanisches Signal gemessen werden. Nach wiederholtem Aufwärmen beobachten wir Veränderungen der mechanischen Eigenschaften des Kantilevers sowie Änderungen am Mikrowellenresonator und diskutieren mögliche Ursachen. Trotz Herausforderungen bei der Thermalisierung der mechanischen Mode nach Verlegen des Kryostaten in ein anderes Labor, konnte optomechanisches Kühlen anhand einer der neuen Proben mit einer Kopplungsstärke von bis zu 0.24(3) kHz demonstriert werden.

Zur Isolierung der mechanischen Mode von Vibration wird das Experiment im Kryostaten an einer Feder aufgehängt [9]. Durch die Implementierung eines mechanischen Wärmeschalters und das Verwenden von wärmebehandelten Kupfergeflechten konnte die Thermalisierung des isolierten Systems verbessert und ein schnelleres Abkühlen des Kryostaten ermöglicht werden.

Acknowledgements

First and foremost, I would like to thank **Gerhard Kirchmair** for supervising this thesis, the weekly mechanics project meetings and for always bringing such great enthusiasm. You are an excellent supervisor, and I'm looking forward to working and learning with you as a PhD student in your group.

Furthermore, I want to thank the members of the mechanics team, **Lukas Deeg**, **Bhargava Thyagarajan**, and **Raamamurthy Sathyanarayanan**, who were directly or indirectly involved in everything presented in this thesis.

A special thanks to **Lukas Deeg**, the last person standing before the new generation of team members (including me) joined the project, after **David Zoepfel**, **Christian Schneider**, and **Mathieu Juan** set up the experimental platform and laid the foundation for the current setup. Lukas introduced us to the project and worked closely with me during every cooldown, measurement and data analysis. Your idea for the nonlinear circle fit routine became a smooth and reliable tool, and your simple yet very effective cryogenic suspension setup and cantilever mounting stage pushed the project forward. I hope I may still ask you for one of your creative, elegant and fast solutions after you graduate!

To **Bhargava Thyagarajan**, thank you for all your help in the lab, for carefully reading this thesis and your helpful comments and discussions (especially your uncanny ability to spot German phrasing in my English!). I've learned a lot from you. Your deep knowledge of cryostats is inspiring. I'm happy to have you as a postdoc and look forward to more hikes in the mountains around Innsbruck and trips to Baggersee!

Raamamurthy Sathyanarayanan, the go-to person for anything that needs to be simulated. Together with Bhargava, you took on the fabrication of the next generation of microwave cavity devices. Thanks for organising and being the game master of my first D&D session, a world you introduced some of us to!

Thanks to our theory collaborators, **Nicolás Díaz-Naufal** and **Anja Metelmann**, who developed the nonlinear cooling theory and now, together with their newest team member **Gustavo Kufatty**, support us in better understanding our experiment. Many thanks also to everyone in the **SuperMeQ consortium** for the great collaboration.

I also thank the team from the mechanical workshop, **Andreas Strasser**, **Bernhard Öttl**, **David Arnold** and **Tanja Waidacher** for machining various parts of the setup and introducing me to the student mechanical workshop.

A big thanks to the administrative staff at IQOQI for ordering components and all the work that goes on behind the scenes. Special thanks to **David Jordan**, who manages the lab network, keeps us connected to our instruments, and whose amazing photography skills made the title page and other pictures in this thesis possible.

To all current and previous members of the Kirchmair group:

Julian Daser, who rather randomly became my lab partner in one of the master's lab courses and later led me to join the group for my master's thesis. Looking forward to catching up with the group's fastest hiker, host of epic BBQs, and master of the delicious liquid nitrogen ice cream. **Teresa Hönigl-Decrinis**, who already supervised my bachelor's thesis, and thereby also played an important role in me joining Gerhard's group. **Ian Yang**, for your support, reading my thesis, and providing helpful comments, even after you moved on to Zürich. Most importantly, thank you for the delicious Asian food you prepared for our group dinners. **Vasilisa Usova**, for our ski touring and hiking adventures, and to **Desislava Atanasova**, **Christian Schlager**, **Tanmoy Bera**, **Filip Hudek**, **Deniz Molavali**, **Philipp Straub** and **Niklas Nocker**, thank you all for always being there, whether to answer scientific questions or to join activities after work. The group dynamic is something truly special, with our daily post-lunch coffees, group dinners, and many memorable gatherings beyond work.

An mine besta Kolega us Vorarlberg, **Florian**, **Elias** und **Jarmil**, danke für die gemeinsame Zit abseits vo dr Uni. Hat mi mega gfreut, dassr a zit lang sogär zum Studiera noch Innbruck ko sind und I so o ohne hoam ins schöne Ländle z fahra do was mit euch unterneh han könna.

Ein ganz besonderer Dank gilt meiner Familie, meiner Schwester **Anja**, **Mama** und **Papa**, danke, dass ihr immer für mich da seid. Ohne eure ständige Unterstützung wäre nichts hiervon möglich gewesen. Danke für alles.

Contents

CHAPTER 1

Introduction

One hundred years ago, in 1925, W. Heisenberg laid the foundation of quantum mechanics as it is known today by introducing a formulation based solely on observable quantities [11]. One hundred years later, the United Nations declared 2025 the International Year of Quantum Science and Technology [12]. Over this timespan, quantum mechanics has evolved from a theoretical curiosity into a cornerstone of modern technology.

Today, quantum mechanics forms the foundation of many modern technologies that have become part of our everyday lives. For instance, it explains the microscopic working principle of semiconductor components, such as transistors or LEDs, which are fundamental components in nearly every electronic device. Lasers, atomic clocks (used in GPS), and magnetic resonance imaging all rely on quantum mechanical principles. However, while the probabilistic laws of quantum mechanics govern the microscopic scale, macroscopic systems typically exhibit deterministic, classical behaviour described by Newton's laws [13].

Schrödinger's famous thought experiment [14], in which a cat is simultaneously dead and alive, highlighted the paradoxes of applying quantum theory to macroscopic objects and raises the question: Can quantum effects, such as superposition [15], be observed in larger systems? Could, for example, a diving board simultaneously be in a superposition of being bent upward and downward?

In practice, the larger an object becomes, the more difficult it is to isolate from its environment. This interaction with the environment leads to decoherence, the process by which quantum states lose their coherence and appear classical [16]. For many years, quantum phenomena were only observed on a microscopic scale, such as for individual electrons, photons or atoms. However, over the past few decades, advances in experimental techniques have extended the reach of quantum mechanics to increasingly larger systems.

A few examples are the collective motion of trapped ions [17], interference of large molecules [18], ultracold quantum gases involving thousands or millions of atoms [19], or quantum interference in superconducting circuits [20, 21]. Extending quantum control to larger systems and preparing nonclassical macroscopic quantum states, such as Fock states or Schrödinger cat states with negativity in their Wigner function or squeezed states that reduce the uncertainty in one quadrature below the vacuum level $\sqrt{\hbar/2}$ [22], is not only of interest for exploring the quantum-classical boundary but also has practical applications. For instance, it allows the development of highly sensitive quantum sensors that surpass classical measurement limits [23].

Prominent platforms in this field are cavity optomechanical systems [10], where radiation pressure couples photons of an electromagnetic field in a cavity to the phonons of a mechanical resonator, allowing precise manipulation of its motional quantum state. As the effective mass of the mechanical mode increases, its resonance frequency decreases. At a fixed temperature, this results in a higher thermal occupation, thereby bringing the system further away from its quantum ground state. Remarkably, it has recently been demonstrated that certain protocols allow for the preparation of quantum superposition states even from a thermally excited initial state [24]. However, most applications of optomechanical systems in quantum metrology or quantum information processing require the occupation of the mechanical mode to be close to its quantum ground state [10].

For mechanical resonators with frequencies in the microwave domain, such ground state cooling is possible through cryogenic refrigeration [25]. For lower frequency mechanical modes, additional cooling is required. Dynamic backaction cooling [26, 27] or active feedback cooling [28, 29] can be used to reduce the thermal occupation. Ground-state cooling has been demonstrated in several optomechanical systems [30–32].

A critical requirement for efficient backaction cooling is that the system operates in the sideband resolved regime, where the mechanical frequency exceeds the cavity linewidth. In this regime, the quantum backaction limit, which sets the minimum achievable phonon occupation, falls below one phonon and thereby enables cooling to the mechanical ground state [26, 33].

In addition to ground-state cooling, many applications of optomechanical systems require strong optomechanical coupling. A high coupling strength enables not only efficient cooling but also fast and precise control of the mechanical quantum state. This allows efficient coherent quantum state transfer between the mechanical resonator and the cavity, which makes optomechanical systems attractive building blocks in quantum information processing, for example, as long-lived quantum memories or to interconnect different, otherwise incompatible, platforms [34].

Several systems have already demonstrated strong coupling [35–37], where the intracavity photon number enhanced optomechanical coupling strength $g = g_0\sqrt{n_\mathrm{c}}$ exceeds both the mechanical and cavity linewidth, a necessary condition for quantum state exchange within the coherence time of the system. However, the even more stringent single-photon strong coupling regime, where the single-photon coupling strength g_0 exceeds both linewidths, has not yet been experimentally demonstrated in cavity optomechanical systems.

Our approach of inductively coupling a micrometre-sized magnetic AFM cantilever to a microwave stripline SQUID cavity is a particularly promising platform to reach this regime. Thanks

to the exceptional sensitivity of the SQUID, this architecture offers among the highest single-photon coupling strengths demonstrated for microwave-domain optomechanical systems [6]. As first proposed in Ref. [1], it has the potential to reach the single-photon strong coupling regime. Additionally, it also allows for in situ tuning of the optomechanical coupling strength with a magnetic bias field.

Due to the relatively large linewidth of the microwave cavity, our system does not yet operate in the sideband resolved regime, which currently prevents ground-state cooling. To address this limitation, this thesis investigates a new batch of SQUID cavities with narrower linewidths, aiming to enter the sideband resolved regime and enable ground-state cooling in future iterations.

This thesis is structured into six chapters:

- In Chapter 1 (this chapter), we motivated the development of cavity optomechanical systems as macroscopic quantum systems and outlined possible applications.
- In Chapter 2, we introduce the theoretical background required for the analysis and interpretation of our experimental observations. We start with the fundamentals of the optomechanical interaction and discuss optomechanical backaction cooling with a linear and a nonlinear Kerr cavity. Then, we introduce microstrip cavities, the physics of Josephson junctions and SQUIDs. We derive theoretical models for the tuning behaviour and Kerr nonlinearity of SQUID cavities. We confirm the derived models using a simulation of the lumped element circuit model. We then show how such cavities can be coupled to a rectangular waveguide, discuss internal loss mechanisms and present models for the scattering parameters in the linear and nonlinear cavity cases. Finally, we discuss the magnetomechanical coupling scheme as well as the modes of a cantilever.
- In Chapter 3, we focus on the characterisation of bare SQUID cavities, before mounting a cantilever. After a brief description of the experimental setup, we analyse the flux tuning behaviour and extract parameters such as the SQUID participation ratio and shielding parameter. We then report on measurements of the external and internal quality factors. Finally, we study the cavity's response at higher probe powers to determine the Kerr constant and compare the results with theoretical predictions.
- In Chapter 4, we describe the preparation of mechanical samples, including the modification of cantilevers with magnetic particles. We discuss how the particles influence the mechanical properties and explain the procedure for mounting cantilevers onto SQUID cavities.
- In Chapter 5, we characterise the prepared magnetomechanical samples. We begin with a description of the additions to the experimental setup required for characterising mechanics samples. This includes a cryogenic vibration isolation setup, for which we analyse limiting factors for thermalisation. We explain the detection principle for the mechanical signal and its calibration. The chapter further explores the effect of the cantilever and magnetic particle on cavity tuning behaviour and quality factor. We analyse mechanical signatures of the different samples, investigate changes in mechanical properties across several cooldowns, with applied magnetic flux bias and temperature. Finally, we present measurements of optomechanical backaction cooling on one of the prepared samples and extract the single-photon coupling strength.

CHAPTER 2

Theoretical background

In this chapter, we summarise the theoretical framework necessary to explain the experimental results of this thesis. We begin with a brief introduction to the field of optomechanics and the fundamentals of the optomechanical interaction. We then describe how the mechanical mode of an optomechanical system can be cooled, and how a nonlinear cavity can enhance this cooling.

Next, we introduce superconducting microstrip cavities and explain how they can be made frequency tunable with external magnetic flux by incorporating a superconducting quantum interference device (SQUID). We derive a model for the tuning behaviour and show that the cavity can be described by a nonlinear Kerr Hamiltonian. We further analyse how the nonlinearity evolves as the flux bias is varied. To confirm the validity of the derived models, we perform simulations of the lumped element circuit model.

We then demonstrate how the microstrip cavities can be coupled to the electric field in a rectangular waveguide and discuss the internal loss mechanisms. The chapter concludes with a discussion of the scattering parameters for the cavities in the waveguide and how these are influenced by the intrinsic Kerr nonlinearity of the SQUID.

Finally, we present the inductive coupling mechanism between the flux-tunable cavities and the mechanical resonator, which in our system is a silicon cantilever with an attached magnetic particle. We discuss the mechanical modes of the cantilever and examine how the attached particle modifies the resonator's mechanical properties.

2.1 Optomechanics

In optomechanics, we study the interaction between electromagnetic radiation and mechanical motion. A comprehensive introduction to the field of optomechanics can be found in Ref. [10]. In the following section and its subsections, key concepts from this reference are summarised.

A typical optomechanical system consists of a Fabry–Pérot cavity, where one of the two mirrors is mounted on a spring. A schematic representation of such a system is shown in Fig. 2.1. The Hamiltonian of the non-interacting systems can be written as

$$\hat{H}_0 = \hbar\omega_c \hat{a}^\dagger \hat{a} + \hbar\Omega_m \hat{b}^\dagger \hat{b}, \tag{2.1}$$

wherein $\hat{a}$ ($\hat{a}^\dagger$) and $\hat{b}$ ($\hat{b}^\dagger$) are the respective lowering (raising) operators of the optical cavity and the mechanical resonator, with corresponding resonance frequencies ω_c and Ω_m.

The mirror's displacement $\hat{x}$ is given by

$$\hat{x} = \sqrt{\hbar/(2m_\mathrm{eff}\Omega_\mathrm{m})}\left(\hat{b} + \hat{b}^\dagger\right) = x_\mathrm{ZPF}\left(\hat{b} + \hat{b}^\dagger\right), \tag{2.2}$$

where we defined the zero-point fluctuation amplitude x_ZPF and the effective mass m_eff. Displacing the mirror alters the length of the optical cavity, thereby changing its resonance frequency. Hence, we can expand the cavity frequency in terms of the displacement as

$$\omega_\mathrm{c}(\hat{x}) = \omega_\mathrm{c}(0) + \hat{x}\frac{\partial\omega_\mathrm{c}}{\partial\hat{x}} + \dots . \tag{2.3}$$

Inserting Eq. (2.3), truncated at first order, into Eq. (2.1) and using Eq. (2.2) gives

$$\hat{H} = \hat{H}_0 + \hbar\hat{x}\frac{\partial\omega_\mathrm{c}}{\partial\hat{x}}\hat{a}^\dagger\hat{a} \quad = \hat{H}_0 + \hbar x_\mathrm{ZPF}(\hat{b} + \hat{b}^\dagger)\frac{\partial\omega_\mathrm{c}}{\partial\hat{x}}\hat{a}^\dagger\hat{a}. \tag{2.4}$$

Defining the single-photon coupling strength as $g_0 = -x_\mathrm{ZPF}\partial\omega_\mathrm{c}/\partial\hat{x}$, we end up with

$$\hat{H} = \hat{H}_0 - \hbar g_0(\hat{b} + \hat{b}^\dagger)\hat{a}^\dagger\hat{a}. \tag{2.5}$$

This additional term represents an interaction Hamiltonian $\hat{H}_\mathrm{int}$, between the light field in the cavity and the motion of the mirror. The single-photon coupling strength g_0 corresponds to the

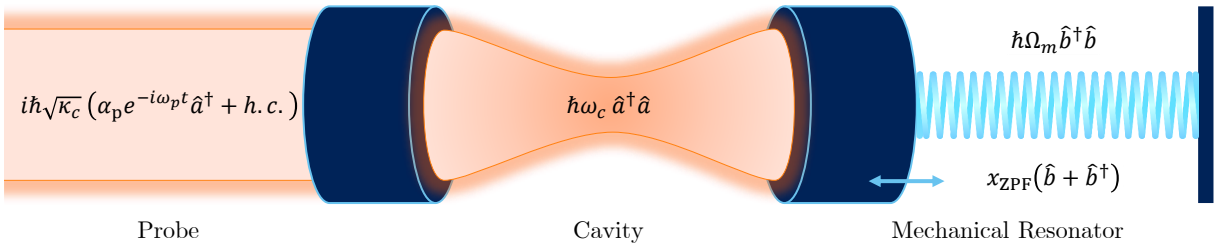

Fig. 2.1 Optomechanical Fabry–Pérot cavity with one mirror mounted to a spring. A displacement of the mirror changes the cavity resonance frequency, which results in an interaction between the light field in the cavity and the mechanical motion of the mirror. An external probe tone allows readout and control of the system.

frequency shift of the cavity due to a displacement of the mechanical resonator by its zero-point fluctuation amplitude. This enables the mechanical motion to be detected through the cavity's response.

Equivalently, g_0 determines the radiation pressure force exerted on the mirror by a single photon in the optical cavity. The total radiation pressure force is given by

$$\hat{F} = -\frac{d\hat{H}_{\mathrm{int}}}{d\hat{x}} = \hbar\frac{g_0}{x_{\mathrm{ZPF}}}\hat{a}^\dagger\hat{a}. \tag{2.6}$$

Due to this force, the motion of the mirror can be controlled via the light field in the cavity.

As illustrated in Fig. 2.1, a probe tone with amplitude α_{p} and frequency ω_{p} is used to interact with the cavity. This probe tone can be described by the Hamiltonian

$$\hat{H}_{\mathrm{p}} = i\hbar\sqrt{\kappa_{\mathrm{c}}}(\alpha_{\mathrm{p}}e^{-i\omega_{\mathrm{p}}t}\hat{a}^\dagger + \mathrm{h.c.}), \tag{2.7}$$

where κ_{c} is the external coupling rate. The external coupling introduces a loss channel, which, together with the internal loss rate κ_{i}, determines the total or loaded cavity linewidth

$$\kappa_{\mathrm{l}} = \kappa_{\mathrm{c}} + \kappa_{\mathrm{i}}. \tag{2.8}$$

In Sections 2.4 and 2.5, we will discuss this in more detail in the context of microwave cavities.

When driving the cavity, it is convenient to transform the Hamiltonian of the optomechanical system into the rotating frame of the probe. Applying the unitary transformation $\hat{U} = e^{-i\omega_{\mathrm{p}}\hat{a}^\dagger\hat{a}t}$ and omitting counter-rotating terms, gives

$$\hat{H} = -\hbar\Delta\hat{a}^\dagger\hat{a} + \hbar\Omega_{\mathrm{m}}\hat{b}^\dagger\hat{b} - \hbar g_0(\hat{b} + \hat{b}^\dagger)\hat{a}^\dagger\hat{a}, \tag{2.9}$$

where we omit the time-independent probe term $\hat{H}_{\mathrm{p}} = i\hbar\sqrt{\kappa_{\mathrm{c}}}(\alpha_{\mathrm{p}}\hat{a}^\dagger + \mathrm{h.c.})$, that only adds a global phase, and define

$$\Delta = \omega_{\mathrm{p}} - \omega_{\mathrm{c}} \tag{2.10}$$

as the detuning between the cavity and the probe frequency.

2.1.1 Linearised optomechanical interaction

As optomechanical systems often only achieve rather low g_0, strong pumps are used to enhance the optomechanical interaction [35, 38]. Increasing the number of circulating photons increases the radiation pressure force and leads to a bigger optomechanical interaction. In the following, we will derive how this strong pump effectively linearises the optomechanical Hamiltonian.

For a strong probe tone, the field in the cavity can be described by a classical average field amplitude $\bar{\alpha}$ and its small fluctuations $\delta\hat{a}$, which govern the quantum dynamics of the system. To derive an approximate optomechanical Hamiltonian, we replace

$$\hat{a} \to \bar{\alpha} + \delta\hat{a}. \tag{2.11}$$

Substituting this into the interaction Hamiltonian results in

$$\hat{H}_{\mathrm{int}} = -\hbar g_0(|\bar{\alpha}|^2 + \bar{\alpha}^*\delta\hat{a} + \delta\hat{a}^\dagger\bar{\alpha} + \delta\hat{a}^\dagger\delta\hat{a})(\hat{b} + \hat{b}^\dagger). \tag{2.12}$$

The first term $-\hbar g_0|\bar{\alpha}|^2(\hat{b}+\hat{b}^\dagger)$ corresponds to a static radiation pressure force $\bar{F} = \hbar g_0|\bar{\alpha}|^2/x_{\mathrm{ZPF}}$ acting on the mirror. This leads to a shift of the mirrors's resting position $\delta\bar{x} = \bar{F}/m_{\mathrm{eff}}\Omega_{\mathrm{m}}^2$ and the cavity frequency $\delta\omega_{\mathrm{c}} = g_0\delta\bar{x}/x_{\mathrm{ZPF}}$. Redefining the displacement and using the dressed cavity frequency in the definition of the detuning allows us to omit this term. We keep the second and third term, while the last term $-\hbar g_0\delta\hat{a}^\dagger\delta\hat{a}$ is small compared to the other terms and can be neglected. This allows us to approximate

$$\hat{H}_{\mathrm{int}} \approx -\hbar g_0(\bar{\alpha}^*\delta\hat{a} + \delta\hat{a}^\dagger\bar{\alpha})(\hat{b}+\hat{b}^\dagger). \tag{2.13}$$

If we now relate the mean light field amplitude $|\bar{\alpha}| = \sqrt{\bar{n}_{\mathrm{c}}}$ to the mean photon number $\bar{n}_{\mathrm{c}}$ in the cavity and assume $\bar{\alpha}$ to be real without loss of generality, we can write

$$\hat{H}_{\mathrm{int}} \approx -\hbar g_0\sqrt{\bar{n}_{\mathrm{c}}}(\delta\hat{a} + \delta\hat{a}^\dagger)(\hat{b}+\hat{b}^\dagger). \tag{2.14}$$

From this, we see that the single-photon coupling strength is enhanced by the number of photons in the cavity, and we can define the total optomechanical coupling strength

$$g = g_0\sqrt{\bar{n}_{\mathrm{c}}}. \tag{2.15}$$

Applying Eq. (2.11) to the full optomechanical Hamiltonian gives

$$\hat{H} \approx -\hbar\Delta\delta\hat{a}^\dagger\delta\hat{a} + \hbar\Omega_{\mathrm{m}}\hat{b}^\dagger\hat{b} - \hbar g(\delta\hat{a} + \delta\hat{a}^\dagger)(\hat{b}+\hat{b}^\dagger), \tag{2.16}$$

where we omit constant terms and choose $\bar{\alpha}$ such that $\bar{\alpha}^*\delta\hat{a} + \mathrm{h.c}$ cancels the probe [39].

The corresponding equations of motion for this Hamiltonian are linear, which leads to purely Gaussian classical evolution. This means it does not enable the preparation of nonclassical quantum states [40].

Even though we aim to reach the regime where the full nonlinear optomechanical interaction is relevant, interesting effects already arise in the linearised regime. For instance, the linear interaction enables the coherent exchange of states between the cavity and the mechanical resonator, allowing quantum states to be stored in the mechanical mode [41]. Introducing a nonlinearity would allow the preparation of nonclassical quantum states, which could be transferred to the mechanical mode. Furthermore, a parametric drive would allow the creation of squeezed mechanical states [42–44], which could enhance the sensitivity in mechanical position and force sensing applications. However, the implementation of such experiments is beyond the scope of this thesis.

2.1.2 Cooling of the mechanical mode

A major limitation in most applications of optomechanical systems is the presence of thermal noise, which affects the ability to observe quantum effects. At a given temperature T, the thermal occupation $\bar{n}_{\mathrm{m}}^{\mathrm{th}}$ of the mechanical mode is given by the Bose-Einstein distribution:

$$\bar{n}_{\mathrm{m}}^{\mathrm{th}} = \frac{1}{e^{\hbar\Omega_{\mathrm{m}}/k_{\mathrm{B}}T} - 1} \approx \frac{k_{\mathrm{B}}T}{\hbar\Omega_{\mathrm{m}}} \quad \text{for} \quad k_{\mathrm{B}}T \gg \hbar\Omega_{\mathrm{m}}. \tag{2.17}$$

Due to the inherently low resonance frequencies of macroscopic mechanical resonators, the thermal occupation of the mechanical mode remains high even at cryogenic temperatures. Therefore, additional cooling is required to reach the quantum ground state.

One method to reduce the thermal occupation of the mechanical mode is dynamical backaction cooling [26]. Thereby, the radiation pressure force exerted by the intracavity light field is used to dampen the mechanical mode. This process can be understood in a Raman-scattering picture. In Fig. 2.2 a), the energy level scheme of a sideband resolved optomechanical system i.e. $\kappa_\mathrm{l} < \Omega_\mathrm{m}$ is shown. Probing the system at different detunings and only considering resonant interaction terms of the Hamiltonian (2.16), we get:

- $\Delta = +\Omega_\mathrm{m} \rightarrow \hbar g(\delta\hat{a}\hat{b} + \delta\hat{a}^\dagger\hat{b}^\dagger)$: For a blue-detuned probe, only terms that create or destroy one photon and one phonon are resonant. This interaction can heat the mechanical mode.
- $\Delta = -\Omega_\mathrm{m} \rightarrow \hbar g(\delta\hat{a}\hat{b}^\dagger + \delta\hat{a}^\dagger\hat{b})$: For a red-detuned probe, only terms that create one photon and simultaneously destroy one phonon are resonant. As shown in Fig. 2.2 a), this can cool the mechanical mode.
- $\Delta = 0 \rightarrow \hbar g(\delta\hat{a} + \delta\hat{a}^\dagger)(\hat{b} + \hat{b}^\dagger)$: On resonance, the phase of the light field in the cavity is modulated by the position of the mechanical resonator $\propto (\hat{b} + \hat{b}^\dagger)$. This allows us to detect the mechanical motion via the cavity without changing the mechanical occupation.

In the sideband unresolved regime, shown in Fig. 2.2 b), where the total linewidth of the optical cavity is bigger than the mechanical frequency, i.e. $\kappa_\mathrm{l} > \Omega_\mathrm{m}$, one cannot individually select between the three described processes. Nevertheless, for a red detuned probe tone, the heating Stokes process (with rate Γ_+) remains less resonant than the cooling anti-Stokes process (with rate Γ_-), and cooling of the mechanical mode is still possible.

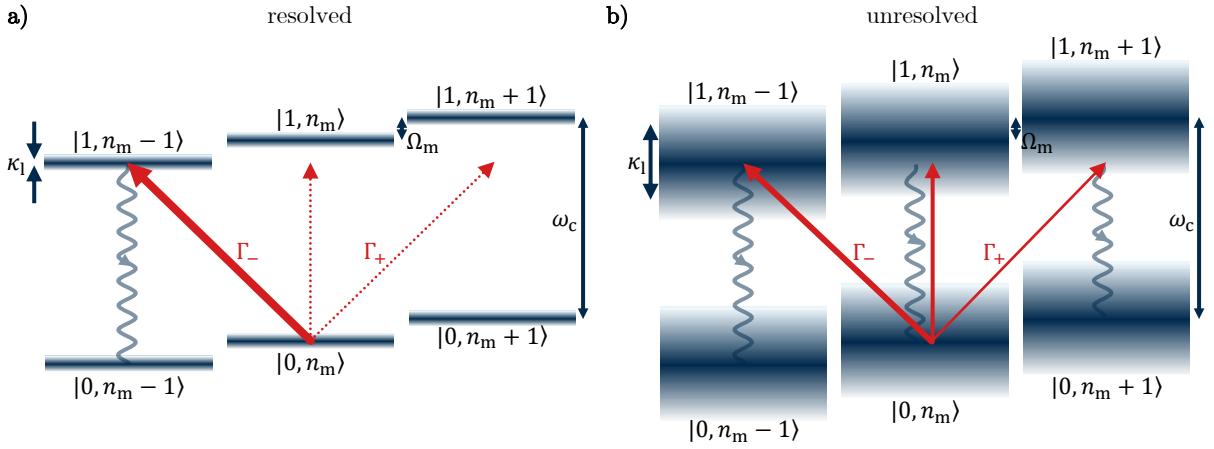

Fig. 2.2 Energy level diagram for an optomechanical system. **a)** In the resolved sideband regime, where $\kappa_\mathrm{l} < \Omega_\mathrm{m}$, transitions can be individually addressed. A red-detuned pump tone with $\Delta = -\Omega_\mathrm{m}$, that drives the transition $|0, n_\mathrm{m}\rangle \leftrightarrow |1, n_\mathrm{m}-1\rangle$, leads to cooling of the mechanical mode. The red-detuned photon annihilates one phonon to create a photon at the cavity frequency. If κ_l is significantly larger than the mechanical decay rate $\kappa_\mathrm{l} \gg \Gamma_\mathrm{m}$ and the cavity is not thermally excited, the cavity quickly decays back into the ground state. **b)** In the unresolved sideband regime, where $\kappa_\mathrm{l} > \Omega_\mathrm{m}$, addressing individual transitions is not possible. However, due to slightly different rates of the Stokes Γ_+ and anti-Stokes Γ_- processes, cooling of the mechanical mode remains possible.

To calculate the Stokes and anti-Stokes rate for the case of weak coupling $g \ll \kappa_\mathrm{l}$, we can apply Fermi's golden rule to the interaction Hamiltonian $H_\mathrm{int} = -\hat{x}\hat{F}$ of the mechanical resonator with the fluctuating radiation pressure force [39]. This yields the rates

$$\Gamma_\pm = \frac{x_\mathrm{ZPF}^2}{\hbar^2} S_{FF}(\omega = \mp\Omega_\mathrm{m}) = g_0^2 S_{nn}(\omega = \mp\Omega_\mathrm{m}), \tag{2.18}$$

wherein $S_{FF}(\omega) = \int_{-\infty}^{+\infty} dt e^{i\omega t}\langle \hat{F}(t)\hat{F}(0)\rangle$ is the radiation pressure force noise spectrum, which is related to the intracavity photon number noise spectrum $S_{nn}(\omega) = \int_{-\infty}^{+\infty} dt e^{i\omega t}\langle(\hat{a}^\dagger\hat{a})(t)(\hat{a}^\dagger\hat{a})(0)\rangle$ because of the optomechanical interaction. For a cavity probed with a mean input photon number rate $\bar{n}_\mathrm{in} = P_\mathrm{in}/\hbar\omega_\mathrm{p}$, corresponding to a probe tone power P_in, the photon number noise spectrum can be calculated as

$$S_{nn}(\omega) = \bar{n}_\mathrm{c} \frac{\kappa_\mathrm{l}}{(\Delta+\omega)^2 + \kappa_\mathrm{l}^2/4}, \tag{2.19}$$

where $\bar{n}_\mathrm{c}$ is the average intracavity photon number, given by

$$\bar{n}_\mathrm{c} = \frac{\kappa_\mathrm{c}/2}{\Delta^2 + \kappa_\mathrm{l}^2/4} 2\pi \bar{n}_\mathrm{in}. \tag{2.20}$$

Anticipating our experimental configuration, explained later in Section 2.4, we assume a cavity coupled in a notch configuration [45], which gives a factor of 1/2 in κ_c. The factor of 2π converts the input photon number rate, defined as a natural frequency, to an angular frequency. With that, the optomechanically induced damping rate

$$\Gamma_\mathrm{OM} = \Gamma_- - \Gamma_+ \quad \Rightarrow \quad \Gamma_\mathrm{m,eff} = \Gamma_m + \Gamma_\mathrm{OM}, \tag{2.21}$$

that leads to a broadening (in case of cooling) or narrowing (in case of heating) of the intrinsic mechanical linewidth Γ_m, can be written as

$$\Gamma_\mathrm{OM} = g_0^2 \bar{n}_\mathrm{c} \left(\frac{\kappa_\mathrm{l}}{(\Delta+\Omega_\mathrm{m})^2 + \kappa_\mathrm{l}^2/4} - \frac{\kappa_\mathrm{l}}{(\Delta-\Omega_\mathrm{m})^2 + \kappa_\mathrm{l}^2/4} \right). \tag{2.22}$$

For the case of strong heating, this can lead to an effectively negative mechanical linewidth $\Gamma_\mathrm{m,eff} < 0$. In this regime, the system becomes unstable, and the mechanical occupation grows exponentially over time until it is limited by nonlinear effects.

Moreover, it can be shown that the optomechanical interaction leads to a shift in the mechanical resonance frequency

$$\delta\Omega_\mathrm{m} = g_0^2 \bar{n}_\mathrm{c} \left(\frac{\Delta+\Omega_\mathrm{m}}{(\Delta+\Omega_\mathrm{m})^2 + \kappa_\mathrm{l}^2/4} + \frac{\Delta-\Omega_\mathrm{m}}{(\Delta-\Omega_\mathrm{m})^2 + \kappa_\mathrm{l}^2/4} \right), \tag{2.23}$$

an effect known as the optical spring effect [46]. Depending on the selected detuning, the spring suspending the mirror effectively hardens or softens, increasing or decreasing Ω_m.

Using the Stokes and anti-Stokes rates, one can calculate the steady-state mechanical occupation

$$\bar{n}_\mathrm{m} = \frac{\Gamma_+ + \bar{n}_\mathrm{m}^\mathrm{th}\Gamma_\mathrm{m}}{\Gamma_- - \Gamma_+ + \Gamma_\mathrm{m}}. \tag{2.24}$$

In case of strong cooling $\Gamma_{\mathrm{OM}} \gg \Gamma_{\mathrm{m}}$, one can assume $\Gamma_{\mathrm{m}} = 0$, which is the case for an ideal mechanical system completely decoupled from its environment. This leads to a minimal occupation

$$\bar{n}_{\mathrm{m}}^{\mathrm{min}} = \frac{\Gamma_+}{\Gamma_- - \Gamma_+} = \left(\frac{(\Delta - \Omega_{\mathrm{m}})^2 + \kappa_{\mathrm{l}}^2/4}{(\Delta + \Omega_{\mathrm{m}})^2 + \kappa_{\mathrm{l}}^2/4} - 1 \right)^{-1}, \tag{2.25}$$

often referred to as the backaction limit [26, 33, 47].

Varying the detuning to minimise this expression in the limit of the resolved sideband regime $\kappa_{\mathrm{l}} \ll \Omega_{\mathrm{m}}$, yields the minimal mechanical occupation at $\Delta = -\Omega_{\mathrm{m}}$

$$\bar{n}_{\mathrm{m}}^{\mathrm{min}} = \left(\frac{\kappa_{\mathrm{l}}}{4\Omega_{\mathrm{m}}} \right)^2 < 1. \tag{2.26}$$

This shows that ground-state cooling is possible. In the far unresolved sideband regime $\kappa_{\mathrm{l}} \gg \Omega_{\mathrm{m}}$,

$$\bar{n}_{\mathrm{m}}^{\mathrm{min}} = \frac{\kappa_{\mathrm{l}}}{4\Omega_{\mathrm{m}}} > 1, \tag{2.27}$$

even at an optimal detuning of $\Delta = -\kappa_{\mathrm{l}}/2$, backaction cooling does not allow cooling to the ground state. Note that it has been demonstrated that this backaction limit can be overcome by e.g. squeezing the intracavity light field [48]. However, as we will explain in the following, cooling in our system is not only limited by backaction.

In Fig. 2.3 a), cooling of the mechanical mode is simulated for typical parameters of our system in the unresolved sideband regime. For a red detuned probe $\Delta < 0$, the optomechanically induced damping Γ_{OM} lowers the mechanical occupation $\bar{n}_{\mathrm{m}}$, while the optical spring effect shifts the mechanical frequency by $\delta\Omega_{\mathrm{m}}$. Increasing the intracavity photon number enhances the optomechanical interaction and improves cooling till the backaction limit $\bar{n}_{\mathrm{m}}^{\mathrm{min}}$ (dashed line).

However, in our system, the photon number cannot be arbitrarily increased, as it is constrained by an intrinsic Kerr nonlinearity of the cavity, which we will discuss in more detail in Section 2.3.4. Consequently, we can only reach the backaction limit for a sufficiently large single-photon coupling strength g_0. In Section 2.1.3, we will show how the Kerr nonlinearity can increase the cooling efficiency in the unresolved sideband regime by partially suppressing the Stokes process [8]. This allows reaching lower phonon numbers with fewer intracavity photons than with an identical linear cavity [7]. Despite this improvement, the backaction limit remains unchanged in the nonlinear case and reaching the ground state would still require additional techniques to overcome the backaction limit [8].

A more straightforward path to ground-state cooling could be to push the system towards the resolved sideband regime by reducing the cavity linewidth κ_{l}. This is shown in Fig. 2.3 b). Decreasing the cavity linewidth κ_{l} suppresses the Stokes process Γ_+, thereby increasing the cooling efficiency and lowering the backaction limit (dashed lines). Even reducing the linewidth by a factor of 2, such that the sideband resolved parameter $\Omega_{\mathrm{m}}/\kappa_{\mathrm{l}}$ changes from 0.1 to 0.2, pushes the backaction limit below one phonon. Reducing the cavity linewidth by one order of magnitude, such that $\Omega_{\mathrm{m}}/\kappa_{\mathrm{l}} = 1$, would allow cooling the mechanical mode to less than 10 phonons with only 10 intracavity photons. With $\Omega_{\mathrm{m}}/\kappa_{\mathrm{l}} = 10$, cooling below one phonon would be possible with only 10 intracavity photons.

As will be explained in Section 2.7, the single-photon coupling strength g_0 in our system is not fixed but can be tuned in situ. The maximum coupling strength at which the system can still be reliably operated is primarily limited by its shielding from external noise sources [7]. Recent improvements in shielding the system from vibrational noise [9] should allow for operating at even higher g_0 than the 1 kHz assumed here. This would ease the constraints on the cavity linewidth necessary to achieve ground-state cooling.

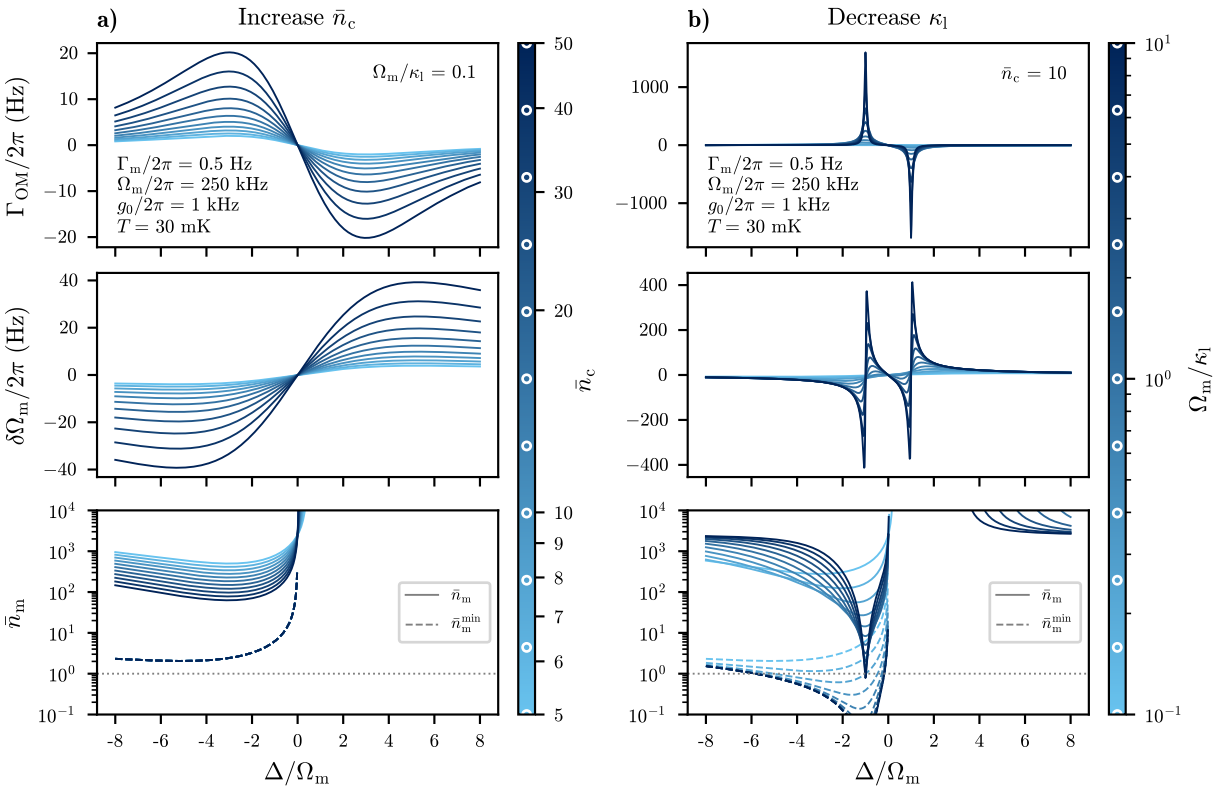

Fig. 2.3 **a)** Cooling of the mechanical mode for typical system parameters in the unresolved sideband regime. Different colours correspond to different intracavity photon numbers, marked on the colorbar for the individual traces. The dashed line shows the backaction limit $\bar{n}_m^{min}$. **b)** Cooling for the same system as in a), but with different colours corresponding to decreasing cavity linewidth κ_l. Moving towards a resolved system, suppression of the Stokes process increases the cooling efficiency and lowers the backaction limit $\bar{n}_m^{min}$ (dashed lines). In the resolved regime, the detuning for optimal cooling moves towards $\Delta = -\Omega_m$. With $\Omega_m/\kappa_l = 10$ cooling below one phonon would be possible at only 10 intracavity photons.

Note that in our experiment, cooling traces are typically obtained using a constant probe tone power $P_{in} = \hbar\omega_p\bar{n}_{in}$. Consequently, the intracavity photon number varies with detuning, as described by Eq. (2.20). Fig. 2.4 illustrates cooling for the same system parameters as in Fig. 2.3. However, instead of maintaining a constant intracavity photon number across all detunings of a single trace, the photon number is calculated at each detuning based on the constant input power P_{in}. This variation in intracavity photon number affects the total optomechanical coupling and modifies the shape of the cooling traces.

For a fair comparison of cooling performance in Fig. 2.4 b), we select the input power for individual traces such that the intracavity photon number remains constant at the detuning with optimal cooling. In the resolved sideband regime, this approach results in relatively high intracavity photon numbers near $\Delta = 0$, as higher input powers are necessary to achieve $n_c(\Delta_{\text{bestcooling}}) = 10$. This could break the assumption of weak coupling $g_0\sqrt{\bar{n}_c} \ll \kappa_l$. However, while this may alter the trace close to $\Delta = 0$, it does not affect the validity of the results at the detuning where optimal cooling occurs.

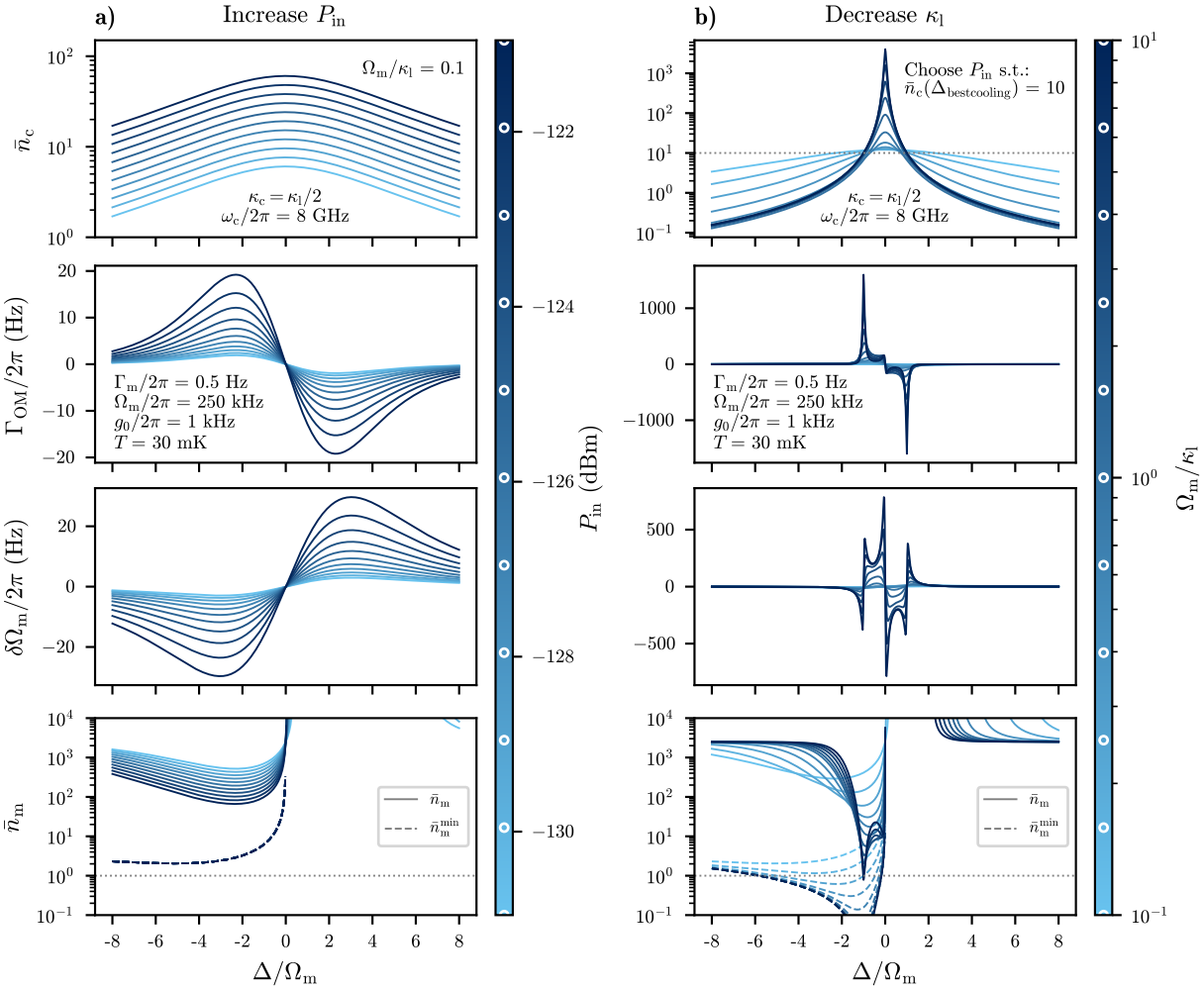

Fig. 2.4 Optomechanical cooling for the same system parameters as in Fig. 2.3. Instead of keeping the intracavity photon number constant, the probe tone power P_{in} is held constant for individual traces, causing the intracavity photon number to vary with detuning. This variation affects the effective optomechanical coupling and modifies the cooling traces. In **a** different traces correspond to different probe tone powers as marked on the colour bar. In **b)** the input powers for the individual traces are chosen such that the intracavity photon number for all traces is constant at the detuning with optimal cooling. This ensures a constant photon-enhanced coupling strength for the points of optimal cooling and enables a fair comparison of cooling performance with respect to the cavity linewidth.

2.1.3 Kerr enhanced cooling

When designing an optomechanical system, one would typically aim for a linear cavity, as nonlinearities impose limitations on the maximum drive amplitude and consequently the photon-enhanced coupling strength (Eq. (2.14)). Nevertheless, in the unresolved sideband regime, a nonlinear cavity can facilitate enhanced cooling as theoretically derived in [8, 49] and experimentally demonstrated in [7, 9, 50].

Similar to an optomechanical system with a linear cavity, the rates of the Stokes and anti-Stokes processes are given by

$$\Gamma_{\pm} = g_0^2 S_{nn}(\omega = \mp\Omega_{\mathrm{m}}), \tag{2.28}$$

wherein for the nonlinear cavity, with Kerr constant $\mathcal{K}$, the photon noise spectrum [8] reads

$$S_{nn}(\omega) = \bar{n}_{\mathrm{c}}\kappa_{\mathrm{l}} \frac{(-\tilde{\Delta} + \omega + \mathcal{K}\bar{n}_{\mathrm{c}})^2 + \kappa_{\mathrm{l}}^2/4}{(\tilde{\Delta}^2 - \omega^2 + \kappa_{\mathrm{l}}^2/4 - \mathcal{K}^2\bar{n}_{\mathrm{c}}^2)) + \kappa_{\mathrm{l}}^2\omega}, \quad \text{with} \quad \tilde{\Delta} = \Delta + 2\mathcal{K}\bar{n}_{\mathrm{c}}. \tag{2.29}$$

The mean intracavity photon number $\bar{n}_{\mathrm{c}}$ satisfies

$$\bar{n}_{\mathrm{c}} \left((\Delta + \mathcal{K}\bar{n}_{\mathrm{c}})^2 + \frac{\kappa_l^2}{4} \right) = \frac{\kappa_c}{2} 2\pi \bar{n}_{\mathrm{in}}. \tag{2.30}$$

Above the critical input photon number rate $\bar{n}_{\mathrm{in,bi}}$, the cavity becomes bistable and multiple solutions for the intracavity photon number exist

$$\bar{n}_{\mathrm{in}} > \bar{n}_{\mathrm{in,bi}} = \frac{1}{2\pi} \frac{2\kappa_{\mathrm{l}}}{\kappa_{\mathrm{c}}} \frac{\kappa_{\mathrm{l}}^2}{3\sqrt{3}\mathcal{K}}. \tag{2.31}$$

Again, note that in contrast to Ref. [8], here we assume a cavity with finite internal loss, that is coupled in a notch configuration. This results in an additional factor of $2\kappa_{\mathrm{l}}/\kappa_{\mathrm{c}}$. Furthermore, we defined the input photon number rate as a natural frequency, which gives a factor of $1/2\pi$

The mechanical frequency shit due to the optical spring effect in the nonlinear case is given by

$$\delta\Omega_{\mathrm{m}} = -2g_0^2\bar{n}_{\mathrm{c}} \frac{(\mathcal{K}\bar{n}_{\mathrm{c}} - \tilde{\Delta}) \left(\tilde{\Delta}^2 - \Omega_{\mathrm{m}}^2 + \kappa_{\mathrm{l}}^2/4 - \bar{n}_{\mathrm{c}}^2\mathcal{K}^2 \right)}{\left(\tilde{\Delta}^2 - \Omega_{\mathrm{m}}^2 + \kappa_{\mathrm{l}}^2/4 - \bar{n}_{\mathrm{c}}^2\mathcal{K}^2 \right)^2 + \kappa_{\mathrm{l}}^2\Omega_{\mathrm{m}}^2}. \tag{2.32}$$

As shown in the insets of Fig. 2.5, the Kerr nonlinearity leads to an asymmetric intracavity photon number spectrum, which enhances the cooling efficiency. The power-dependent frequency shift of the cavity moves the detuning for optimal cooling to more negative values. Similar to a system deeper in the sideband resolved regime, the cooling feature becomes narrower and deeper.

Further increasing the input power would lead to bifurcation of the intracavity photon number. Notably, it has been demonstrated that optomechanical cooling is still possible in this regime [9]. However, unlike in a more sideband resolved system, the backaction limit (shown by the dashed lines) is not improved by the nonlinearity of the cavity. Therefore, reaching the ground state would require additional techniques like squeezing the intracavity field to overcome the backaction limit [49].

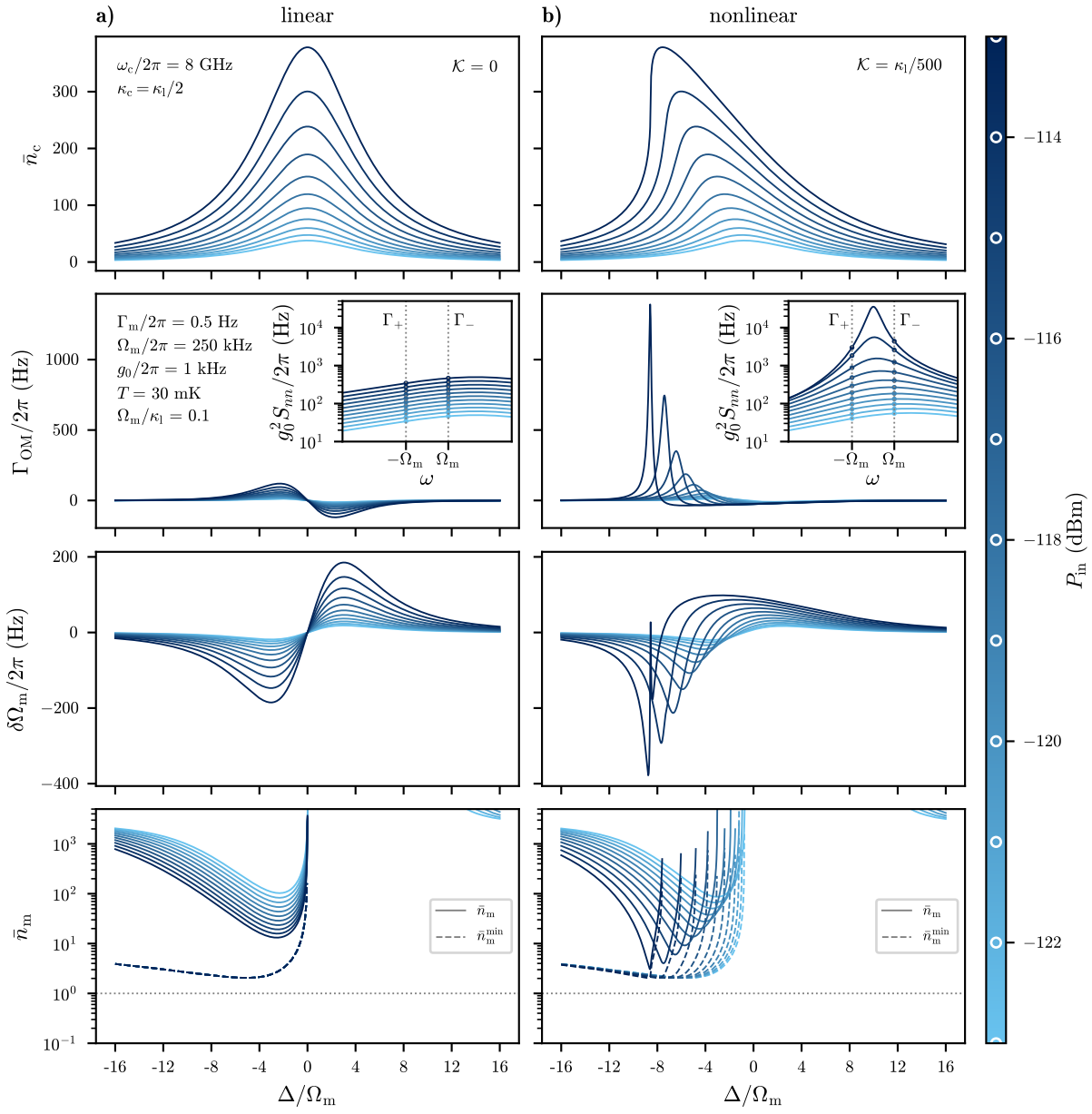

Fig. 2.5 Comparison of cooling in the unresolved sideband regime for two identical optomechanical systems with **a)** linear $\mathcal{K} = 0$ and **b)** nonlinear $\mathcal{K} = \kappa_l/500$ cavity. Different colors correspond to different input powers. Powers used for the plotted traces are marked on the colorbar. Insets show the photon noise spectra for the detunings with optimal cooling. The resulting values of the Stokes and anti-Stokes rates $\Gamma_\pm$ are marked at $\omega = \mp\Omega_m$. The asymmetric photon number spectrum of the nonlinear cavity improves the cooling efficiency. For the same input power, lower phonon numbers can be reached with the nonlinear cavity. The dashed lines show the backaction limit n_m^{min}.

2.2 Microstrip cavities

In our optomechanical system, a superconducting microwave cavity replaces the optical cavity presented in the previous section. In particular, we use a $\lambda/2$ microstrip cavity, placed in a rectangular waveguide [51, 52].

Fig. 2.6 a) shows a schematic representation of such a cavity. The U-shaped microstrip, made from a thin film of niobium (Nb), is patterned onto a silicon (Si) substrate. In Fig. 2.6 b) the magnitude of the electric field E and surface current I for the fundamental $\lambda/2$ mode can be seen. The simulation data was taken from Ref. [51] and shows that the fundamental mode has an electric field node and a current antinode at the centre of the microstrip.

Fig. 2.6 c) shows the distributed element model of the microstrip cavity. Each infinitesimal microstrip segment is modelled as an inductance l and capacitance c, with an additional shunt capacitance c_n^{s} between the U-shaped legs. The circuit's ground is provided by the walls of the waveguide. Based on this model, we will now determine the Lagrangian for the microstrip cavity and demonstrate how the symmetry of its fundamental mode enables an approximation as an LC circuit. The Lagrangian can be written in terms of the node fluxes ϕ_n^{L} and ϕ_n^{R} [53, 54]

$$\mathcal{L} = \left(\frac{\Phi_0}{2\pi}\right)^2 \sum_{n=1}^{N} \left(\frac{c(\dot{\phi}_n^{\mathrm{L}})^2}{2} - \frac{(\phi_{n+1}^{\mathrm{L}} - \phi_n^{\mathrm{L}})^2}{2l} + \frac{c(\dot{\phi}_n^{\mathrm{R}})^2}{2} - \frac{(\phi_{n+1}^{\mathrm{R}} - \phi_n^{\mathrm{R}})^2}{2l} + \frac{c_n^{\mathrm{s}}(\dot{\phi}_n^{\mathrm{R}} - \dot{\phi}_n^{\mathrm{L}})^2}{2} \right). \tag{2.33}$$

The circuit supports two types of modes: symmetric and antisymmetric. For symmetric modes, which have an electric field antinode at the centre of the microstrip and $\phi_n^{\mathrm{L}} = \phi_n^{\mathrm{R}}$, the effect of the shunt capacitance vanishes. For antisymmetric modes, such as the fundamental mode, we have $\phi_n^{\mathrm{L}} = -\phi_n^{\mathrm{R}} =: \phi_n$. Hence, the Lagrangian can be simplified to

$$\mathcal{L} = \left(\frac{\Phi_0}{2\pi}\right)^2 \sum_{n=1}^{N} \left(\frac{(2c + 4c_n^{\mathrm{s}})\dot{\phi}_n^2}{2} - \frac{2(\phi_{n+1} - \phi_n)^2}{2l} \right). \tag{2.34}$$

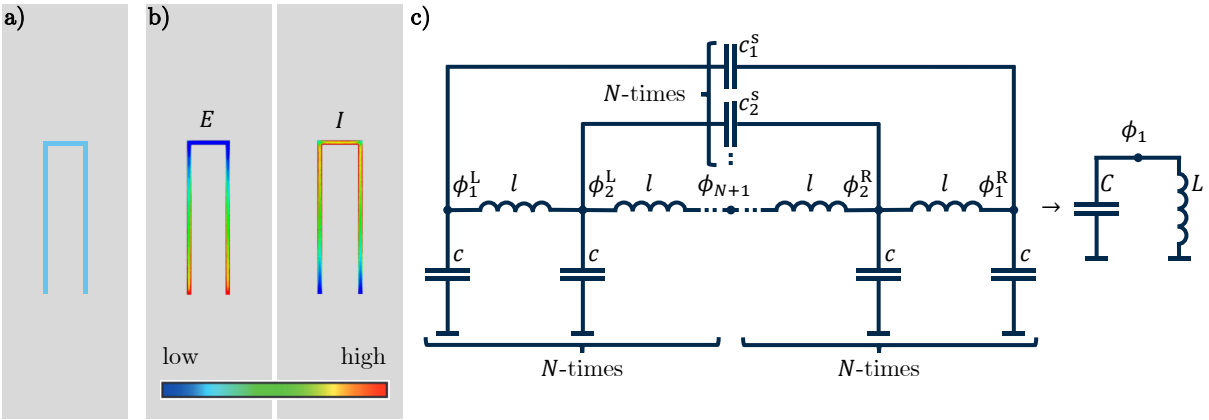

Fig. 2.6 **a)** Schematic representation of a silicon chip with a U-shaped microstrip, made from a thin film of niobium. **b)** Simulated magnitude of the electric field E and surface current I for the $\lambda/2$ fundamental mode. Data taken from Ref. [51]. **c)** Distributed and lumped element circuit diagrams of the microstrip cavity.

For $N \to \infty$, changing the sum into an integral over the total length d_m of the microstrip and redefining the capacitance c, inductance l and shunt capacitance $c_\mathrm{s}(x)$ as values per unit length we get

$$\mathcal{L} = \left(\frac{\Phi_0}{2\pi}\right)^2 \int_{-d_\mathrm{m}/2}^{d_\mathrm{m}/2} \left(\frac{(2c + 4c_\mathrm{s}(x))\dot{\phi}^2(x)}{2} - \frac{2\left(d\phi(x)/dx\right)^2}{2l} \right) dx. \tag{2.35}$$

Only considering the fundamental mode $\phi(x) = \phi_1 \cos(\pi x/d_\mathrm{m})$ [54], this can be written as

$$\mathcal{L} = \left(\frac{\Phi_0}{2\pi}\right)^2 \int_{-d_\mathrm{m}/2}^{d_\mathrm{m}/2} \left(\frac{(2c + 4c_\mathrm{s}(x))\dot{\phi_1}^2 \cos^2(\pi x/d_\mathrm{m})}{2} - \frac{2(\phi_1 \pi/d_\mathrm{m})^2 \sin^2(\pi x/d_\mathrm{m})}{2l} \right) dx. \tag{2.36}$$

The primary contribution of the shunt capacitance $\bar{c}_\mathrm{s}(x)$, arises at the ends of the cavity legs, where the electric field difference is maximal. In this region, sufficiently distant from where the two parallel legs are connected, one can assume that the shunt capacitance per unit length is to a good approximation constant in x, which allows one to to pull $\bar{c}_\mathrm{s}$ in front of the integral, which yields

$$\mathcal{L} = \left(\frac{\Phi_0}{2\pi}\right)^2 \left(\frac{(2c + 4c_\mathrm{s})\dot{\phi_1}^2 d_\mathrm{m}/2}{2} - \frac{2(\phi_1 \pi/d_\mathrm{m})^2 d_\mathrm{m}/2}{2l} \right). \tag{2.37}$$

Defining the effective capacitance $C = d_\mathrm{m}(c + 2c_\mathrm{s})$ and $L = d_\mathrm{m} l/\pi^2$, this can be written as

$$\mathcal{L} = \left(\frac{\Phi_0}{2\pi}\right)^2 \left(\frac{C\dot{\phi_1}^2}{2} - \frac{\phi_1^2}{2L} \right), \tag{2.38}$$

which corresponds to the Lagrangian of an LC circuit, as shown in Fig. 2.6 c). The corresponding Hamiltonian is given by

$$\hat{H} = \hbar\omega_\mathrm{c} \hat{a}^\dagger \hat{a}, \quad \text{where} \quad \omega_\mathrm{c} = 1/\sqrt{LC}. \tag{2.39}$$

2.3 Frequency tunable microstrip cavities

To allow tuning of the resonance frequency and mediate a magnetic coupling to a mechanical resonator, we introduce a variable inductance, in the form of a superconducting quantum interference device (SQUID), in the microstrip cavity. As depicted in Fig. 2.7 a), a SQUID consists of a superconducting loop interrupted by two thin insulating barriers. The barriers interrupting the superconductor form so-called Josephson junctions [55, 56].

2.3.1 Josephson junction

The thin barrier of a Josephson junction allows Cooper pairs to tunnel through, leading to a current I_j and a voltage V_j across the junction. The Josephson equations [56]

$$I_\mathrm{j} = I_\mathrm{c} \sin(\phi_\mathrm{j}), \quad V_\mathrm{j} = \frac{\Phi_0}{2\pi} \frac{\partial \phi_\mathrm{j}}{\partial t}, \tag{2.40}$$

relate this voltage and current to the phase difference ϕ_j of the superconducting wavefunction across the leads forming the junction. The critical current I_c of the junction depends on the materials used, the thickness and area of the barrier. Using the Josephson equations, one can obtain

$$V_j = \frac{\Phi_0}{2\pi I_\mathrm{c}} \frac{1}{\cos(\phi_\mathrm{j})} \frac{\partial I_\mathrm{j}}{\partial t} = \frac{L_{\mathrm{j},0}}{\cos(\phi_\mathrm{j})} \frac{\partial I_\mathrm{j}}{\partial t}, \tag{2.41}$$

which shows that a Josephson junction behaves as a nonlinear inductance $L_j = L_{\mathrm{j},0}/\left|\cos(\phi_\mathrm{j})\right|$, wherein we define the linear junction inductance as $L_{\mathrm{j},0} = \Phi_0/(2\pi I_\mathrm{c})$.

2.3.1.1 Magnetic field tunability of a Josephson junction

Applying an in-plane magnetic field, normal to the tunnelling direction of Cooper pairs in the Josephson junction, leads to a reduction of the critical current I_c and therefore to an increase in inductance L_j of the junction [56].

The critical current of the Josephson junction tunes with

$$I_c(\Phi_{j,ip}) = I_c(\Phi_{j,ip} = 0) \cdot \mathrm{sinc}\left(\pi \frac{\Phi_{j,ip}}{\Phi_0}\right), \tag{2.42}$$

where $\Phi_{j,ip}$ is the in-plane magnetic flux threading the area of the insulating junction barrier. With that, the junction inductance behaves as

$$L_j(\Phi_{j,ip}) = \frac{L_j(\Phi_{j,ip} = 0)}{\left|\mathrm{sinc}\left(\pi \frac{\Phi_{j,ip}}{\Phi_0}\right)\right|}. \tag{2.43}$$

To create one flux quantum Φ_0 in the small area of the junction barrier, a rather high magnetic field is required. Hence, the sensitivity to changes in the magnetic field of a single Josephson junction is quite small. To increase the effective area and the tunability in inductance, two Josephson junctions can be combined in a superconducting loop, forming a direct current superconducting quantum interference device (DC-SQUID).

2.3.2 Direct Current - Superconducting quantum interference device

As shown in Fig. 2.7 a) a DC-SQUID consists of a superconducting loop, that is interrupted by two parallel Josephson junctions [56, 57]. For simplicity, we assume a symmetric SQUID, where both junctions have the same critical current I_c. A more general treatment of an asymmetric SQUID can be found in Ref. [5], which serves as the basis for the following discussion, presented here in a summarised form.

Using Eq. (2.40), the current across a symmetric SQUID, can be written as

$$I_{SQUID} = I_c \sin(\phi_1) + I_c \sin(\phi_2) = 2I_c \cos\left(\frac{\phi_1 - \phi_2}{2}\right) \sin\left(\frac{\phi_1 + \phi_2}{2}\right). \tag{2.44}$$

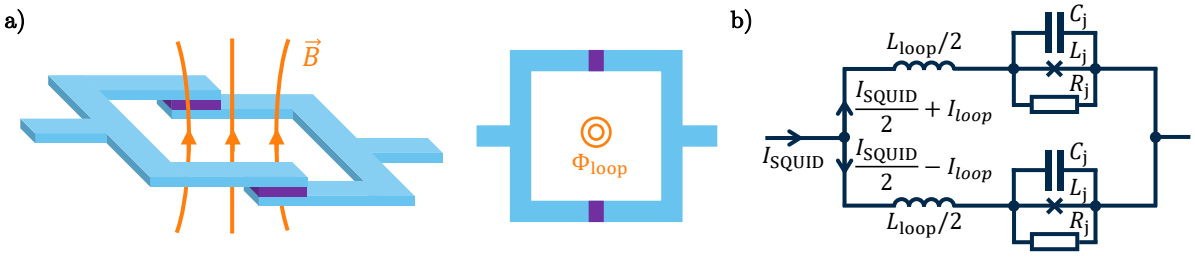

Fig. 2.7 **a)** Schematic representation of a SQUID. A loop of superconducting material is interrupted by two Josephson junctions. An external applied magnetic flux, changes the inductance periodically with the magnetic flux quantum Φ_0. **b)** Equivalent circuit diagram of a SQUID, including junction capacitance C_j, normal resistance R_j (RCSJ-model [57]) and loop inductance L_{loop}. Unless stated otherwise, we neglect the junction capacitance. The normal resistance only becomes relevant when exceeding the junction critical current.

Since the SQUID loop has to fulfil the fluxoid quantisation condition

$$\phi_1 - \phi_2 - \frac{2\pi}{\Phi_0}\Phi_{\text{loop}} = 2\pi n \quad | \quad n \in \mathbb{Z}, \tag{2.45}$$

we can relate the phase differences ϕ_1 and ϕ_2 over the junctions to the magnetic flux threading the SQUID loop Φ_{loop}. After assuming $n = 0$ without loss of generality, we can write

$$I_{\text{SQUID}} = 2I_{\text{c}} \cos(\pi\Phi_{\text{loop}}/\Phi_0) \sin(\phi_{\text{SQUID}}), \tag{2.46}$$

where we define the phase drop over the SQUID as $\phi_{\text{SQUID}} = (\phi_1 + \phi_2)/2 = \phi_1 + \pi\Phi_{\text{loop}}/\Phi_0$. Comparing this to the current over a single junction, given by Eq. (2.40), we see that a SQUID exhibits similar behaviour. The key difference is that the effective critical current

$$I_{\text{c,SQUID}}(\Phi_{\text{loop}}) = 2I_{\text{c}} \cos(\pi\Phi_{\text{loop}}/\Phi_0) \tag{2.47}$$

and hence the inductance,

$$L_{\text{SQUID}}(\Phi_{\text{loop}}) = \frac{L_{\text{SQUID}}(\Phi_{\text{loop}} = 0)}{|\cos(\pi\Phi_{\text{loop}}/\Phi_0)|}, \tag{2.48}$$

can be periodically tuned by changing the magnetic flux through the loop. This makes a SQUID extremely sensitive to changes in magnetic flux as small as a fraction of a single flux quantum [57].

Like a single junction, a SQUID behaves as a nonlinear inductance in the presence of a bias current I_{SQUID}. This current induces a phase drop ϕ_{SQUID}, which modifies the total effective inductance

$$L_{\text{SQUID}}(\Phi_{\text{loop}}, \phi_{\text{SQUID}}) = \frac{L_{\text{SQUID}}(\Phi_{\text{loop}} = 0, \phi_{\text{SQUID}} = 0)}{|\cos(\pi\Phi_{\text{loop}}/\Phi_0)\cos(\phi_{\text{SQUID}})|}. \tag{2.49}$$

For zero bias current and zero loop flux, the linear SQUID inductance is given by

$$L_{\text{SQUID,0}} = L_{\text{SQUID}}(\Phi_{\text{loop}} = 0, \phi_{\text{SQUID}} = 0) = \frac{L_{\text{j,0}}}{2} = \frac{\Phi_0}{2\pi}\frac{1}{2I_{\text{c}}}. \tag{2.50}$$

2.3.2.1 Loop inductance - Screening parameter

Figure 2.7 b), shows the equivalent circuit of a SQUID. In reality, a junction can be modelled as an ideal junction that is shunted with a resistance R_{j} corresponding to the normal resistance of the oxide barrier, and a capacitance C_{j} (RCSJ-model [57]). The normal resistance is only relevant when exceeding the junction critical current, and in the following derivation, we will neglect C_{j}.

Furthermore, the material forming the loop has an inductance L_{loop} which induces a screening or loop current I_{loop} and causes a difference between the external applied flux Φ_{ext} and the actual flux threading the loop

$$\Phi_{\text{loop}} = \Phi_{\text{ext}} + L_{\text{loop}} I_{\text{loop}}. \tag{2.51}$$

The loop current I_{loop} circulating the SQUID is implicitly given by

$$\begin{aligned} I_{\text{SQUID}}/2 + I_{\text{loop}} &= I_c \sin(\phi_1) \\ I_{\text{SQUID}}/2 - I_{\text{loop}} &= I_c \sin(\phi_2). \end{aligned} \tag{2.52}$$

For small bias currents $I_{\mathrm{SQUID}} \ll I_{\mathrm{loop}}$, we get $I_{\mathrm{loop}} \approx I_c \sin(\phi_1) \approx -I_c \sin(\phi_2)$, which together with the fluxoid quantization condition Eq. (2.45) gives

$$I_{\mathrm{loop}} \approx \pm I_{\mathrm{c}} \sin\left(\pi \frac{\Phi_{\mathrm{loop}}}{\Phi_0}\right). \tag{2.53}$$

Plugging this into Eq. (2.51) we get,

$$\frac{\Phi_{\mathrm{loop}}}{\Phi_0} \approx \frac{\Phi_{\mathrm{ext}}}{\Phi_0} \pm \frac{\beta_{\mathrm{L}}}{2} \sin\left(\pi \frac{\Phi_{\mathrm{loop}}}{\Phi_0}\right), \tag{2.54}$$

where we defined the screening parameter

$$\beta_{\mathrm{L}} = \frac{2 L_{\mathrm{loop}} I_{\mathrm{c}}}{\Phi_0} = \frac{L_{\mathrm{loop}}}{\pi L_{\mathrm{j},0}}. \tag{2.55}$$

Solving Eq. (2.54) for $\beta_L > 0$, always yields at least two solutions, corresponding to a clockwise or counterclockwise loop current. These currents either act with or counteract the externally applied flux to ensure that fluxoid quantisation is fulfilled. Consequently, the inductance of a SQUID can exhibit hysteretic behaviour when the sweep direction of the external flux is reversed.

According to usual textbook examples, discrete jumps between solutions only appear for $\beta_{\mathrm{L}} > 2/\pi$, where additional, metastable solutions of Eq. (2.54) exist [55]. However, simulations of the full SQUID potential energy landscape and experimental data show that jumps between possible solutions can also occur for $0 < \beta_{\mathrm{L}} < 2/\pi$ [58].

2.3.3 Cavity tuning behavior

By incorporating a SQUID into the microstrip cavities presented in Section 2.2, the cavity frequency becomes tunable with external flux. Modelling the SQUID cavity with the lumped element model shown in Fig. 2.8 a), we get

$$\omega_{\mathrm{c}}(\Phi_{\mathrm{loop}}) = \frac{1}{\sqrt{C(L + L_{\mathrm{SQUID}}(\Phi_{\mathrm{loop}}))}} \tag{2.56}$$

for the resonance frequency. Using Eq. (2.48) and defining the SQUID participation ratio

$$\beta_{\mathrm{r}} = L_{\mathrm{SQUID},0}/L. \tag{2.57}$$

we can write this as

$$\omega_{\mathrm{c}}(\Phi_{\mathrm{loop}}) = \frac{1}{\sqrt{CL\left(1 + \frac{\beta_{\mathrm{r}}}{|\cos(\pi\Phi_{\mathrm{loop}}/\Phi_0)|}\right)}}. \tag{2.58}$$

Equivalently, we can define the sweetspot frequency $\omega_{\mathrm{c}}(\phi_{\mathrm{loop}} = 0)$, which (as can be seen in Fig. 2.8 b)), differs from the bare cavity frequency $\omega_{\mathrm{c,bare}} = 1/\sqrt{LC}$ by a factor of $1/\sqrt{1+\beta_{\mathrm{r}}}$, and write

$$\omega_{\mathrm{c}}(\Phi_{\mathrm{loop}}) = \frac{\omega_{\mathrm{c}}(\Phi_{\mathrm{loop}} = 0)\sqrt{1+\beta_{\mathrm{r}}}}{\sqrt{1 + \frac{\beta_{\mathrm{r}}}{|\cos(\pi\Phi_{\mathrm{loop}}/\Phi_0)|}}}. \tag{2.59}$$

For SQUIDs with non-negligible screening parameter β_{L}, the hysteretic tuning behaviour with externally applied flux can be obtained by solving Eq. (2.54) for a given external flux Φ_{ext} and shielding parameter β_{L}. As shown in Fig. 2.8 c), this yields solutions for the loop flux Φ_{loop}, which can be plugged into Eq. (2.59), to obtain the possible resonance frequencies.

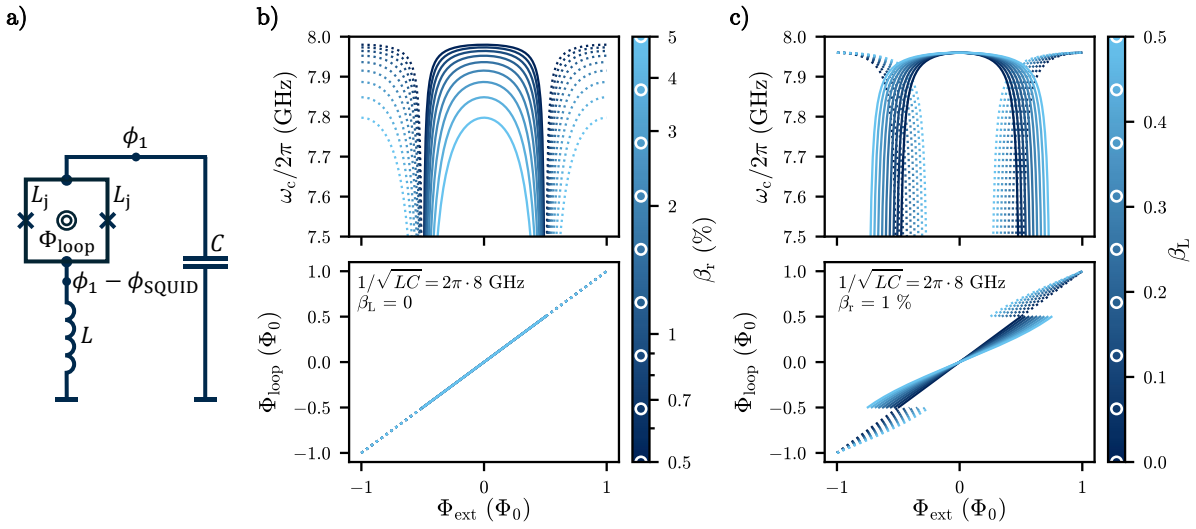

Fig. 2.8 **a)** Lumped element model of a SQUID cavity, neglecting the junction capacitance. **b)** Theoretical tuning behaviour of the SQUID cavity with varying SQUID participation ratio β_r. **c)** In case of a finite linear loop inductance, hence a nonzero screening parameter $\beta_L > 0$, multiple stable solutions (dashed and solid lines) for Φ_{loop} exist around $\Phi_{ext} = \pm 0.5\,\Phi_0$.

2.3.4 Nonlinear Kerr Hamiltonian

As can be seen from Eq. (2.49) and (2.44), the inductance of a SQUID not only depends on the externally applied flux, but also changes with the bias current. With increasing probe power, this current dependence leads to a nonlinear behaviour of SQUID cavities. Up to second order, this nonlinearity can be described with the Kerr constant $\mathcal{K} > 0$ and the Hamiltonian [7, 9]

$$\hat{H} = \hbar\omega_c \hat{a}^\dagger \hat{a} - \hbar\frac{\mathcal{K}}{2}\hat{a}^\dagger\hat{a}^\dagger\hat{a}\hat{a}. \tag{2.60}$$

Calculating the eigenvalues of this Hamiltonian for the Fock states

$$\begin{aligned}
\langle 0|\,\hat{H}\,|0\rangle &= 0 \\
\langle 1|\,\hat{H}\,|1\rangle &= \hbar\omega_c \\
\langle 2|\,\hat{H}\,|2\rangle &= 2\hbar\omega_c - \hbar\mathcal{K} \\
&\vdots \\
\langle n_c|\,\hat{H}\,|n_c\rangle &= n_c\hbar\omega_c - (n_c-1)\hbar\mathcal{K},
\end{aligned} \tag{2.61}$$

we see that, the effective mode frequency

$$\omega_c(n_c) = \langle n_c|\,\hat{H}/\hbar\,|n_c\rangle - \langle n_c - 1|\,\hat{H}/\hbar\,|n_c - 1\rangle = \omega_c(0) - n_c\mathcal{K} \tag{2.62}$$

decreases with the intracavity photon number n_c.

To obtain an expression for $\mathcal{K}$, we will now derive the Hamiltonian of the SQUID cavity. We approximate the microstrip cavity with the lumped element model shown in Fig. 2.8 a) and

neglect the capacitance of the Josephson junctions. The Lagrangian of this circuit is written as

$$\mathcal{L} = \left(\frac{\Phi_0}{2\pi}\right)^2 \left(\frac{C\dot{\phi}_1^2}{2} - \frac{(\phi_1 - \phi_{\mathrm{SQUID}})^2}{2L}\right) + \mathcal{L}_{\mathrm{SQUID}}, \tag{2.63}$$

where $\mathcal{L}_{\mathrm{SQUID}}$ is the Lagrangian of the SQUID. Up to a constant offset, the SQUID potential energy $\mathcal{U}_{\mathrm{SQUID}}$ can be calculated as the time integral

$$\begin{aligned}
\mathcal{U}_{\mathrm{SQUID}} &= \int I_{\mathrm{SQUID}} V_{\mathrm{SQUID}} dt \\
&= \int \left(2I_{\mathrm{c}} \cos\left(\pi\Phi_{\mathrm{loop}}/\Phi_0\right) \sin(\phi_{\mathrm{SQUID}})\right) \left(\frac{\Phi_0}{2\pi}\frac{\partial\phi_{\mathrm{SQUID}}}{\partial t}\right) dt \\
&= -\frac{\Phi_0}{2\pi} 2I_{\mathrm{c}} \cos\left(\pi\Phi_{\mathrm{loop}}/\Phi_0\right) \cos(\phi_{\mathrm{SQUID}}),
\end{aligned} \tag{2.64}$$

where we use the second Josephson equation (Eq. (2.40)) to get the voltage V_{SQUID} over the SQUID. Using Eq. (2.50) and (2.57), we can write this in terms of the SQUID participation ratio β_{r} and the linear cavity inductance L

$$\mathcal{U}_{\mathrm{SQUID}} = -\left(\frac{\Phi_0}{2\pi}\right)^2 \frac{1}{L}\frac{1}{\beta_{\mathrm{r}}} \cos\left(\pi\Phi_{\mathrm{loop}}/\Phi_0\right) \cos(\phi_{\mathrm{SQUID}}). \tag{2.65}$$

Hence, we get for the total Lagrangian of the circuit

$$\mathcal{L} = \left(\frac{\Phi_0}{2\pi}\right)^2 \left(\frac{C\dot{\phi}_1^2}{2} - \frac{(\phi_1 - \phi_{\mathrm{SQUID}})^2}{2L} + \frac{1}{L}\frac{1}{\beta_{\mathrm{r}}} \cos\left(\pi\Phi_{\mathrm{loop}}/\Phi_0\right) \cos(\phi_{\mathrm{SQUID}})\right) \tag{2.66}$$

Due to Kirchoff's law the current through the inductor I_{L} has to equal the bias current through the SQUID I_{SQUID}, therefore we get that

$$\begin{aligned}
I_{\mathrm{L}} &= I_{\mathrm{SQUID}} \\
\frac{\Phi_0}{2\pi}\frac{\phi_1 - \phi_{\mathrm{SQUID}}}{L} &= 2I_{\mathrm{c}} \cos\left(\pi\Phi_{\mathrm{loop}}/\Phi_0\right) \sin(\phi_{\mathrm{SQUID}}) \\
\phi_1 - \phi_{\mathrm{SQUID}} &= \underbrace{\frac{1}{\beta_{\mathrm{r}}} \cos\left(\pi\Phi_{\mathrm{loop}}/\Phi_0\right)}_{B_{\mathrm{r}}} \sin(\phi_{\mathrm{SQUID}}),
\end{aligned} \tag{2.67}$$

where we define the inverse of the effective SQUID participation ratio as B_{r}. For a small phase drop over the SQUID, we can Taylor expand $\sin(\phi_{\mathrm{SQUID}})$ and get

$$\phi_1 - \phi_{\mathrm{SQUID}} = B_{\mathrm{r}} \left(\phi_{\mathrm{SQUID}} - \frac{1}{6}\phi_{\mathrm{SQUID}}^3 + O(\phi_{\mathrm{SQUID}}^5)\right). \tag{2.68}$$

To obtain an expression for ϕ_{SQUID}, we use the polynomial ansatz

$$\phi_{\mathrm{SQUID}} = a\phi_1 + b\phi_1^2 + c\phi_1^3 + d\phi_1^4 + O(\phi_1^5). \tag{2.69}$$

After inserting this into Eq. (2.68), comparison of coefficients yields

$$\phi_{\mathrm{SQUID}} = \frac{1}{B_{\mathrm{r}} + 1}\phi_1 + \frac{B_{\mathrm{r}}}{6(B_{\mathrm{r}} + 1)^4}\phi_1^3 + O(\phi_1^5). \tag{2.70}$$

Inserting this into the Lagrangian after Taylor expanding $\cos(\phi_{\mathrm{SQUID}})$ gives

$$\begin{aligned}\mathcal{L} = \left(\frac{\Phi_0}{2\pi}\right)^2 \Bigg(& \frac{C\dot{\phi}_1^2}{2} - \frac{1}{2L}\left(\frac{B_\mathrm{r}^2}{(B_\mathrm{r}+1)^2}\phi_1^2 - \frac{B_\mathrm{r}^2}{3(B_\mathrm{r}+1)^5}\phi_1^4\right) \\ & + \frac{1}{L}\left(1 - \frac{B_\mathrm{r}}{2(B_\mathrm{r}+1)^2}\phi_1^2 - \frac{3B_\mathrm{r}^2 - B_\mathrm{r}}{24(B_\mathrm{r}+1)^5}\phi_1^4\right)\Bigg) + O(\phi_1^5).\end{aligned} \tag{2.71}$$

Doing a Legendre transformation and replacing the phase $\phi_1 \to \hat{\phi}_1$ with its quantum operator yields the Hamiltonian

$$\begin{aligned}\hat{H} = \left(\frac{\Phi_0}{2\pi}\right)^2 \Bigg(& \frac{C\dot{\hat{\phi}}_1^2}{2} + \frac{1}{2L}\left(\frac{B_\mathrm{r}^2}{(B_\mathrm{r}+1)^2}\hat{\phi}_1^2 - \frac{B_\mathrm{r}^2}{3(B_\mathrm{r}+1)^5}\hat{\phi}_1^4\right) \\ & + \frac{1}{L}\left(\frac{B_\mathrm{r}}{2(B_\mathrm{r}+1)^2}\hat{\phi}_1^2 + \frac{3B_\mathrm{r}^2 - B_\mathrm{r}}{24(B_\mathrm{r}+1)^5}\hat{\phi}_1^4\right)\Bigg) + O(\hat{\phi}_1^5),\end{aligned} \tag{2.72}$$

where we omit constant energy terms. To express this Hamiltonian in second quantisation, we use the definition of the ladder operator

$$\hat{a} = \frac{\Phi_0}{2\pi}\left(\sqrt{\frac{C\omega_{\mathrm{c,bare}}}{2\hbar}}\hat{\phi}_1 + i\sqrt{\frac{C}{2\hbar\omega_{\mathrm{c,bare}}}}\dot{\hat{\phi}}_1\right), \quad \text{with} \quad \omega_{\mathrm{c,bare}} = \frac{1}{\sqrt{LC}}, \tag{2.73}$$

and obtain

$$\hat{\phi}_1 = \frac{2\pi}{\Phi_0}\frac{1}{2}\sqrt{\frac{2\hbar}{C\omega_{\mathrm{c,bare}}}}(\hat{a} + \hat{a}^\dagger) \quad \text{and} \quad \dot{\hat{\phi}}_1 = \frac{2\pi}{\Phi_0}\frac{1}{2i}\sqrt{\frac{2\hbar\omega_{\mathrm{c,bare}}}{C}}(\hat{a} - \hat{a}^\dagger). \tag{2.74}$$

Inserting this into the Hamiltonian (Eq. (2.72)) and collecting terms which are diagonal in the Fock-basis yields

$$\begin{aligned}\hat{H} = & \hbar\left[\frac{\omega_{\mathrm{c,bare}}}{2}\left(1 + \frac{B_\mathrm{r}}{B_\mathrm{r}+1}\right) - \left(\frac{2\pi}{\Phi_0}\right)^2 \frac{1}{8}\frac{B_\mathrm{r}}{(1+B_\mathrm{r})^4}\hbar\omega_{\mathrm{c,bare}}^2 L\right]\hat{a}^\dagger\hat{a} \\ & - \hbar\frac{1}{2}\left[\left(\frac{2\pi}{\Phi_0}\right)^2 \frac{1}{8}\frac{B_\mathrm{r}}{(1+B_\mathrm{r})^4}\hbar\omega_{\mathrm{c,bare}}^2 L\right]\hat{a}^\dagger\hat{a}^\dagger\hat{a}\hat{a}\end{aligned} \tag{2.75}$$

Comparing this to the initially defined Hamiltonian (Eq. (2.60)), we find

$$\mathcal{K} = \left(\frac{2\pi}{\Phi_0}\right)^2 \frac{1}{8}\frac{B_\mathrm{r}}{(1+B_\mathrm{r})^4}\hbar\omega_{\mathrm{c,bare}}^2 L \tag{2.76}$$

and

$$\omega_\mathrm{c} = \frac{\omega_{\mathrm{c,bare}}}{2}\left(1 + \frac{B_\mathrm{r}}{B_\mathrm{r}+1}\right) - \mathcal{K}, \tag{2.77}$$

For $B_\mathrm{r} \gg 1$, corresponding to $\beta_\mathrm{r}/\cos(\pi\Phi_{\mathrm{loop}}/\Phi_0) \ll 1$, the obtained expression for the cavity frequency ω_c is equivalent to the expression derived in Section 2.3.3 (Eq. (2.59)). In this regime of small effective SQUID participation ratio, we see that the Kerr constant scales as $\mathcal{K} \propto 1/B_\mathrm{r}^3 = \beta_\mathrm{r}^3/\cos^3(\pi\Phi_{\mathrm{loop}}/\Phi_0)$.

2.3.5 Simulation in *scQubits*

To validate the analytical expressions for ω_c and $\mathcal{K}$, and to investigate the effect of neglecting the junction capacitance, we simulate the circuit using *scQubits* [59]. For the parameters of the simulation, we use typical values for our SQUID cavities. The value for the linear inductance L was obtained by R. Sathyanarayanan by simulating the design of the microstrip in *Ansys HFSS*.

The results of the simulation are shown in Fig. 2.9. As the cavity is tuned away from its flux sweet spot, the frequency decreases and the Kerr nonlinearity $\mathcal{K}$ increases due to the increased nonlinear SQUID inductance. For small junction capacitance C_J, the analytical models (Eq.(2.59) and Eq.(2.76)) show good agreement with the simulation results. For larger C_J, slight deviations from the predictions appear, particularly at higher SQUID participation ratios β_r.

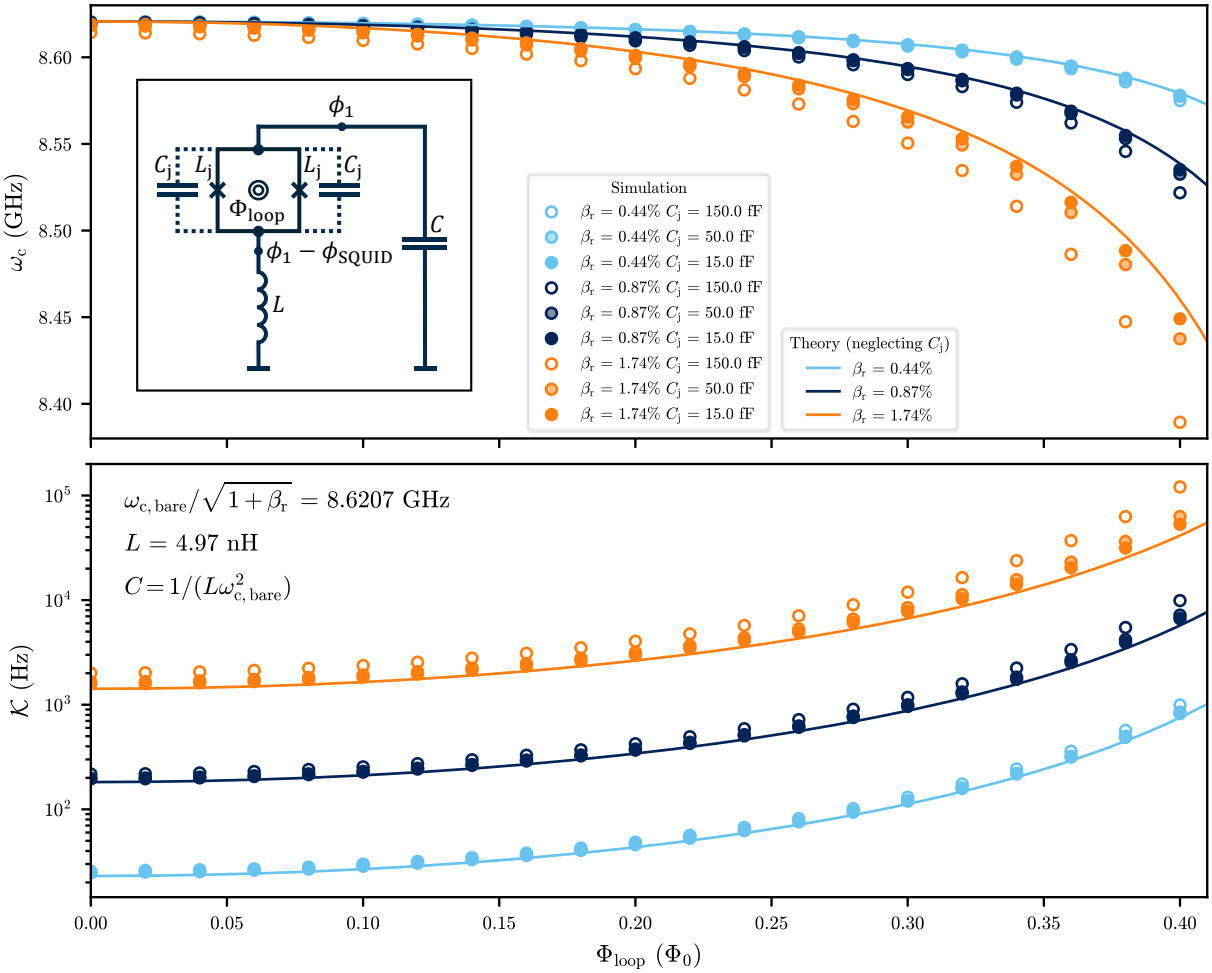

Fig. 2.9 Simulated frequency and Kerr of a SQUID cavity using *scQubits* [59]. Colours indicate different SQUID participation ratios, and markers correspond to varying junction capacitances. Solid lines show the analytical models Eq. (2.59) and Eq. (2.76), derived in Section 2.3.3 and Section 2.3.4 respectively. The inset shows the lumped element model of a SQUID cavity, including the capacitance of the junctions, which we neglect in the derivation of the analytical models.

2.4 External loss - Coupling the cavity to a waveguide

To interact with the cavity and subsequently detect and manipulate the mechanical motion, we couple it to the field within a rectangular waveguide, as shown schematically in Fig. 2.10. The electric field of the fundamental propagating TE_{10} waveguide mode is given by [50, 60]

$$\vec{E} = E_0 \cos(\pi d / w_{\mathrm{WG}}) \hat{e}_y. \tag{2.78}$$

Placing the cavity at a distance d from the centre of the waveguide creates an electric field difference between the cavity legs. For $d_{\mathrm{L}} \ll w_{\mathrm{WG}}$, the difference in electric field at the position of the two legs can be approximated as

$$\Delta E \approx d_{\mathrm{L}} \frac{\partial E}{\partial d} \propto \sin(\pi d / w_{\mathrm{WG}}). \tag{2.79}$$

This difference in electric field causes a capacitive coupling of the cavity to the waveguide mode, as illustrated in Fig. 2.10 b). The coupling introduces a loss channel for the cavity, characterised by the external or coupling linewidth

$$\kappa_{\mathrm{c}} \propto \Delta E \propto \sin(\pi d / w_{\mathrm{WG}}). \tag{2.80}$$

As the difference in electric field ΔE increases with the distance d from the centre of the waveguide, we can tune the coupling for a given chip by changing its x-position.

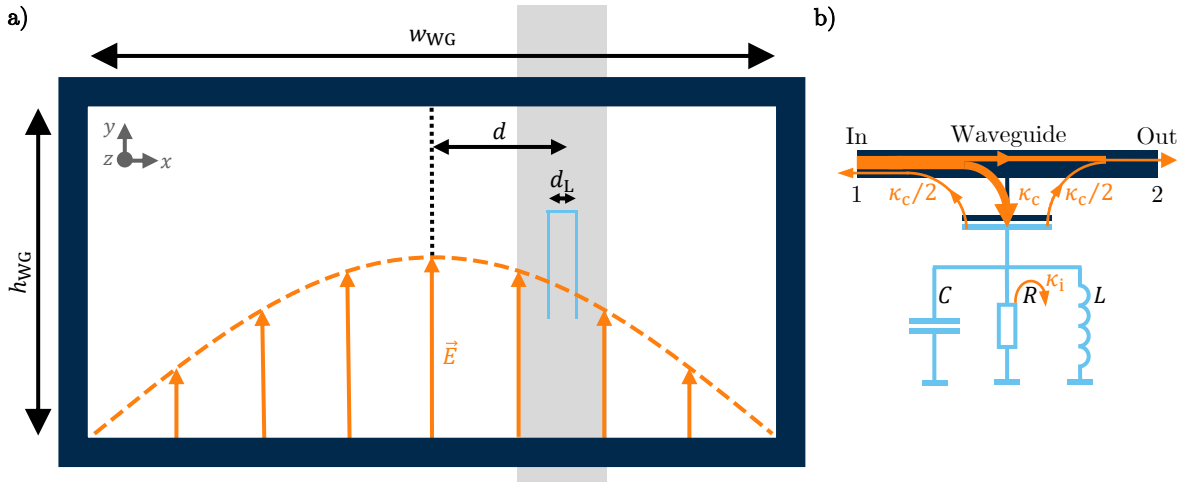

Fig. 2.10 **a)** Schematic representation of a cut through the rectangular waveguide, normal to the propagating mode direction. In orange, we plot the electric field for the fundamental TE_{01} waveguide mode. The electric field difference between the cavity legs causes a capacitive coupling to the waveguide mode, which can be tuned by changing the chip position d. **b)** Circuit representation of the cavity in the waveguide, capacitively coupled to the waveguide mode at a loss rate κ_{c}. The additional resistor represents internal loss κ_{i}. Orange arrows show the path of an incoming, near-resonant probe tone. Half of the signal coming from the cavity is reflected back to the waveguide input, while the other half, phase-shifted signal interferes with the uncoupled part of the probe tone towards the output.

2.5 Internal loss mechanisms of the cavity

Apart from the deliberately introduced loss to the waveguide, which provides information about the system and is essential for control, the microwave cavity also experiences internal losses.

One internal loss mechanism is conductive loss. Below the superconducting transition temperature, the remaining ratio of unpaired electrons causes dissipation [52, 61]. Especially in external magnetic fields, reduced Cooper pair density and trapped flux vortices can impact the performance of superconducting cavities [62–64]. Additionally, a normal conducting material in close proximity to the cavity can lead to the induction of dissipative eddy currents [65].

Dielectric materials, like the silicon substrate, oxide layers on material surfaces or the junction barrier [66], as well as residual materials from the fabrication process e.g. photoresist, introduce additional loss channels [62]. Superconductors like aluminium or niobium form oxide layers on their surfaces when exposed to air. Two-level systems (TLS) can reside in such amorphous oxide layers [67] or in other insulating layers which might be used in multilayer fabrication processes [68]. The interaction of these TLSs with the electric field of the superconducting cavity leads to the loss of photons.

A combination of these internal loss mechanisms broadens the linewidth of the cavity by the internal linewidth κ_i. Together with the external linewidth κ_c, κ_i contributes to the total or loaded cavity linewidth

$$\kappa_\mathrm{l} = \kappa_\mathrm{i} + \kappa_c. \tag{2.81}$$

To compare the performance of different cavities, these linewidths are often normalised to the cavity resonance frequency ω_c and expressed in terms of quality factors

$$Q_x = \frac{\omega_\mathrm{c}}{\kappa_x}, \tag{2.82}$$

where Q_x represents the relevant quality factor, depending on whether κ_x refers to the internal, external, or total linewidth.

2.6 Cavity scattering parameters

To obtain the internal and external quality factors of a cavity, the S_{21} scattering parameter can be measured. The obtained data can then be fitted using a so-called circle fit routine [45, 69].

2.6.1 Linear circle fit

The transmission of a probe tone with frequency ω_p through a waveguide, coupled to a cavity with frequency ω_c, can be described by the complex scattering parameter [45, 69]

$$S_{21}(\omega_\mathrm{p}) = a e^{i\alpha} e^{-i\omega_\mathrm{p}\tau} \left(1 - \frac{(Q_\mathrm{l}/|Q_\mathrm{c}|)\cdot e^{i\varphi}}{1 + 2iQ_\mathrm{l}(\omega_\mathrm{p}/\omega_\mathrm{c} - 1)}\right). \tag{2.83}$$

Here, the second term in brackets describes the scattering of the cavity with loaded quality factor $Q_\mathrm{l} = \omega_\mathrm{c}/\kappa_\mathrm{l}$ and complex coupling quality factor $Q_\mathrm{c} = |Q_\mathrm{c}|e^{-i\varphi}$. Regarding Q_c as a complex value takes into account the possibility of an impedance mismatch φ between the cavity and the waveguide. The first term accounts for the so-called environment or background [69], an overall

attenuation a, a phase offset α and a delay τ, caused by the waveguide, cables, attenuators and other components between the cavity and the measurement device.

After correcting for the background, as detailed in Ref. [69], the second term corresponds to a circle with diameter $Q_\mathrm{l}/|Q_\mathrm{c}|$ in the complex plane. By fitting this circle to background corrected scattering data, the loaded quality factor Q_l and complex coupling quality factor Q_c of a cavity can be obtained. The internal quality factor can then be calculated as [45]

$$Q_\mathrm{i} = (Q_\mathrm{l}^{-1} - Q_\mathrm{c,eff}^{-1})^{-1}, \tag{2.84}$$

wherein we define an effective coupling quality factor

$$Q_\mathrm{c,eff} = |Q_\mathrm{c}|/\cos(\phi). \tag{2.85}$$

The factor $1/\cos(\varphi)$ corrects for a potential impedance mismatch [45].

In Fig. 2.11 a), the background-corrected cavity response is simulated for different effective coupling quality factors $Q_\mathrm{c,eff}$. For increasing coupling (decreasing $Q_\mathrm{c,eff}$), the dip in $|S_{21}|$ gets deeper and the cavity linewidth increases. On the complex plane, this manifests as an increasing

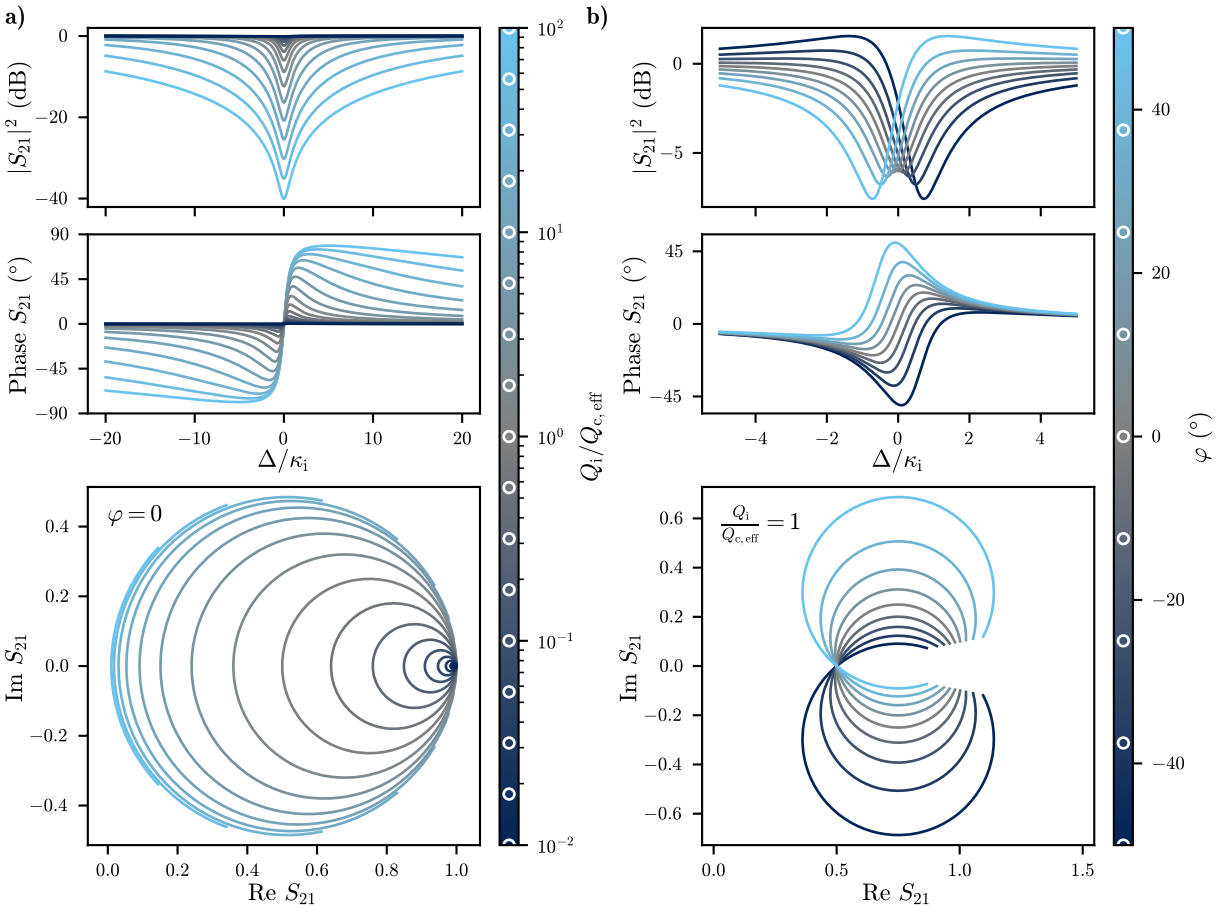

Fig. 2.11 Theroy curves for the S_{21} scattering parameter of a linear cavity for **a)** different effective coupling quality factors $Q_\mathrm{c,eff}$ and **b)** impedance mismatches φ.

radius of the circle. In the overcoupled regime $Q_\mathrm{i}/Q_\mathrm{c,eff} < 1$, the total cavity linewidht κ_l is dominated by external loss, while internal loss dominates in the undercoupled regime $Q_\mathrm{i}/Q_\mathrm{c,eff} > 1$. For a criticaly coupled cavity, where $Q_\mathrm{i}/Q_\mathrm{c,eff} = 1$, internal and external loss equally contribute to κ_l. Note that we set the impedance mismatch $\varphi = 0$ in this subfigure, so the complex coupling quality factor has no imaginary part and $Q_\mathrm{c,eff} = |Q_\mathrm{c}| = Q_\mathrm{c}$.

In Fig. 2.11 b), the response of a critically coupled cavity is plotted for varying impedance mismatch φ. As can be seen, impedance mismatch leads to an asymmetric resonance and a frequency-shifted minimum of $|S_{21}|$. In the complex plane, this appears as a rotation and scaling of the circle. Since all traces correspond to a cavity with the same internal quality factor, the varying circle diameters highlight the necessity of accounting for impedance mismatch when extracting the internal cavity quality factor [45].

An example demonstrating a circle fit applied to experimental data is shown in Fig. 3.4.

2.6.2 Nonlinear circle fit

As discussed in Section 2.3.4, the SQUID introduces an intrinsic nonlinearity. For large probe powers, this leads to a nonlinear behaviour of tunable SQUID cavities. The effective resonance frequency

$$\omega_\mathrm{c}(n_\mathrm{c}) = \omega_\mathrm{c}(0) - \mathcal{K} n_\mathrm{c}, \tag{2.86}$$

shifts with the intracavity photon number n_c and the Kerr constant $\mathcal{K} > 0$.

As mentioned in Section 2.1.3, for a given probe frequency ω_p, the mean intracavity photon number $\bar{n}_\mathrm{c}$ of a Kerr cavity can be obtained by solving the cubic equation

$$\bar{n}_\mathrm{c}\left((\omega_\mathrm{p} - \omega_\mathrm{c}(\bar{n}_\mathrm{c}))^2 + \frac{\kappa_l^2}{4}\right) = \frac{\kappa_c}{2} 2\pi \bar{n}_\mathrm{in}, \tag{2.87}$$

with $\bar{n}_\mathrm{in} = P_\mathrm{in}/\hbar\omega_\mathrm{p}$, the mean input photon number rate, calculated from the microwave power P_in that reaches the cavity. When the input photon rate exceeds the threshold

$$\bar{n}_\mathrm{in} > \bar{n}_\mathrm{in,bi} = \frac{1}{2\pi}\frac{2\kappa_\mathrm{l}}{\kappa_\mathrm{c}}\frac{\kappa_\mathrm{l}^2}{3\sqrt{3}\mathcal{K}}, \tag{2.88}$$

the cavity becomes bistable and two solutions for $\bar{n}_\mathrm{c}$ exist.

Inserting the steady state solutions for the resonance frequency $\omega_\mathrm{c}(\bar{n}_\mathrm{c})$ at different probe frequencies ω_p in the formula for the scattering parameter of a linear cavity (Eq. (2.83)), yields the scattering parameter for the nonlinear case [9]

$$S_{21}(\omega_\mathrm{p}) = a e^{i\alpha} e^{-i\omega_\mathrm{p}\tau}\left(1 - \frac{(Q_\mathrm{l}/|Q_\mathrm{c}|)\cdot e^{i\varphi}}{1 + 2iQ_\mathrm{l}(\omega_\mathrm{p}/\omega_\mathrm{c}(\bar{n}_\mathrm{c}(\omega_\mathrm{p})) - 1)}\right). \tag{2.89}$$

Fig. 2.12 shows the steady state photon number and the scattering parameter of a Kerr cavity, plotted against the probe frequency. With increasing power, the Kerr dependent frequency shift results in a steep slope at negative detunings and a more gradual slope for positive detunings, producing an asymmetric resonance profile that resembles a shark fin.

This asymmetry arises from the dependence of the intracavity photon number on the effective detuning $\omega_\mathrm{p} - \omega_\mathrm{c}(n_\mathrm{c})$ between the probe tone and the cavity [5]. For negative effective detunings, the cavity frequency shifts towards the probe tone, which brings it closer to resonance. This increases the number of photons and shifts the cavity even closer to the probe until a steady state is reached. On the other hand, for positive effective detunings, the cavity shifts away from the probe, which decreases the photon number and shifts the cavity even further away, until a steady state is reached. The time constant required to reach the steady state is thereby on the order of the lifetime of the photons in the cavity, given by the inverse of the total cavity linewidth.

When the probe power exceeds the bistable threshold, the steady-state photon number no longer depends solely on the instantaneous probe frequency but also on the prior evolution of the intracavity photon number. Sweeping the probe tone from negative towards positive detunings leads to the cavity settling on the low photon number branch, whereas sweeping from positive to negative detunings results in the high photon number branch being occupied. As shown in Fig. 2.12, this results in two distinct cavity responses (solid and dashed lines), depending on the direction of the frequency sweep

In Section 3.4, we will show how fitting Eq. (2.89) to measured scattering data allows us to determine the Kerr constant.

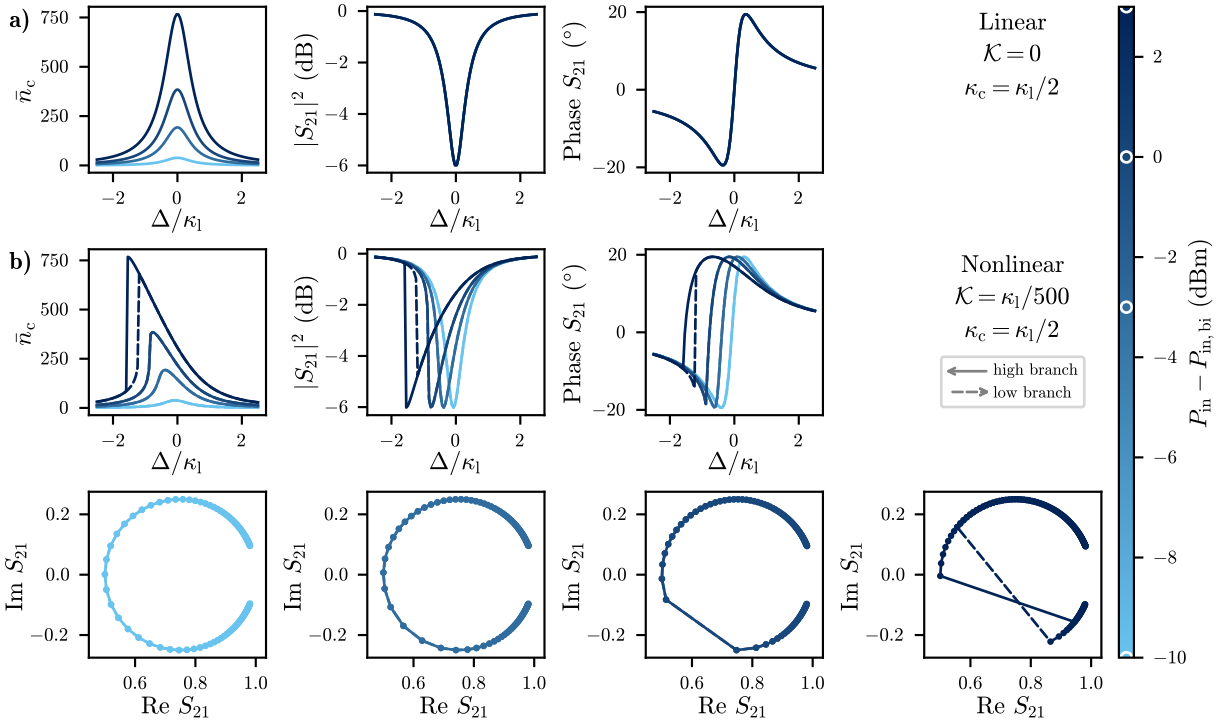

Fig. 2.12 Theory curves for the S_{21} scattering parameter of **a)** a linear cavity with $\mathcal{K} = 0$ and **b)** a nonlinear cavity with $\mathcal{K} = \kappa_1/500$. Above the bistable input power, the intracavity photon number can settle into either a low or high photon number branch (dashed and solid lines). Depending on the sweep direction of the probe frequency (arrows in legend), this leads to a different scattering parameter of the cavity. Markers in the complex S_{21} plane visualise equidistant frequency points.

2.7 Inductive coupling to a mechanical resonator

To build an optomechanical system, we need to couple our cavity to the motion of a mechanical object. For an LC circuit, this is typically achieved by using the motion of a mechanical object to either change the capacitance [70–74] or the inductance [2, 75] of the circuit. Similar to the case of the optical cavity with one suspended mirror, discussed in Section 2.1, the coupling strength

$$g_0 = -x_{\mathrm{ZPF}}\partial\omega_{\mathrm{c}}/\partial\hat{x} \tag{2.90}$$

depends on how much a single zero point fluctuation in the mechanical object's position changes the LC circuit's resonance frequency. Since a SQUID's inductance is highly susceptible to magnetic flux changes, it enables significant frequency shifts even for tiny movements of a magnetic object. This sensitivity makes SQUIDs perfectly suited for optomechanical systems [2, 75–79].

Fig. 2.13 a) shows a schematic representation of a tunable SQUID cavity, coupled to a silicon atomic force microscope (AFM) cantilever with an attached magnetic particle. As the cantilever oscillates, the distance between the SQUID and the particle changes, modulating the magnetic flux threading the SQUID loop. As illustrated in Fig. 2.13 b), modulation of the external flux leads to modulation of the cavity frequency, introducing a coupling

$$g_0 = -x_{\mathrm{ZPF}}\frac{\partial\omega_{\mathrm{c}}}{\partial\hat{x}} = -x_{\mathrm{ZPF}}\frac{\partial\omega_{\mathrm{c}}}{\partial\Phi_{\mathrm{ext}}}\frac{\partial\Phi_{\mathrm{ext}}}{\partial\hat{x}}, \tag{2.91}$$

which to first order is proportional to the slope $\partial\omega_{\mathrm{c}}/\partial\Phi_{\mathrm{ext}}$, and can therefore be tuned in situ by applying an external flux bias field. If the bias field is sufficiently stable and the system is well-shielded from external noise, operation at steep flux bias points enables exceptionally large single-photon coupling strengths, surpassing typical capacitive coupling schemes [6].

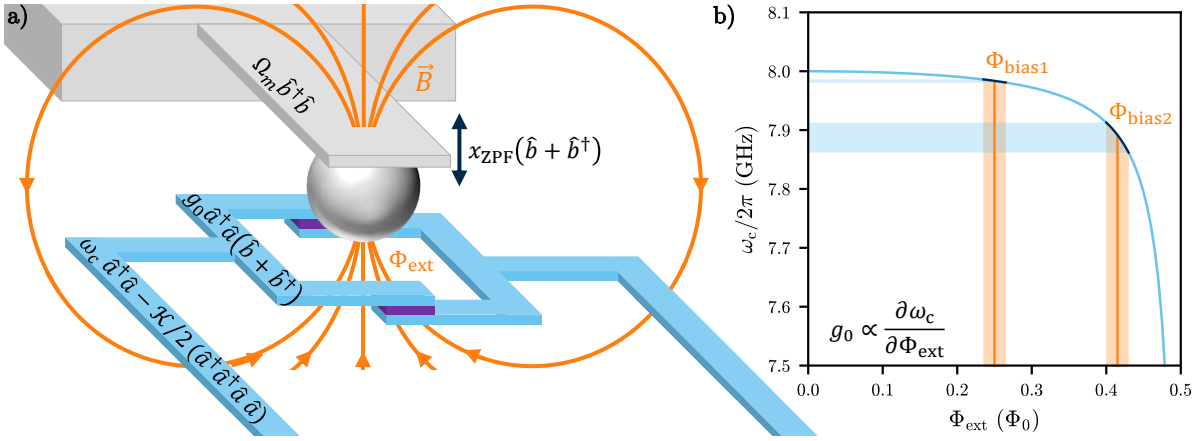

Fig. 2.13 **a)** Schematic representation of a cantilever with magnetic particle, inductively coupled to a tunable stripline cavity. Oscillation of the cantilever changes the distance between the SQUID and the magnetic particle, which leads to a modulation of the magnetic flux threading the SQUID loop. **b)** Typical tuning behaviour of a SQUID cavity with externally applied flux (Eq. (2.59)). The cantilever modulates the external flux, leading to a modulation of the cavity frequency. Applying an additional external flux bias Φ_{bias}, allows to tune the optomechanical coupling strength in situ, $g_0(\Phi_{\mathrm{bias2}}) > g_0(\Phi_{\mathrm{bias1}})$.

2.7.1 Bending modes of a cantilever

For small deflections, the bending modes of a thin, uniform cantilever beam of length l_{beam} can be derived using Euler-Bernouli beam theory [80, 81]. The normalised deflection amplitude $D_n(l)$, perpendicular to the beam's long axis l, is given by

$$D_n(l) = \frac{(\cos(\lambda_n l/l_{\text{beam}}) - \cosh(\lambda_n l/l_{\text{beam}})) + \gamma\,(\sin(\lambda_n l/l_{\text{beam}}) - \sinh(\lambda_n l/l_{\text{beam}}))}{(\cos(\lambda_n) - \cosh(\lambda_n)) + \gamma\,(\sin(\lambda_n) - \sinh(\lambda_n))}, \tag{2.92}$$

wherein

$$\gamma = (\sin(\lambda_n) - \sinh(\lambda_n))/(\cos(\lambda_n) + \cosh(\lambda_n)). \tag{2.93}$$

The parameter λ_n for the n-th bending mode can be obtained by solving

$$1 + \cosh(\lambda_n)\cos(\lambda_n) = 0 \quad \Rightarrow \quad \lambda_1 \approx 1.8751,\ \lambda_2 \approx 4.6941,\ \lambda_3 \approx 7.8548,\ \ldots\ . \tag{2.94}$$

The normalised mode shapes of the first three modes are plotted in Fig. 2.14 a). The corresponding mode frequencies are given by

$$\Omega_{\text{m}}^{(n)} = \frac{\lambda_n^2}{l_{\text{beam}}^2}\sqrt{\frac{EI}{\rho A}}, \tag{2.95}$$

where E is the Young's-modulus, I is the area moment of inertia, ρ is the density and A is the beam's cross-section. For a beam with a rectangular cross-section of width w_{beam} and thickness t_{beam}, the area moment of inertia is given by $I = w_{\text{beam}} t_{\text{beam}}^3/12$. Inserting the obtained values for λ_n, we see that the second mode has ≈ 6.27 and the third mode ≈ 17.55 times the frequency of the fundamental mode.

To model the cantilever with total mass $m_{\text{beam}} = \rho A l_{\text{beam}}$ as a spring-mass system, we define its effective mass as

$$m_{\text{eff}}^{(n)} = \int_0^{l_{\text{beam}}} (D_n(l))^2 \rho A dl = \frac{m_{\text{beam}}}{l_{\text{beam}}} \int_0^{l_{\text{beam}}} (D_n(l))^2 dl, \tag{2.96}$$

where we scale each infinitesimal element of the beam with the square of the normalised deflection amplitude [82]. This takes into account that different parts of the cantilever contribute differently

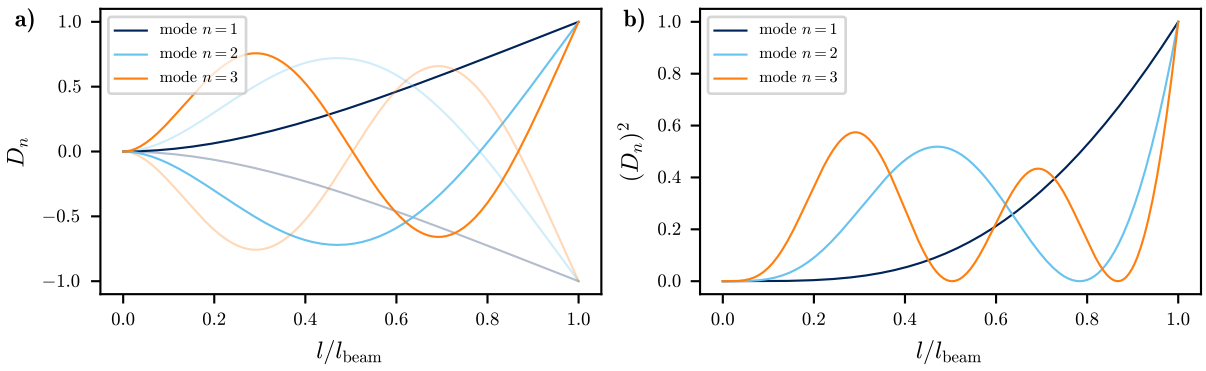

Fig. 2.14 **a)** Normalised deflection amplitudes (mode shapes) of a cantilever beam, as given by Eq. (2.92). **b)** Squared normalised deflection amplitude, proportional to the ratio of effective to real mass of an infinitesimal beam element. Integrating these functions yields the ratio of the effective to the total mass of the cantilever.

to the kinetic energy of the oscillation. The squared, normalised deflection amplitudes are plotted in Fig. 2.14 b). Numerical integration yields that, mostly independent of the mode order n,

$$m_{\mathrm{eff}} \approx m_{\mathrm{beam}}/4. \tag{2.97}$$

Thus, only about one-quarter of the cantilever's total mass effectively contributes to its motion. Using this result, we can express the mode frequencies as

$$\Omega_{\mathrm{m}}^{(n)} = \frac{\lambda_n^2}{\lambda_1^2}\sqrt{\frac{k}{m_{\mathrm{eff}}}}, \tag{2.98}$$

where, by comparing with Eq. (2.95), the effective spring constant of the cantilever is

$$k = \frac{\lambda_1^4}{12}\frac{E w_{\mathrm{beam}} t_{\mathrm{beam}}^3}{4 \cdot l_{\mathrm{beam}}^3} \approx \frac{E w_{\mathrm{beam}} t_{\mathrm{beam}}^3}{4 \cdot l_{\mathrm{beam}}^3}. \tag{2.99}$$

For µm-sized, commercially available silicon cantilevers, which are commonly used in AFMs, this results in fundamental frequencies ranging from 10 kHz to 500 kHz [83].

Considering the different cantilever mode frequencies and assuming all modes are thermalised to a bath temperature T, the absolute maximum deflection amplitudes are smaller for higher-order modes. In the limit $k_{\mathrm{B}}T \gg \hbar\Omega_{\mathrm{m}}^{(n)}$, the deflection amplitude of the n-th mode scales as

$$\frac{\hat{x}^{(n)}}{\hat{x}^{(1)}} = \frac{x_{\mathrm{ZPF}}^{(n)}\sqrt{\bar{n}_{\mathrm{m}}^{\mathrm{th}(n)}}}{x_{\mathrm{ZPF}}^{(1)}\sqrt{\bar{n}_{\mathrm{m}}^{\mathrm{th}(1)}}} = \frac{\Omega_{\mathrm{m}}^{(1)}}{\Omega_{\mathrm{m}}^{(n)}} \propto \frac{1}{\Omega_{\mathrm{m}}^{(n)}}, \tag{2.100}$$

relative to the fundamental mode. Here we use that in the limit $k_{\mathrm{B}}T \gg \hbar\Omega_{\mathrm{m}}^{(n)}$, the thermal occupation behaves as $1/\Omega_{\mathrm{m}}^{(n)}$ (see Eq. (2.17)) and the respective zeropoint fluctuation amplitudes scale with the square root of $1/\Omega_{\mathrm{m}}^{(n)}$ (see Eq. (2.2)). The corresponding scaled mode shapes are plotted in Fig. 2.15 a).

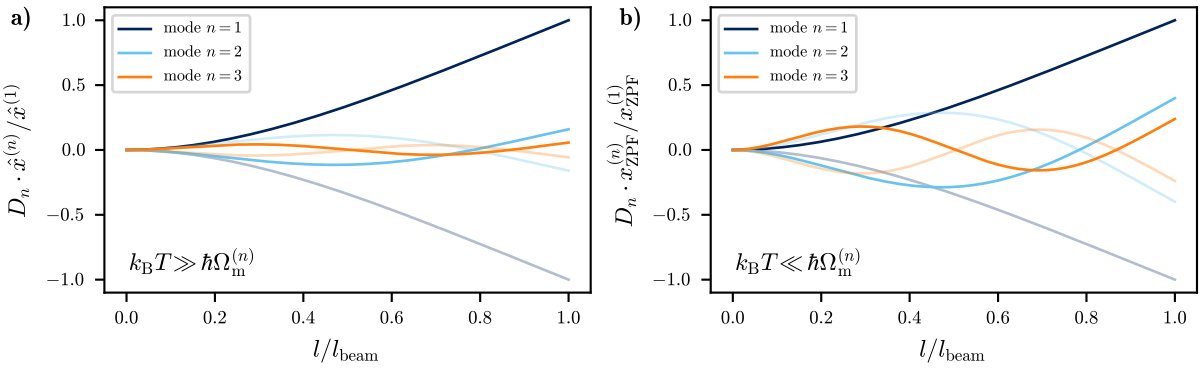

Fig. 2.15 **(a)** Relative thermal deflection amplitudes of a uniform cantilever beam, normalised to the amplitude of the fundamental mode. The amplitudes are calculated assuming that all modes are thermalised to a bath at temperature T in the limit $k_{\mathrm{B}}T \gg \hbar\Omega_{\mathrm{m}}^{(n)}$ (Eq. 2.100) **(b)** Relative thermal deflection amplitudes of the cantilever modes near the quantum ground state (Eq. 2.101).

Close to the ground state, the cantilever motion is only given by the zero-point fluctuation amplitudes of the individual modes

$$\frac{\hat{x}^{(n)}}{\hat{x}^{(1)}} = \frac{x_{\mathrm{ZPF}}^{(n)}}{x_{\mathrm{ZPF}}^{(1)}} = \sqrt{\frac{\Omega_{\mathrm{m}}^{(1)}}{\Omega_{\mathrm{m}}^{(n)}}} \propto \frac{1}{\sqrt{\Omega_{\mathrm{m}}^{(n)}}}. \tag{2.101}$$

The corresponding scaled mode shapes are plotted in Fig. 2.15 b).

2.7.1.1 Attaching a magnetic particle

As schematically shown in Fig. 2.7 a), a magnetic particle is attached to the cantilever for inductive coupling to the SQUID cavity. Approximating the particle as a point mass m_{p}, sitting exactly at the free end of the cantilever, yields a cantilever frequency of [5]

$$\tilde{\Omega}_{\mathrm{m}}^{(n)} = \frac{\lambda_n^2}{\lambda_1^2}\sqrt{\frac{k}{m_{\mathrm{eff}} + m_{\mathrm{p}}}}. \tag{2.102}$$

If the particle does not sit at the very end of the cantilever, but at some distance $l_{\mathrm{p}} < l_{\mathrm{beam}}$ from the cantilever's fixed end, only the effective mass $m_{\mathrm{p,eff}}$ of the particle contributes to the shift in resonance frequency

$$\tilde{\Omega}_{\mathrm{m}}^{(n)}(l_{\mathrm{p}}) = \frac{\lambda_n^2}{\lambda_1^2}\sqrt{\frac{k}{m_{\mathrm{eff}} + m_{\mathrm{p,eff}}^{(n)}(l_{\mathrm{p}})}}. \tag{2.103}$$

Assuming the particle does not change the mode shape, its effective mass can be calculated as

$$m_{\mathrm{p,eff}}^{(n)} = m_{\mathrm{p}}(D_n(l_{\mathrm{p}}))^2. \tag{2.104}$$

For elongated particles with a non-negligible size along the beam direction, integrating over the particle's mass distribution might be required for a more accurate estimate of the effective mass. Again, looking at the squared mode shapes, plotted in Fig. 2.14 b), we see that placing the particle further away from the free end of the cantilever would be beneficial to keep the effective mass of the particle low and maintain a higher mechanical frequency. This would reduce the thermal occupation and could make optomechanical cooling more efficient.

However, beyond modifying the resonance frequency, the position of the particle also influences the coupling to the SQUID cavity. Moving the particle away from the free end of the cantilever reduces its oscillation amplitude, thereby lowering the optomechanical coupling. While this results in a gradual decrease in coupling for the fundamental mode, higher-order modes may exhibit no coupling at all if the particle is positioned at a node of the oscillation. Moreover, the smaller absolute deflection amplitude of higher-order modes, shown in Fig. 2.15, might lead to a smaller optomechanical coupling than for the fundamental mode. Here we also want to point out that, for larger particles, the assumption that the mode shape remains unchanged will no longer be valid. In particular, higher-order modes are sensitive to added mass [84] and may adapt their shape to minimise the overall energy.

CHAPTER 3

Characterisation of frequency tunable microwave cavities

In this chapter, we present the experimental results from the characterisation of a batch of SQUID niobium microstrip cavities fabricated by *STAR Cryoelectronics*. We begin by introducing the experimental setup, which consists of a rectangular copper waveguide mounted on the baseplate of a dilution refrigerator. We briefly discuss the fabrication process of the cavities, which are coupled to the field in the waveguide.

Over several cooldowns, we investigate the tunability of the coupling to the waveguide by varying the positions of the samples. Furthermore, we discuss possible limiting factors for the obtained internal cavity quality factors. We analyse the tuning behaviour with external flux by fitting it with the model derived in Section 2.3.3. This allows us to determine the SQUID participation ratio (β_r) and the shielding parameter (β_L). We discuss the observed spread in these parameters for the different cavities. Subsequently, we examine how the internal quality factor varies with flux bias.

Finally, we explore the behaviour of the cavities under stronger probe powers, where the intrinsic nonlinearity of the SQUID becomes significant. By fitting the nonlinear model for the scattering parameter, introduced in Section 2.6.2, to the obtained data, we determine the Kerr constant for each cavity at various magnetic flux bias points. Finally, we compare these results to the theoretical predictions presented in Section 2.3.4.

3.1 Experimental setup

Operation of the SQUID cavities requires cooling below the superconducting transition temperature of 9.25 K for Nb [85]. To ensure that the cavities with microwave frequencies of around 8 GHz are not thermally excited ($k_B T \ll \hbar\omega_c$), even lower temperatures (<1 K) are required.

3.1.1 Dilution refrigerator

To reach such low temperatures, the waveguide with the cavities is mounted on the baseplate of a *Oxford Triton 400* dilution refrigerator, as seen in Fig. 3.1 a). The gold plated copper plates have decreasing temperatures from top to bottom. Cooling power is provided by two systems. The first system, a pulse tube (PT) cooler, cools the first stage to 50 K and the second stage to about 4 K by adiabatic expansion of compressed He. For further cooling, a second circuit containing a mix of ^{3}He and ^{4}He is employed. This circuit is connected to the PT via a heat exchanger, which condenses the He mix. After evaporative cooling to about 800 mK, the mix separates into a dilute (^{3}He and ^{4}He) and a concentrated (^{3}He) phase. The movement of ^{3}He from the concentrated to the dilute phase upon continuously pumping on the latter cools to a baseplate temperature of 30 mK. The pumped out ^{3}He is returned through the condense line, and the cycle continues. [86, 87]

3.1.2 Microwave and DC wiring

Fig. 3.1 b) shows the wiring setup. To protect the cavities from room temperature thermal noise, the microwave signal of a vector network analyser (VNA) is attenuated at the 4 K and 30 mK stage. The signal is filtered using a *K&L 6L250* 12 GHz lowpass filter and a homebuilt Eccosorb filter before reaching the waveguide (WG). On the WG output, *Quinstar* cryogenic isolators prevent thermal noise from entering the WG through the output and block any possible reflected signals from returning to the WG. Superconducting Nb output lines (purple) bring the

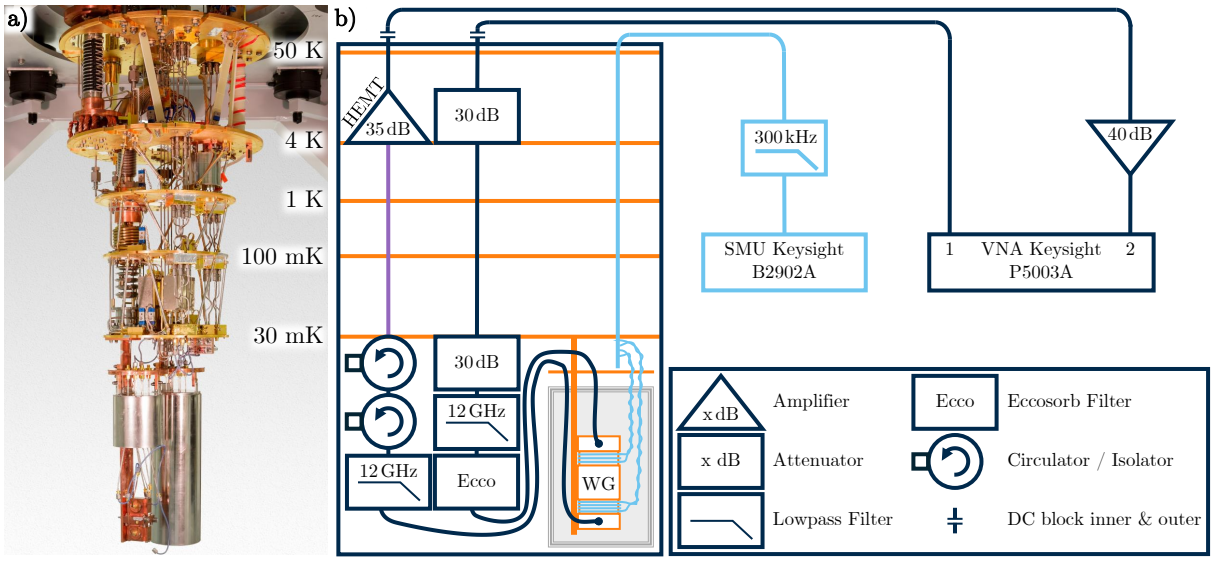

Fig. 3.1 **a)** Oxford dilution refrigerator with µ-metal/Nb/µ-metal cans for magnetic shielding, mounted on the 30 mK baseplate. The magnetic shield has been removed from the can on the left, revealing the copper T-beam to which a waveguide (WG) is mounted. Picture taken by D. Jordan. **b)** Illustration of the wiring used, discussed in the main text.

weak output signal to a high electron mobility transistor (HEMT) amplifier with a nominal noise temperature of about 2 to 4 K. An additional amplifier at room temperature boosts the signal to levels suitable for the VNA input.

The DC wiring for magnetic field tuning is routed to the baseplate using pre-installed looms that are thermally anchored at each stage. Current is supplied by a source measure unit (SMU). Pairwise twisting of the wires connecting the loom with the setup and filters with a cut-off at 300 kHz right before the DC-lines enter the fridge reduces magnetic field noise.

3.1.3 Waveguide with tunable coupling

In Fig. 3.2, one of the two waveguides used within this thesis is shown. As discussed in Section 2.4, the coupling between the U-shaped cavity and the fundamental propagating waveguide mode is expected to increase with increasing distance from the waveguide centre. To allow for different couplings, an existing waveguide design has been adapted. Using a Vernier scale engraved on the WG, the clamps which hold the silicon chips can be precisely positioned within an elongated slit in the wall of the WG.

To tune the microwave cavities with a magnetic field, two coils with about 60 and 100 turns are wound around the waveguide. The coils are made from *Supercon Inc. 54S43* ∅ 0.1 mm copper wire, which contains superconducting niobium filaments. This is essential at mK temperatures, where even a few µW of dissipation can significantly heat the experiment. For example, we observed that using normal resistive, gold-coated *Molex SL* connectors close to the waveguide (inside the magnetic shield) already leads to heating by several mK at coil currents of a few mA.

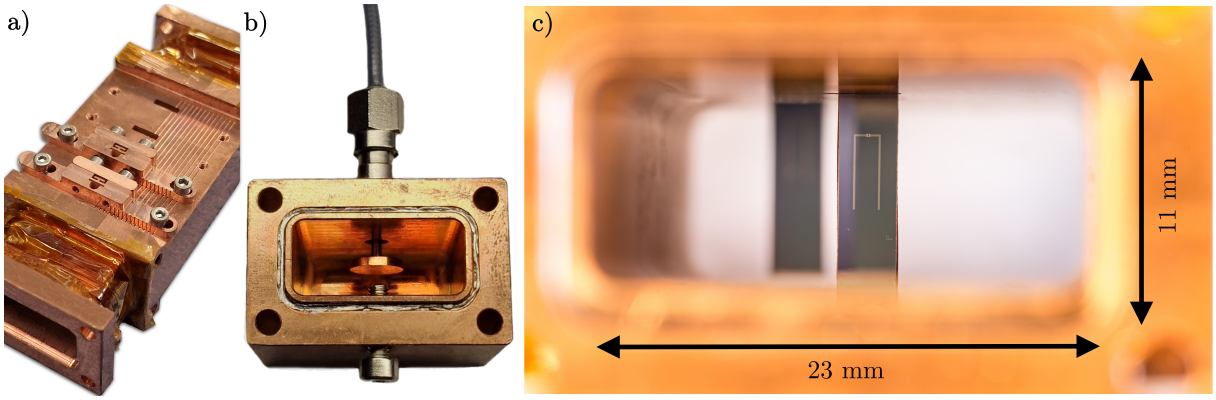

Fig. 3.2 **a)** Waveguide with tunable coupling for up to four cavities. Using the Vernier scale engraved on the waveguide and the clamps, the chip position can be adjusted. On both ends, coils for the application of magnetic bias fields are wound around the waveguide. **b)** Coaxial to waveguide adapter, connecting the waveguide to SMA microwave cables. **c)** View into the waveguide with two cavities, placed at different distances from the centre. Picture taken by D. Jordan.

3.1.4 Frequency tunable cavities - Design and fabrication process

All frequency tunable cavities characterised in this thesis were fabricated on the same silicon wafer by *STAR Cryoelectronics* (StarCryo). The design closely follows that of a previous batch used by D. Zöpfl, et al. [6, 7, 9, 50]. For the new batch, the SQUID loop size was modified to 35

x 35 µm, and the leg length was slightly reduced to $l = 3.1$ mm for samples labeled *WSQx* and $l = 3.3$ mm for *WSQLx*. Additionally, a silicon wafer with higher resistivity was used. Apart from these changes, the new samples are identical to those from the previous batch.

In Fig. 3.3, an optical microscope image with zoom-ins on the SQUID loop can be seen. The fabrication process is described in Ref. [50] and starts with deposition of a Nb/Al-AlOx/Nb trilayer with a total thickness of about 270 nm, of which 9 nm is aluminium (Al). After that, a resist mask defines the junctions and the top Nb/Al-AlOx layer is removed everywhere except the junctions. Then the bottom cavity leg is defined from the remaining Nb layer. Subsequently, an insulating layer of 300 nm SiO_2 is deposited. To connect to the bottom layer, vias are etched through this layer at the position of the junctions, visible as small round dots in Fig. 3.3 a). As mentioned in Section 2.5, the SiO_2 layer can introduce dielectric loss and is therefore removed everywhere except from the SQUID area. This is especially important in areas of high electric field, like at the end of the cavity legs [50]. Areas with remaining SiO_2 appear purple in Fig. 3.3. Finally, another layer of 300 nm Nb is deposited, which is used to form the top leg.

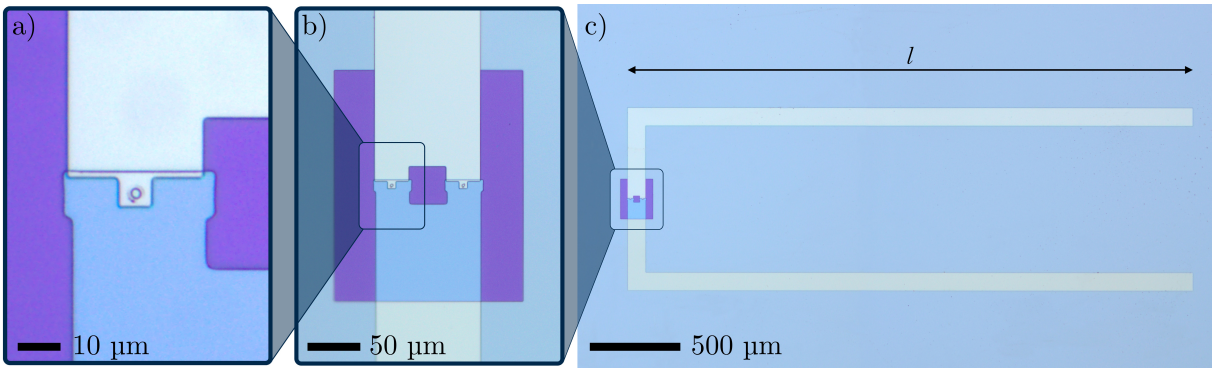

Fig. 3.3 Optical microscope image of a Startcryo microstrip cavity with zoom-ins on **b)** the SQUID loop and **a)** one of the junctions. The background, which appears light blue, corresponds to the Si wafer, with the U-shaped Nb cavity legs appearing white. The purple layer corresponds to SiO_2, which acts as an insulating layer between the bottom and top leg, only connected via the junctions.

3.2 Quality factors

To obtain the quality factors of the microwave cavities, the S_{21} scattering parameter is measured using the VNA. The VNA generates a probe tone whose phase and amplitude change when travelling through the waveguide and interacting with the cavity. By comparing the transmitted signal to the original probe tone, the VNA extracts the complex scattering parameter S_{21} from the relative change in amplitude and phase.

As the phase and amplitude of the probe tone are not only changed by the cavity itself but also by other components, such as microwave cables, attenuators and amplifiers, a background is superposed on the cavity response. The model given in Eq. (2.83) accounts for that with an additional prefactor, which approximates the amplitude of the background with a constant a and the phase with a linear function $\alpha - \omega_p \tau$. In practice, better results can be achieved by adding an additional slope to the amplitude of the background. This model only works well if the background behaves linearly within the frequency range of the resonance linewidth. For cavities

that can be tuned over several linewidths, approximating the background is not necessary, as the actual background can be obtained by tuning the cavity out of the measured frequency range.

In Fig. 3.4 a) the raw, low power scattering data for one of the characterised cavities can be seen. Close to resonance, the interaction of the microwave signal with the cavity leads to a phase shift and a visible dip in the magnitude of the signal transmitted through the waveguide. After subtracting the background, the scattering data resembles a circle on the complex plane, as can be seen in Fig. 3.4 b). Using Eq. (2.83), this circle can be fitted to obtain the loaded quality factor Q_l and the complex coupling quality factor Q_c. The background corrected scattering data reveals that the resonance is asymmetric and the resonant point does not lie on the real axis, but is rotated by an angle φ around the off-resonant point. This is the result of an impedance mismatch between the cavity and the waveguide mode [45], and is taken into account when calculating the internal quality factor with Eq. (2.84).

As illustrated in Fig. 3.4 c), a transformation that removes the impedance mismatch can be applied to the scattering data. As demonstrated in Ref. [45], this transformation requires not only rotating the circle but also scaling its diameter by a factor of $1/\cos(\varphi)$. This transformation is particularly useful for nonlinear cavities, as it allows for differentiation between asymmetry caused by impedance mismatch and asymmetry resulting from nonlinearity.

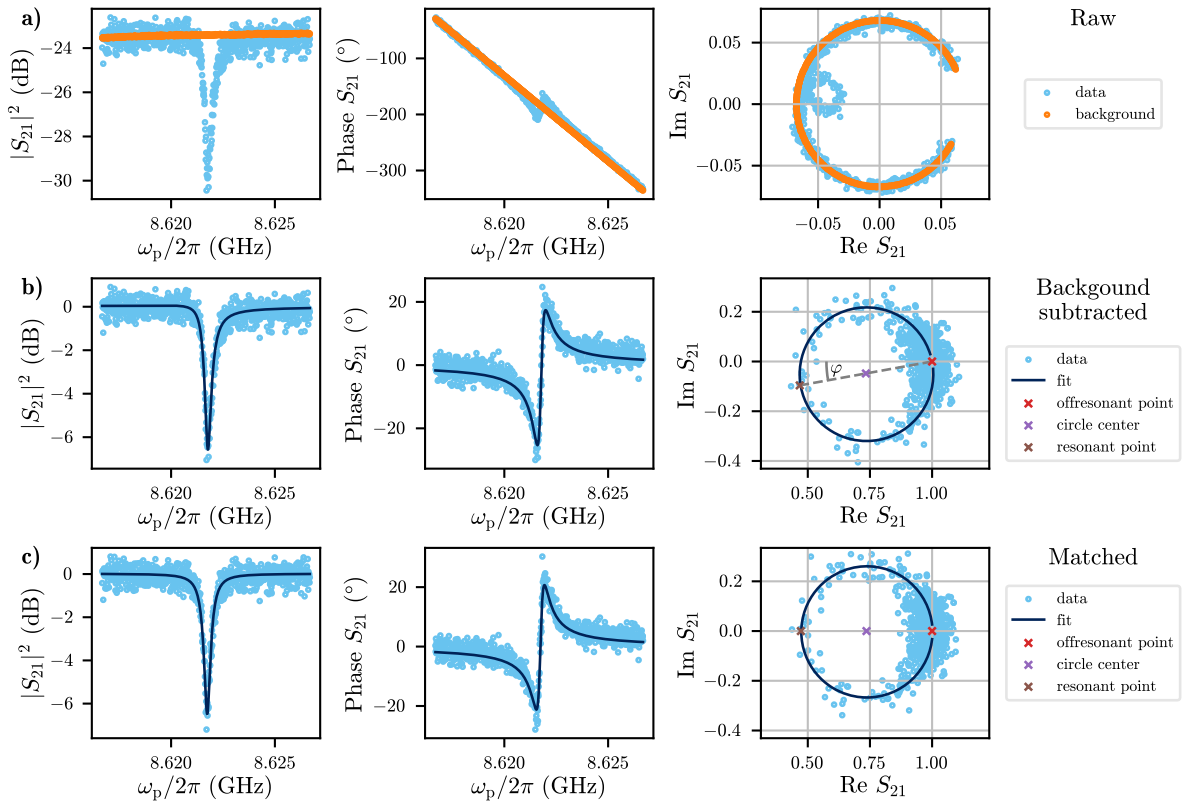

Fig. 3.4 **a)** Measured raw scattering data for cavity *WSQL8*, at the flux sweet spot $\phi_\mathrm{loop} \approx 0$. The background was obtained by tuning the cavity so its resonance frequency fell well outside the measurement window. Data for the background is less noisy, as it was measured with a higher probe tone power. **b)** Background subtracted data with circle fit. **c)** Data after applying a transformation which removes the impedance mismatch [45].

3.2.1 External quality factors - Coupling for different sample positions

To investigate the tunability of the coupling between the cavities and the propagating waveguide mode, discussed in Section 2.4 and 3.1.3, several cavities have been placed at different positions within the waveguide over multiple cooldowns.

The engraved vernier scale on the waveguide enables precise placement of the clamp, with a nominal resolution of 0.1 mm. However, the groove in which the chip sits within the clamp has some clearance. This clearance is required to ensure the chip remains intact during thermal contraction, but also allows for slight offsets and tilts of the chip within the clamp. Consequently, we estimate the overall positioning precision to be approximately 0.2 mm.

Using the linear circle fit routine on measured scattering data, the effective coupling quality factors, defined in Eq. (2.84), and the impedance mismatch have been obtained. The resulting values are plotted in Fig. 3.5. The blue line corresponds to a fit with the expected $\propto 1/\sin(\pi d/w_{\mathrm{WG}})$ behaviour given by Eq. (2.80). The closer the cavities are placed to the center of the waveguide, the smaller the coupling ($\kappa_{\mathrm{c}} \propto 1/Q_{\mathrm{c,eff}}$). As can be seen, the obtained data follows the expected trend reasonably well and mounting a cantilever chip does not seem to influence the coupling.

The obtained values for the impedance mismatch do not show any specific trend with the individual sample position. Significantly larger values of up to $\varphi \gtrsim 50\,^\circ$ have been observed in a different waveguide, when two samples were placed close to each other in the same clamp. Simulations by R. Sathyanarayanan show that the dielectric Si substrate of a nearby chip alters the shape of the waveguide mode. This leads us to suspect that the comparably small variations of the impedance mismatch in the waveguide with tunable coupling might be related to the relative position of the individual samples in the waveguide. However, more data would be necessary to confirm this hypothesis.

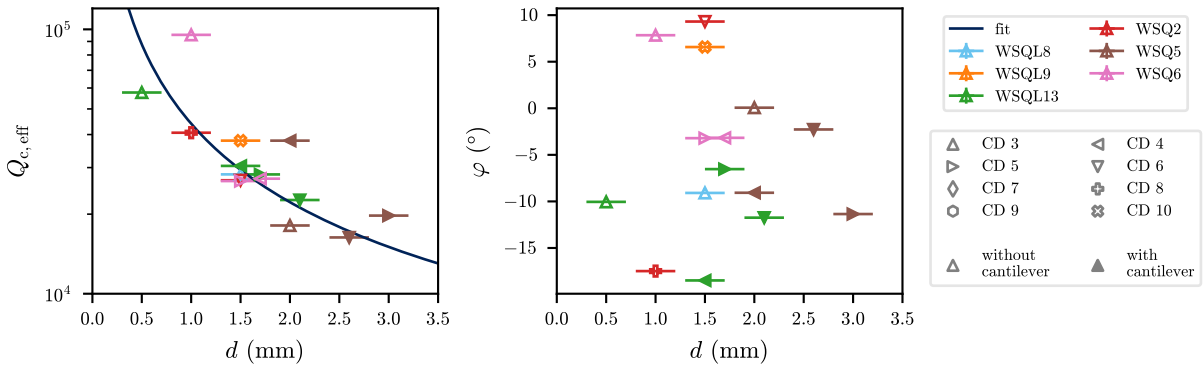

Fig. 3.5 Effective coupling quality factor $Q_{\mathrm{c,eff}}$ and impedance mismatch φ of five tunable cavities at different distances d from the waveguide center. For data points with filled markers, an AFM cantilever chip with a magnetic particle on its tip was mounted over the SQUID loop. Different markers correspond to different cooldowns (CD). The blue line shows a fit with Eq. (2.80). The uncertainty of 0.2 mm corresponds to the estimated accuracy of positioning the chip within the waveguide. Uncertainties of fit parameters are smaller than the marker size.

3.2.2 Internal quality factors

In Figure 3.6, the internal quality factors of seven tunable cavities are plotted.

A recently published paper by D. Rieger [88] demonstrated that measurements of internal quality factors can be affected by Fano interference between the signal and a background path. For example, in measurement setups that operate in reflection using a circulator, limited isolation between ports can allow parts of the incoming signal to bypass the device under test. This bypassed signal interferes with the actual measured signal, leading to a systematic error in the obtained internal quality factor. This error tends to increase with the coupling ratio $Q_\mathrm{i}/Q_\mathrm{c,eff}$.

In the case of our waveguide setup, a possible background path could arise from microwave signals bypassing the waveguide entirely or from standing waves within the setup. To investigate whether the measurement of quality factors in our waveguide setup is affected by Fano interference, the same cavities were measured at different couplings over multiple cooldowns. As can be seen from the plot, the obtained quality factors for the individual cavities do not significantly change with the coupling ratio. Obtained quality factors in the overcoupled regime $Q_\mathrm{i}/Q_\mathrm{c,eff} > 1$ are to a large extent consistent with values obtained in the undercoupled regime $Q_\mathrm{i}/Q_\mathrm{c,eff} < 1$, where the systematic error due to Fano interference should be negligible compared to stochastic errors. This allows us to conclude that, within the tested coupling regime, the background path in our setup is sufficiently small, such that the measured quality factors remain unaffected by Fano interference.

With internal quality factors between $15 \cdot 10^3$ and $35 \cdot 10^3$, the cavities of the new batch exhibit less internal loss than the cavities of the previous batch, which only reached internal quality factors of about $7 \cdot 10^3$ [50]. Since the use of a higher-resistivity Si wafer is the only relevant difference in design and fabrication (see Section 3.1.4), we attribute this improvement to an improved quality factor of the substrate.

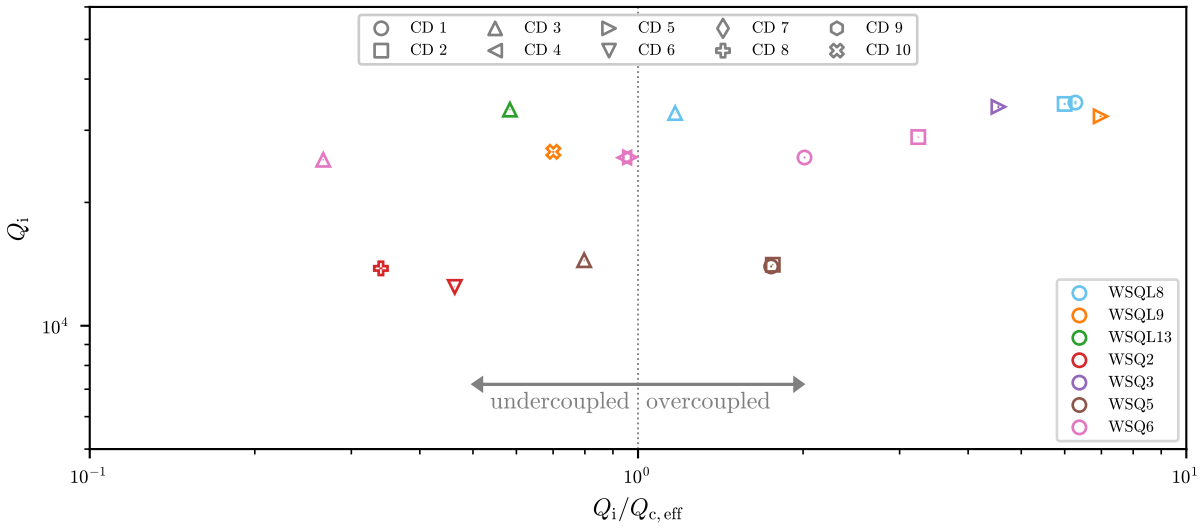

Fig. 3.6 Internal quality factors Q_i at the flux sweet spot $\Phi_\mathrm{loop} \approx 0$ of seven tunable cavities, measured over different cooldowns at different coupling ratios $Q_\mathrm{i}/Q_\mathrm{c,eff}$. Uncertainties of fit parameters are smaller than the marker size. Data on internal quality factors after mounting of cantilevers can be found in Section 5.2.3.

Despite this improvement, much higher quality factors in the order of 10^6 have already been observed in a similar waveguide setup for fixed frequency Nb cavities without a SQUID [52]. First measurements by B. Thyagarajan and R. Sathyanarayanan on recently started in-house fabrication of tunable Nb cavities with Manhattan style Al junctions, yielded quality factors of more than 10^5. With the Manhattan technique, junctions can be fabricated without deposition of an additional insulating layer [89]. As the cavities with these junctions show significantly higher quality factors, we believe that a major limitation on the quality factor for the latest batch of StarCryo cavities is the residual SiO_2 layer.

Nevertheless, with mechanical frequencies between 200 kHz and 450 kHz and cavity quality factors of up to $35 \cdot 10^3$, corresponding to linewidths of approximately 250 kHz, the samples from the new batch would already bring us close to reaching the sideband resolved regime. However, as discussed later in Section 5.2.3, we have yet to maintain these quality factors after mounting a cantilever with a magnetic particle.

3.3 Frequency tuning behaviour

After characterising the quality factors at the flux sweet spot $\Phi_{\text{loop}} = 0$, we want to investigate the frequency tuning behaviour with externally applied magnetic flux Φ_{ext}. Therefore, we measure the S_{21} scattering parameter for varying currents I_{coil} applied through one of the coils wound around the waveguide.

In Fig. 3.7, an example measurement result is shown. We see two resonances that correspond to two different cavities in the waveguide. With changing coil current, the cavity frequency periodically changes. As described in Section 2.3.2.1, the geometric SQUID loop inductance leads to shielding of the externally applied flux. This leads to discrete frequency jumps between multiple solutions for the loop flux. Furthermore, a hysteretic tuning behaviour with the sweep direction of the externally applied magnetic flux can be observed.

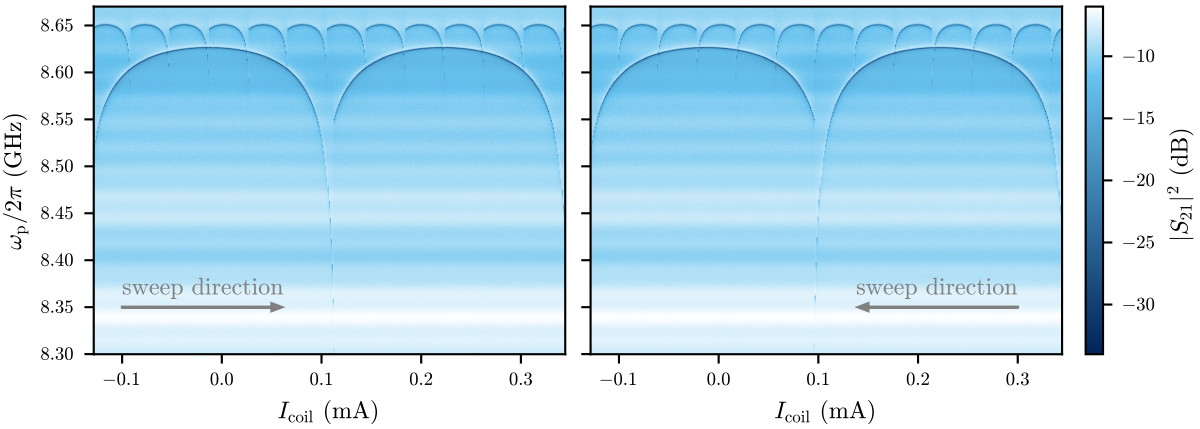

Fig. 3.7 Measured S_{21} scattering data for the cavities *WSQL8* and *WSQL13* at different coil currents. Due to a smaller distance to the coil used, we identify the resonance with a smaller tuning period as *WSQL13*. For the left (right) plot, I_{coil} was swept upward (downward).

Measurements on seven cavities yield the tuning behaviours shown in Fig. 3.8 a). At each coil current, the cavity frequency ω_c was obtained from $\min(|S_{21}|)$. The outer, smaller subplots show the tuning behaviour of the individual cavities, while the bigger central plot allows for direct comparison of all samples. Note that the plot only shows datapoints for the hysteretic branch that corresponds to an increasing sweep of the coil current.

As discussed in Section 3.1.4, all cavities were fabricated on the same wafer. The designs of the two cavity types (*WSQx* and *WSQLx*) only differ by a slight difference in microstrip length. Nevertheless, significant differences in the tuning behaviour can be observed. For example, *WSQL13* shows a maximum tunability of only 50 MHz, while *WSQL9* tunes by more than 300 MHz. Also, the overlap of the hysteretic tuning lobes around $\Phi_{ext} = \pm 0.5\,\Phi_0$ varies between samples. This indicates different SQUID shielding parameters β_L, as shown in Fig. 2.8 c) in Chapter 2.

To obtain quantitative values for β_L, the participation ratio β_r and the sweet spot frequency $\omega_c(\phi_{loop} = 0)$, the tuning behaviours are fitted with Eq. (2.59). Assuming a linear relation between coil current and the generated magnetic field at the SQUID loop, the fit uses the periodicity of the individual tuning curves to determine the external magnetic flux in units of the magnetic flux quantum. Possible solutions for the loop flux are then determined from the external flux by solving Eq. (2.54). The resulting fit parameters can be found in Fig. 3.8 b).

As expected from the initial qualitative comparison, the obtained parameters show a considerable spread. In particular, the lower frequency samples vary by more than a factor of six in β_r.

One might suspect that environmental factors, such as the relative position of the samples within the waveguide, could influence the obtained parameters. Indeed, small shifts in the sweet spot frequency are observed between cooldowns with different (relative) positions of samples in the waveguide. This is most likely due to variations in the linear capacitance, which can arise from differences in the capacitance to the waveguide wall or from the dielectric of nearby samples. However, the magnitude of these shifts in sweetspot frequency is typically below 5 MHz, which is too small to account for the substantial variation seen across different samples.

Assuming a constant geometric loop inductance, a higher SQUID participation ratio should correspond to a lower shielding parameter β_L, as a large junction inductance would dominate over the loop inductance. However, no clear anti-correlation between β_r and β_L is observed. This suggests that not only do the junction parameters vary, but also the linear loop inductance. Possible sources include lithographic variations in the SQUID loop geometry or differences in the vias connecting the top and bottom legs across the junctions. In fact, some samples show fine cracks in the Nb film near the vias, but whether these influence the loop inductance is unclear.

Another potentially relevant factor is the junction capacitance. Simulations shown in Fig. 2.9 demonstrate that including a finite junction capacitance affects the tuning behaviour. Increasing the junction capacitance reduces the effective shielding and increases the apparent β_r. Since the model used for fitting does not account for this, the fit might overestimate the SQUID participation ratio, especially for samples that already exhibit intrinsically high participation ratios.

In microfabrication, on-wafer variation in sample parameters is often correlated with position. For example, samples near the wafer centre may differ from those closer to the edge [90]. However, a comparison between the extracted parameters and the physical locations of the samples revealed no clear spatial correlation.

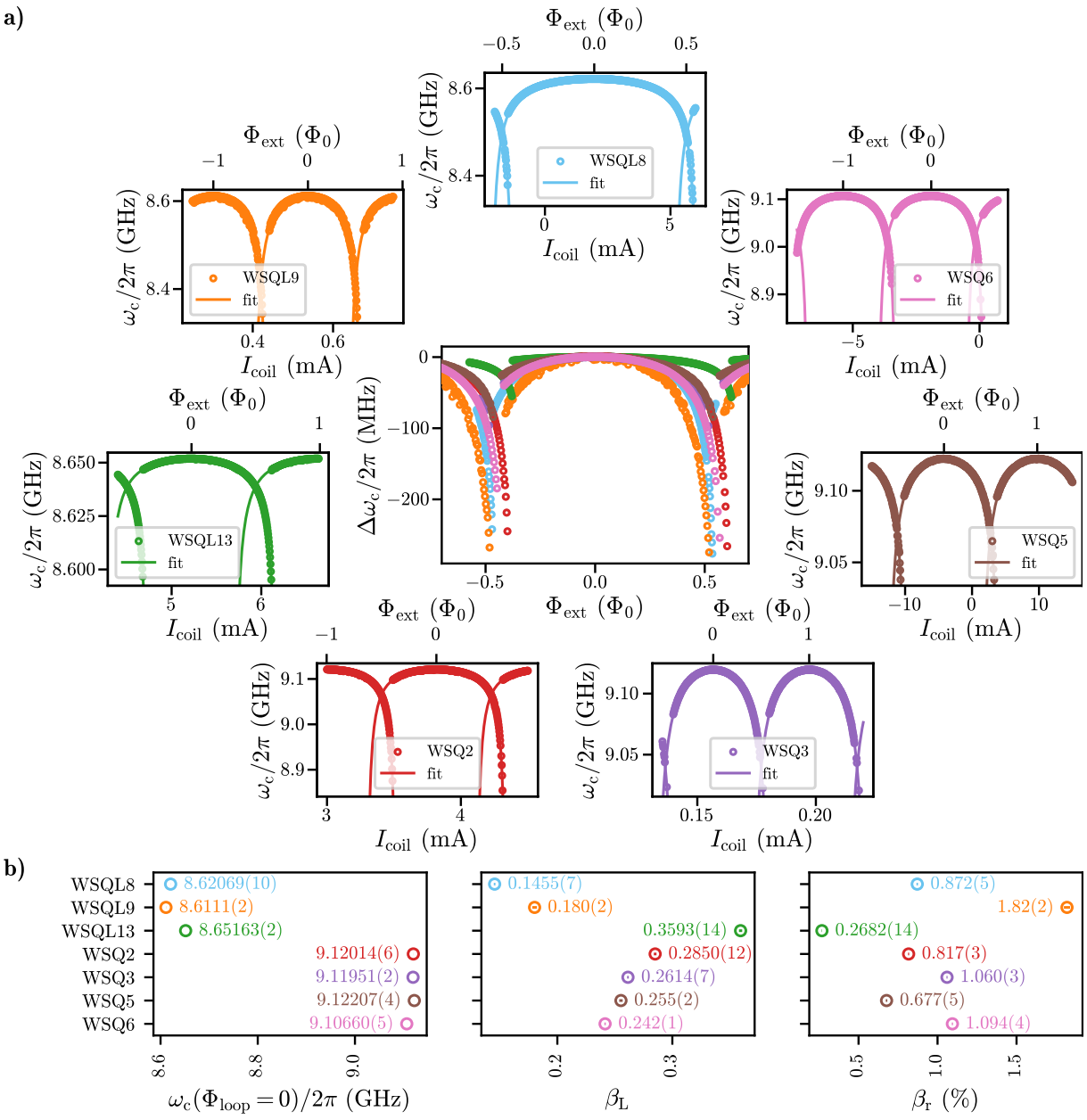

Fig. 3.8 **a)** Frequency tuning behaviour with externally applied bias field for seven cavities. Small plots show the cavity resonance frequency at varying currents applied to one of the tuning coils. Solid lines correspond to fits with Eq. (2.59). The external flux obtained from the periodicity of the tuning behaviour is shown on the top axis. The bigger central plot allows for direct comparison of the seven cavities. **b)** Cavity sweet spot frequency $\omega_c(\phi_{\mathrm{loop}} = 0)$, SQUID participation ration β_r and shielding parameter β_L corresponding to the fits shown in **a)**.

3.3.1 Internal quality factors for different flux bias points

When detuning the cavities from the flux sweet spot, the sensitivity to changes in external flux increases $\propto \partial\omega_c/\partial\Phi_{ext}$. While this is the key feature for detecting tiny variations of magnetic fields, this also leads to increased sensitivity to noise.

Fig. 3.10 shows the internal quality factors of the seven cavities at varying values of slope $\partial\omega_c/\partial\Phi_{ext}$. With increasing slope, the obtained internal quality factors tend to decrease. This decrease might be explained by an apparent broadening of the cavity linewidth due to resonance frequency fluctuations [91]. If the timescale of fluctuations is faster than the VNA measurement, the measured resonance corresponds to an average of resonances with different frequencies. As illustrated in Fig. 3.9, this averaged resonance has a broadened linewidth.

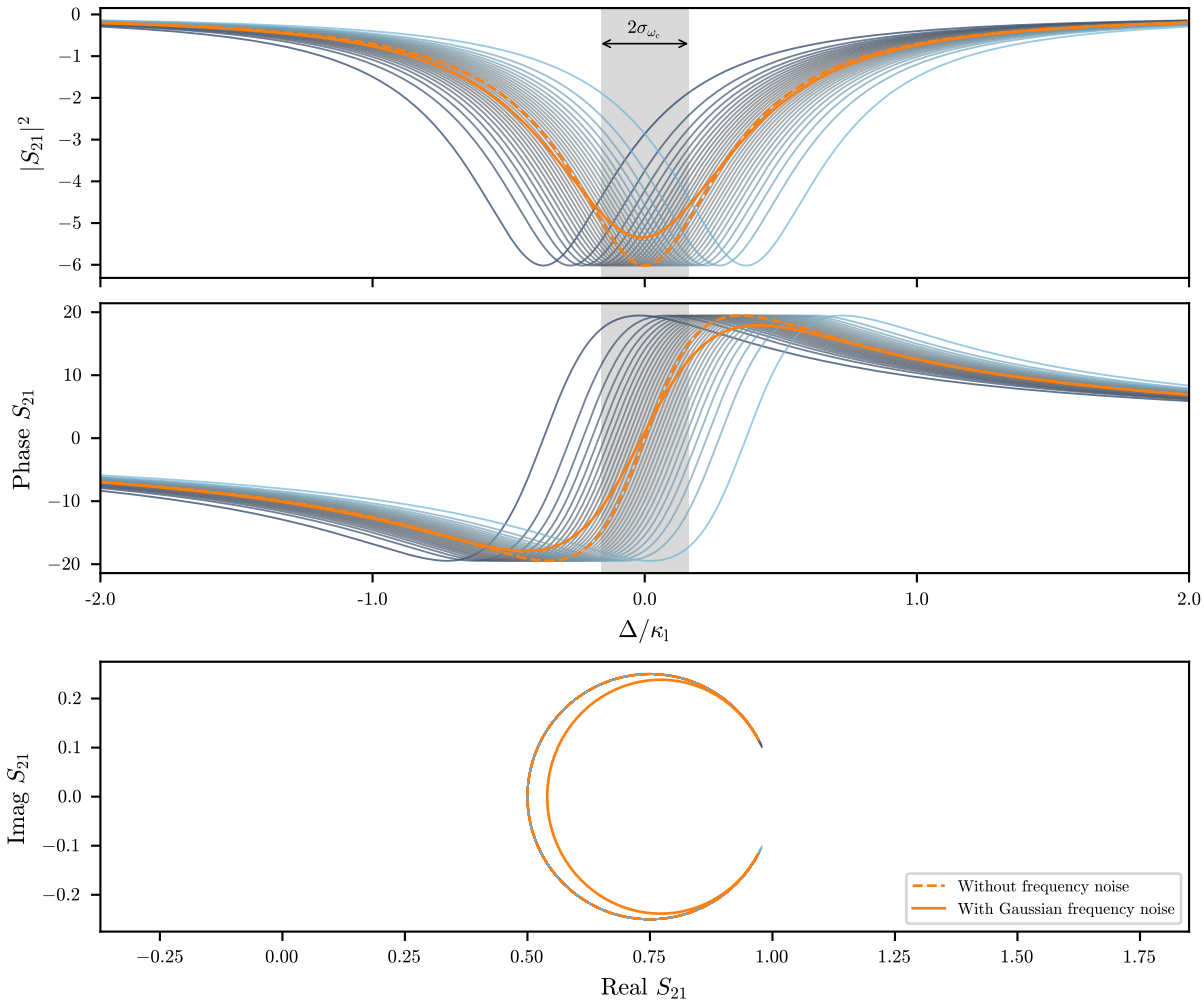

Fig. 3.9 Effect of Gaussian cavity frequency fluctuations on the measured cavity response. Blue lines show individual cavity responses with resonance frequencies sampled uniformly from a Gaussian distribution with standard deviation σ_{ω_c}, centred at ω_c. The dashed orange line represents the response of a cavity with a fixed resonance frequency, while the solid orange line shows the averaged response in the presence of Gaussian frequency fluctuations.

One possible origin for frequency noise is fluctuations in the external magnetic field in the lab. Although the setup is already well shielded with a µ-metal/Nb/µ-metal can, residual magnetic field noise can still contribute to frequency fluctuations. Another source of frequency noise may stem from fluctuations in the current through the tuning coils. Insufficient filtering could allow high-frequency noise components to couple into the system, thereby affecting the magnetic flux and, consequently, the cavity frequency. One possible mitigation strategy would be to add additional (cryogenic) low-pass filters. Implementation of a persistent current setup could even completely eliminate current noise.

A detailed analysis of the impact of frequency noise on internal cavity quality factor measurements was carried out in Ref. [91]. In this work, the authors derive a model that assumes Gaussian fluctuations of the cavity frequency. By fitting this model to scattering data, the standard deviation σ_{ω_c} of the frequency fluctuations can be extracted. Applying this Gaussian noise model to a dataset of four cavities measured within a single cooldown revealed increasing noise levels for samples positioned closer to the tuning coil. However, for the data presented here, we do not perform a quantitative analysis. A direct comparison of noise levels between individual cavities is challenging due to variations in the coils used for different cooldowns, as occasional coil failures necessitated replacements.

Apart from the apparent decrease in internal quality factor due to frequency fluctuations, tuning the cavity can lead to hybridisation with another mode. This introduces an additional loss channel and reduces the internal quality factor. For cavity *WSQ5*, the drop and subsequent increase in quality factor coincide with a crossing with another cavity in the waveguide, suggesting that the behaviour may be due to coupling with this mode. In contrast, cavity *WSQL9* does not cross another cavity, but may have hybridised with a fixed-frequency cavity located near its flux sweet spot. For the shown linear fits, we therefore exclude these points.

Interestingly, we observe that the quality factor decreases roughly linearly with the slope of the cavity tuning behaviour. In the case of Gaussian frequency noise, one would instead expect the cavity linewidth to increase linearly [91], leading to an internal quality factor that scales as $1/(\partial\omega_c/\partial\Phi_{ext})$. Therefore, the observed linear decrease in Q_i suggests a deviation from this simple model, possibly indicating non-Gaussian noise statistics or the presence of other mechanisms which broaden the linewidth.

The decrease in internal quality factor could also be attributed to an actual increase in internal loss. Tuning the cavity changes the mode structure and might increase the effective participation ratio of lossy elements, like the residual insulating SiO_2 layer or the junction oxide barrier.

A steeper decrease in Qi for samples with higher SQUID participation ratios might point toward such loss mechanisms. However, the absence of a clear correlation between the internal quality factors at the flux sweet spot (where first-order sensitivity to flux noise vanishes) and the obtained SQUID participation ratios of the individual samples (see Fig. 3.8) suggests that junction losses alone may not account for the observed behaviour.

To clearly distinguish between an actual increase in internal loss and an apparent increase due to cavity frequency fluctuations, further investigations are required. One approach would be to perform measurements with faster frequency sweeps. If frequency fluctuations occur

predominantly at low frequencies, a faster sweep should result in narrower observed linewidths. Alternatively, ringdown measurements could give direct insight into the actual energy decay rate.

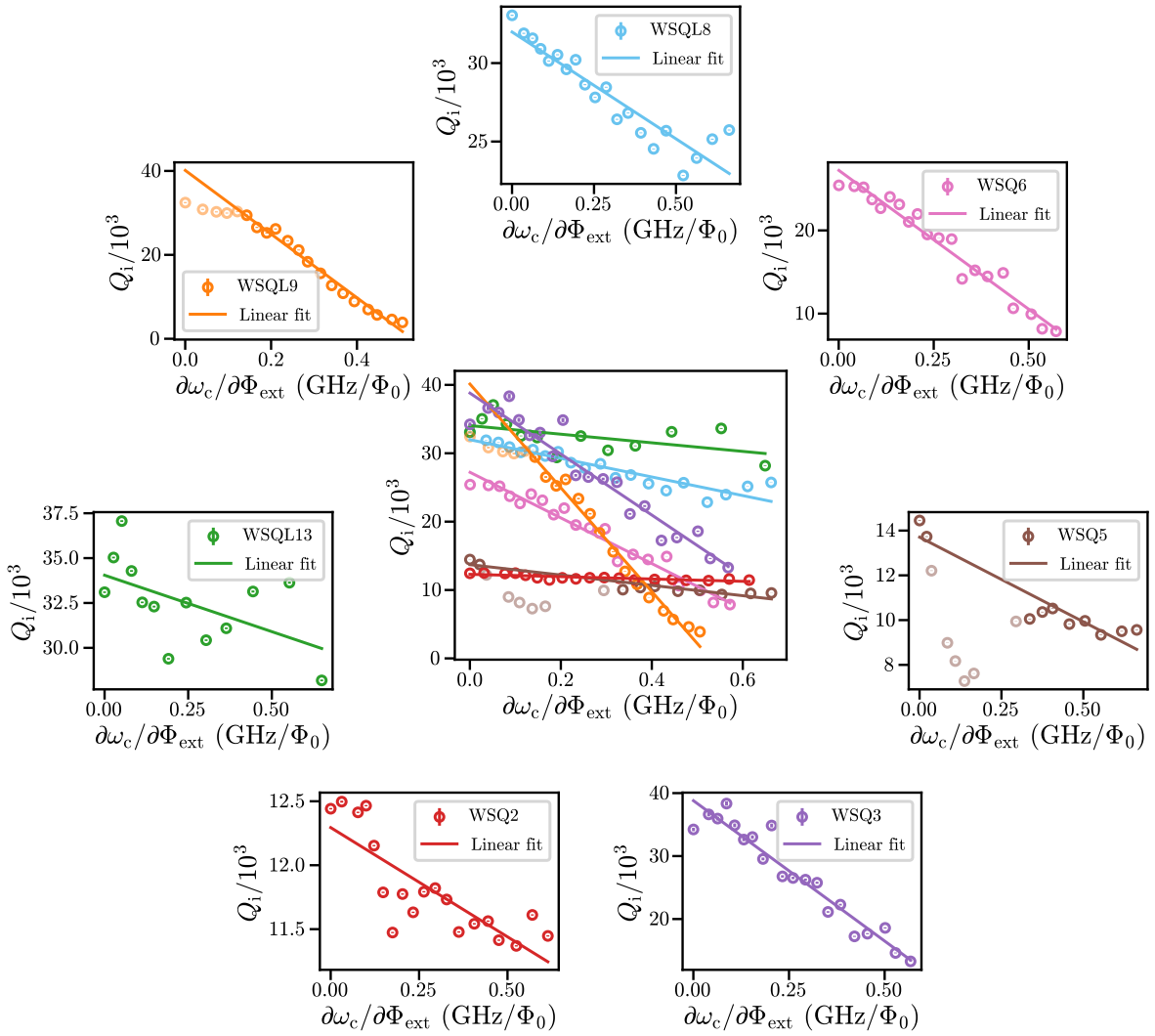

Fig. 3.10 Internal quality factors for seven cavities at varying flux sensitivities. With increasing slope $\partial\omega_c/\partial\Phi_{ext}$, the sensitivity for flux noise increases, which leads to an apparent decrease of Q_i. For cavity *WSQ5*, coupling to a different cavity might explain the sudden drop and subsequent increase in Q_i.

3.4 Kerr nonlinearity - Nonlinear circle fit routine

Up to this section, all measurements were done with low probe power, with less than 30 photons circulating in the cavity. At these low powers, the bias current over the SQUID is small, and the intrinsic nonlinearity of the SQUID inductance is negligible. If the pump power is increased, nonlinear effects start to appear.

In Fig. 3.11, the cavity response is plotted for different input powers. The individual suplots correspond to different sweep directions of the probe tone frequency, indicated by the visible arrows.

With increasing input power, the cavity frequency starts to shift, and the resonance gets asymmetric. Above a certain input power (the critical input power $P_{\mathrm{in,bi}}$), the cavity response depends on the sweep direction of the probe tone. As discussed in Section 2.6.2, this change in scattering parameter can be described by considering the Kerr nonlinearity of the SQUID cavity.

To determine the Kerr constant, data with increasing input power can be fitted using an adapted nonlinear circle fit routine, which uses Eq. (2.89) to model the nonlinear cavity response. Starting with a linear circle fit of a low power trace, as shown in Fig. 3.12 a), the linear cavity frequency without Kerr shift $\omega_{\mathrm{c}}(\bar{n}_{\mathrm{c}} \approx 0)$ can be obtained. Using this frequency, iteratively fitting the nonlinear model to traces with increasing input powers, yields values for Kerr.

As shown in Fig. 3.12 b), the nonlinear model precisely describes the cavity response at powers close to the critical input power. The photon number dependent frequency shift, as well as the shape of the cavity response, is well captured by the model. Above the critical input power, shown in Fig. 3.12 c), using both solutions for the intracity photon number allows fitting the obtained scattering data for the low and high photon number branches. At this power level, the measured data begins to slightly deviate from the fit curve. The earlier-than-expected jump in the cavity response might be explained by flux noise. Furthermore, at such high photon numbers, higher-order nonlinearities that are not included in the model may start to play a significant role.

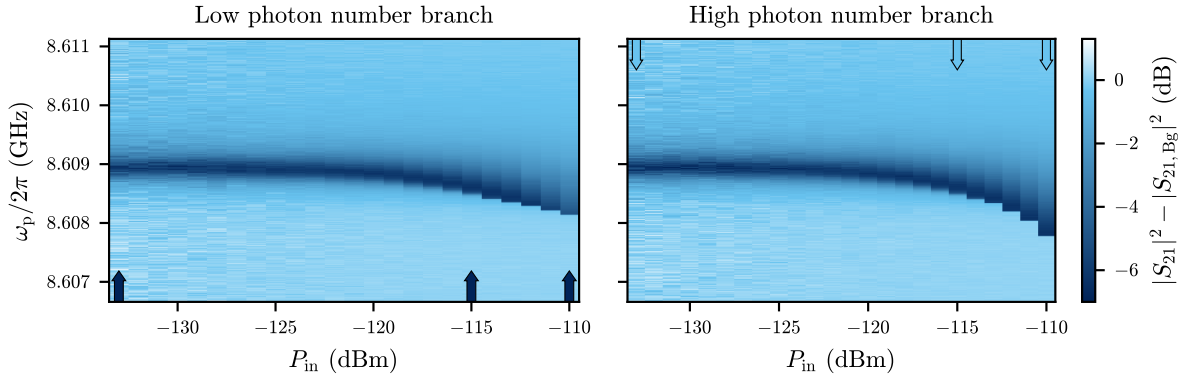

Fig. 3.11 Response of cavity *WSQL8* at different power tone powers, measured at $\Phi_{\mathrm{loop}} \approx 0.23\,\Phi_0$, $\Delta\omega_{\mathrm{c}} \approx 12\,\mathrm{MHz}$ detuned from the sweet spot. Arrows indicate the sweep direction of the probe tone frequency. Fits to slices marked with arrows can be seen in Fig. 3.12.

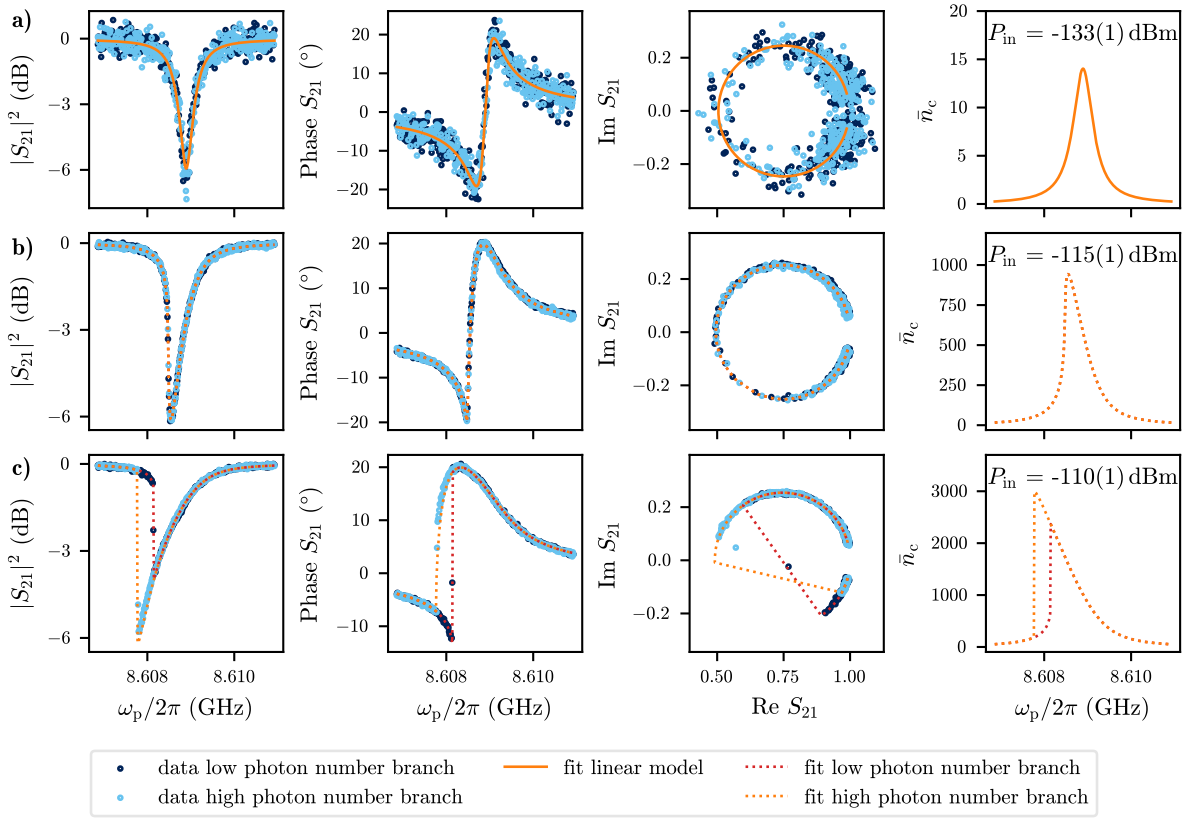

Fig. 3.12 **a)** Linear circle fit for low power scattering data. The mean cavity photon number $\bar{n}_c$ does not exceed 15, and the frequency shift $\mathcal{K}\bar{n}_c$ is too small to observe nonlinear effects. **b)** Nonlinear circle fit for intermediate power scattering data. A frequency shift can be observed, and the resonance shows the typical asymmetric shape of a shark fin. As the critical input power is not yet exceeded, data and fits for the high and low photon number branches are identical. **c)** Nonlinear circle fit for high power scattering data. Here, the critical input power is exceeded, and two possible solutions for the photon number exist.

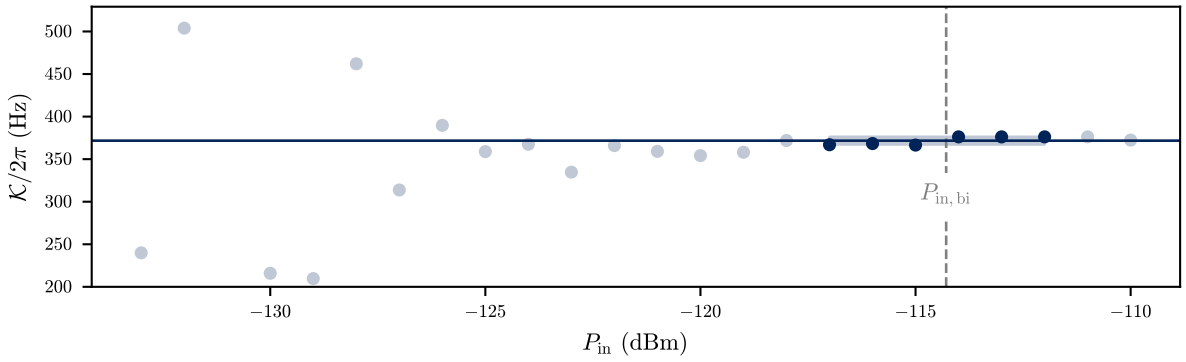

Fig. 3.13 Kerr obtained from the nonlinear circle fit converges with increasing input power. The horizontal blue line and the shaded region show the mean value and standard deviation of Kerr in the range of ±3 dBm of the bistable input power.

For powers well below the critical input power $P_{\mathrm{in,bi}}$ the fit routine does not give meaningful values for Kerr. For small photon numbers, the frequency shift $\mathcal{K}\bar{n}_{\mathrm{c}}$ is much smaller than the cavity linewidth and can not be resolved. As shown in Fig. 3.13, Kerr converges with increasing power.

Accurately determining the microwave power P_{in} at the cavity is essential to obtain precise values for Kerr. This requires knowledge of the cryostat input attenuation. For the data in this thesis, the input attenuation was measured at room temperature. Due to the use of stainless steel coaxial input lines, only a small change is expected after cooling down [92]. However, to account for thermal variations and ripples in the attenuation profile, we assume an uncertainty of $\pm 1\,\mathrm{dB}$.

A more accurate method to determine the input attenuation in the cold state would involve characterising the output chain using a thermal noise source, such as the Johnson–Nyquist noise of a $50\,\Omega$ terminator [60]. Measuring the total transmission in the cold state would then allow for direct extraction of input attenuation. However, this approach requires a cryogenic microwave switch to alternate between the noise source and the measurement chain, which is not available in the current setup.

As shown in Fig. 3.14, using the nonlinear circle fit routine, Kerr of seven cavities has been obtained at different flux bias points. As theoretically expected in Section 2.3.4, we observe an increase of Kerr with Φ_{loop}. Detuning from the flux sweet spot leads to an increase in nonlinear SQUID inductance. Hence, the effective SQUID participation ratio increases, and the circuit becomes more nonlinear.

The solid lines represent the theoretical predictions for Kerr based on Eq. (2.76). The parameters used to calculate these theoretical curves include the SQUID participation ratios β_{r}, which were obtained by fitting the tuning behaviour of the individual cavities, shown in Fig. 3.8. For the geometric inductance L, values of 4.96 nH for the long samples (*WSQLx*) and 4.67 nH for the short samples (*WSQx*) were used. These inductances were obtained by R. Sathyanarayanan, by simulating the design of the stripline cavity in *Ansys HFSS*.

As expected, a trend is observed in which cavities with larger SQUID participation ratios tend to exhibit higher Kerr constants. However, comparing the absolute values obtained with the nonlinear circle fit to the theory curves, we see that samples with larger participation ratios tend to exhibit lower Kerr constants than theoretically expected from fitting their tuning behaviour. This discrepancy is particularly pronounced for *WSQL9*, which, according to its tuning behaviour, has the highest participation ratio among all characterised samples.

As discussed in Section 3.3, for samples with an intrinsically high SQUID participation ratio, neglecting the junction capacitance might lead to an overestimation of the SQUID participation ratio and could explain the observed discrepancies.

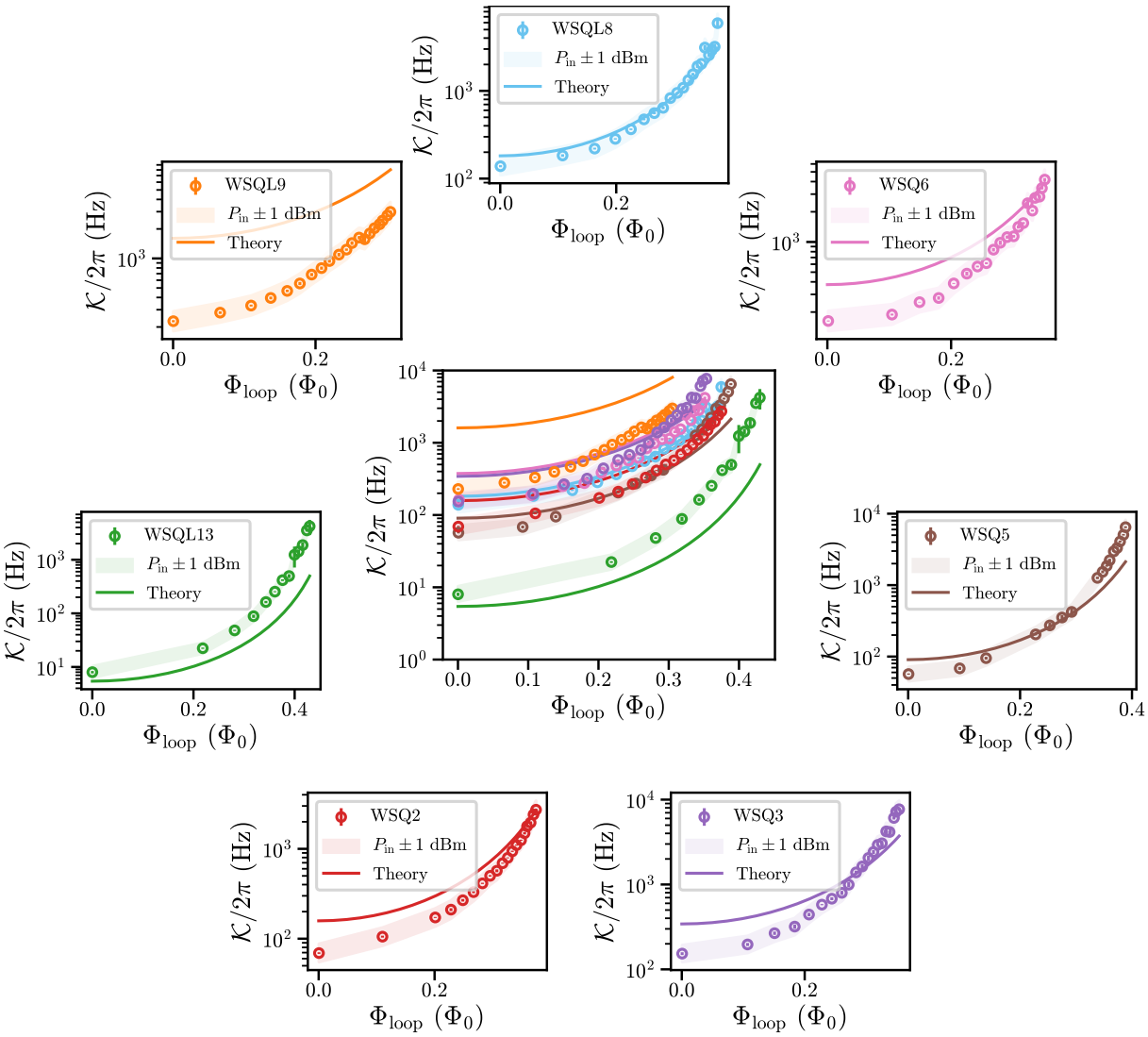

Fig. 3.14 Kerr for seven measured cavities at different detunings from the sweet spot. Data points and the corresponding error bars represent the mean and standard deviation of Kerr obtained by the nonlinear circle fit routine in the range of $P_{\mathrm{in}} = P_{\mathrm{in,bi}} \pm 3\,\mathrm{dBm}$. The shaded areas indicate the variation in Kerr for a $\pm 1\,\mathrm{dBm}$ change in input power, reflecting the uncertainty in determining the input attenuation. Solid lines represent the theoretical behaviour according to Eq. (2.76), using the SQUID participation ratios obtained from fitting the tuning behaviour in Fig. 3.8. For the geometric inductance L of the cavity, simulated values of 4.96 nH for long samples (*WSQLx*) and 4.67 nH for shorter samples (*WSQx*) were used. The central plot allows for a direct comparison of the seven cavities.

CHAPTER 4

Sample preparation

This chapter discusses the modification of AFM cantilevers with magnetic particles and the alignment and mounting process of these cantilevers on top of the microwave cavity's SQUID loop. We will investigate the precision and reproducibility of these processes and study the influence of the magnetic particle on the mechanical properties of the cantilever.

The following picture shows cavity *WSQL13* with cantilever *C7* placed above the SQUID. The sample is fixed in a copper clamp for mounting in the waveguide. Picture taken by D. Jordan.

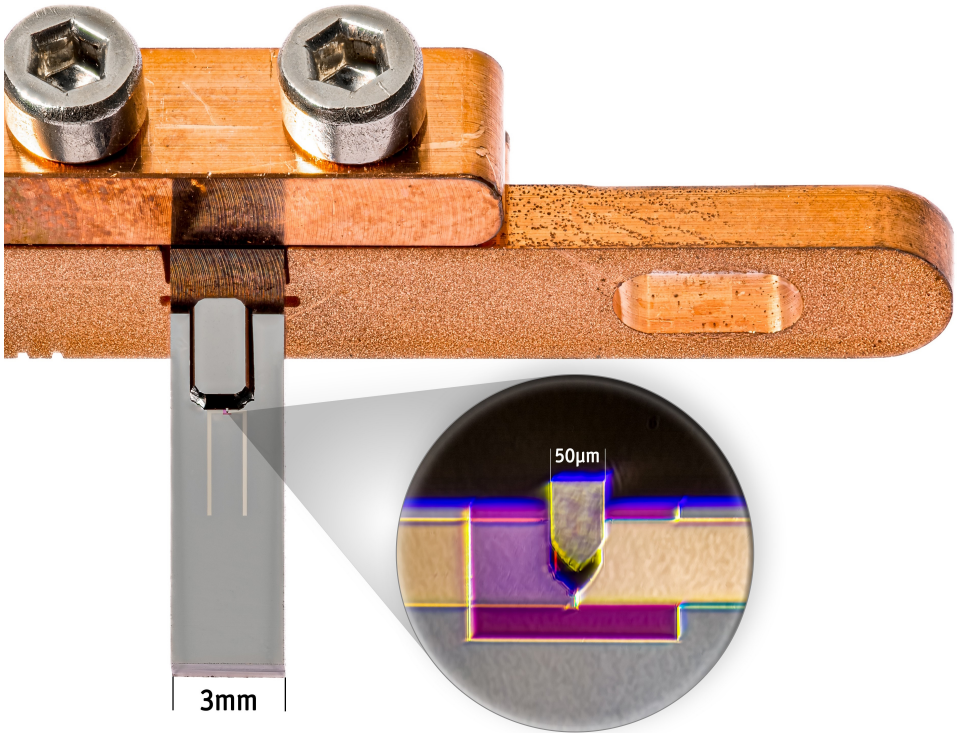

4.1 Modification of AFM cantilevers with magnetic particles

As described in Section 2.7, inductive coupling of an AFM cantilever to the microstrip SQUID cavity is achieved by attaching a magnetic particle to the tip of the cantilever. This is done in-house under an optical microscope.

We use commercially available, tipless silicon cantilever chips, *AIO-TL* from *Budget Sensors*, shown in Fig. 4.4 a). Each chip has four cantilevers with varying dimensions, but only the shortest, highest-frequency cantilever is used. The nominal dimensions of this cantilever are 100 µm in length, 50 µm in width and 2.7 µm in thickness. It has a nominal spring constant of 40 N/m and a resonance frequency of 350 kHz. However, the manufacturer specifies a broad range with typical spring constants from 7 N/m to 160 N/m and resonance frequencies from 200 kHz to 500 kHz [93].

To avoid confusion during the later mounting process, the longer, unused cantilevers are broken off using the tip of a probe station. This ensures that only the intended cantilever remains for modification. Magnetic neodymium iron boron (NdFeB) powder with grain sizes ranging from about 1 µm to 100 µm is prepared on a glass slide. Using the cantilever as a size reference, a particle of approximately 10 µm to 25 µm in size is selected under the optical microscope and picked up using the tip of the probe station. Subsequently, a small drop of epoxy *STYCAST 1266* is applied to the cantilever tip using a 50 µm thin copper wire. The selected magnetic particle is then placed onto the epoxy-covered tip. The entire chip is put onto a hotplate at 50 °C for at least 2 h to cure the epoxy and securely fix the particle to the cantilever. Finally, the magnetic particle is magnetised in the field of a 2 T permanent magnet [94].

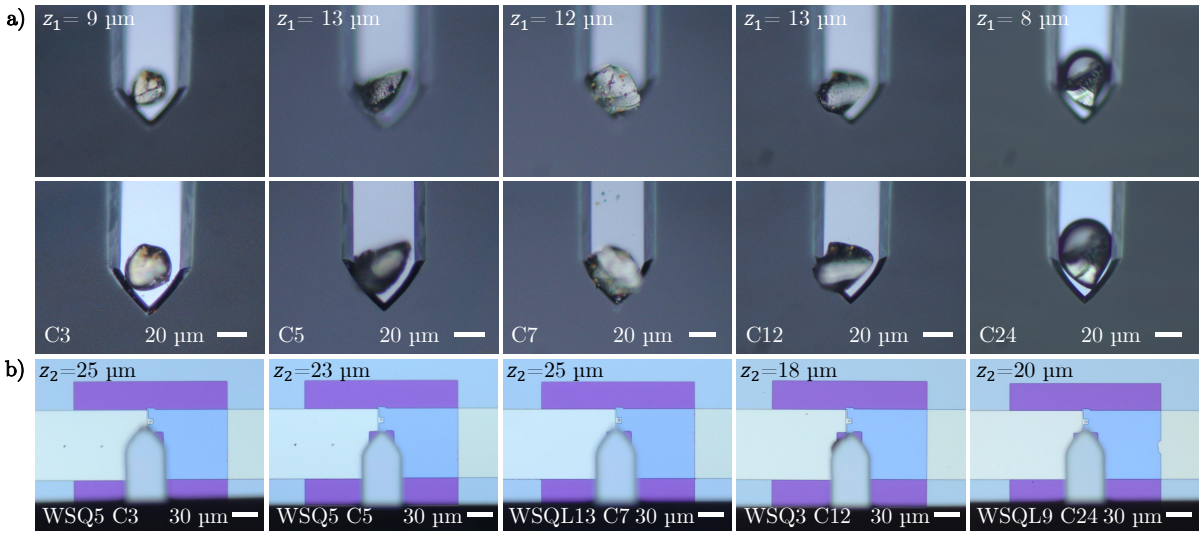

Fig. 4.1 **a)** Optical microscope images of AFM cantilevers with attached NdFeB particles. Bottom pictures with focus on the cantilever, top pictures with focus on the highest point of the particle. The distance z_1 between the two focal planes corresponds to the approximate height of the particle. **b)** Cavities with mounted cantilevers. The distance z_2 is measured between the SQUID and the top of the cantilever, see Fig. 4.4 b). The initially mounted cantilever *C5* that was mounted originally on *WSQ5* did not couple well to the SQUID cavity and was later replaced by *C3*.

In Fig. 4.1 a), five different cantilevers with attached magnetic particles can be seen. Using the focus of the optical microscope, the approximate height z_1 of the particles is determined. Even though all particles shown here are quite similar in size, it is evident from the figure that the shape of the particles varies significantly. This reflects the heterogeneous nature of the particles in the powder, making manual selection challenging and resulting in a yield of only about one good cantilever out of five.

A recent improvement in the selection process of magnetic particles involves using a wafer patterned with a structured grid, providing a consistent size reference during particle selection. Optical microscope images of this wafer, covered by magnetic powder, are shown in Fig. 4.2. From the highest-magnification image, it can be seen that the probe tip is placed close to a particle with a suitable size.

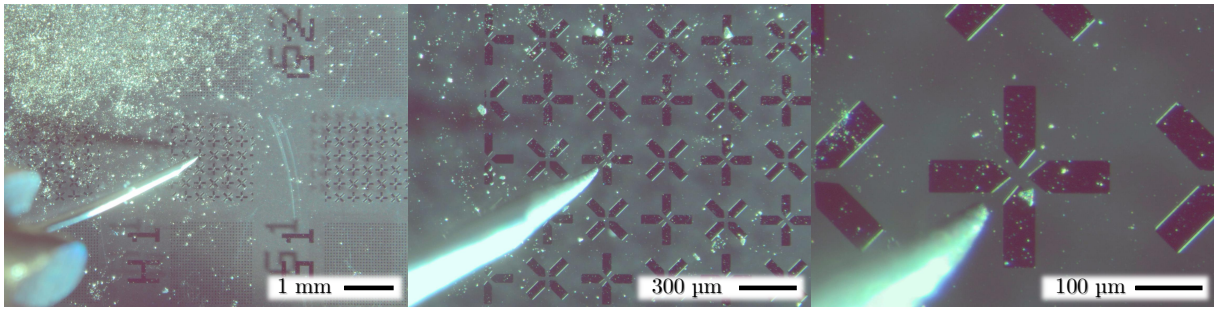

Fig. 4.2 Sapphire wafer with NdFeB powder. The patterned grid, shaped like the cantilever, allows for a consistent size reference when selecting particles from the powder. The visible probe tip is used to pick up a particle and place it on the tip of a cantilever. The wafer was fabricated in our cleanroom by B. Thyagarajan.

For future enhancements, a different powder with more homogenous particles or pre-selecting particles using a sieve could improve reproducibility. An even more controlled approach would be to deposit magnetic material directly onto the cantilever tips. However, this method poses challenges due to slow deposition rates and the need for relatively thick layers to achieve a sufficiently strong magnetic field for effective coupling.

4.1.1 Change of mechanical properties after adding a particle

To investigate the influence of attaching a magnetic particle to the cantilever, we measure its response to a piezo drive in an AFM, before and after attaching the particle. The oscillation amplitude is measured by focusing the laser of the AFM on the cantilever's tip.

The result of such a measurement can be seen in Fig. 4.3 a). Before attaching the particle (dark blue trace), the cantilever has a fundamental mode frequency of $\Omega_\mathrm{m} = 488.15(9)\,\mathrm{kHz}$ and a linewidth of $\Gamma_\mathrm{m} = 3.3(5)\,\mathrm{kHz}$. After mounting a particle to the cantilever's tip (light blue trace), the frequency and linewidth reduce to $\tilde{\Omega}_\mathrm{m} = 343.39(4)\,\mathrm{kHz}$ and $\tilde{\Gamma}_\mathrm{m} = 1.2(2)\,\mathrm{kHz}$.

Using the cantilever's dimensions and known material parameters, we can calculate some key properties of the bare cantilever without a magnetic particle. Given the density of silicon $2329\,\mathrm{kg/m^3}$ [95] and the cantilever dimensions $100(5)\,\mu\mathrm{m}$ x $50.0(2.5)\,\mu\mathrm{m}$ x $2.7(0.5)\,\mu\mathrm{m}$ [93] (assuming that the manufacturer provides these values as a 95.5 % confidence interval), we can

calculate the total mass of the cantilever as

$$m_{\text{beam}} = 31(6)\,\text{ng}, \tag{4.1}$$

where we neglected its exact shape. For the effective mass of the cantilever (see Eq. (2.97)) we therfore get $m_{\text{eff}} = m_{\text{beam}}/4 = 8(2)\,\text{ng}$.

With the dimensions of the cantilever and the Young's modulus for silicon 169 GPa [96], we can use Eq. (2.99) to calculate a spring constant of 43(25) N/m. This matches well with the nominal spring constant of 40 N/m stated by the manufacturer [93]. Using the measured frequency of cantilever *C3* (see Fig. 4.1 and 4.3) and the estimated cantilever mass, we get a spring constant of $k = \Omega_m^2 m_{\text{eff}} = 74(15)\,\text{N/m}$. This matches the value predicted from the cantilever dimensions within 2σ and lies within the quite broad typical range of 7 N/m to 160 N/m specified by the manufacturer [93].

As discussed in Section 2.7.1.1, the observed decrease in the fundamental mode frequency after attaching a magnetic particle can be explained by the added mass. We will now use the measured frequencies before and after mounting the particle to estimate the mass of the particle.

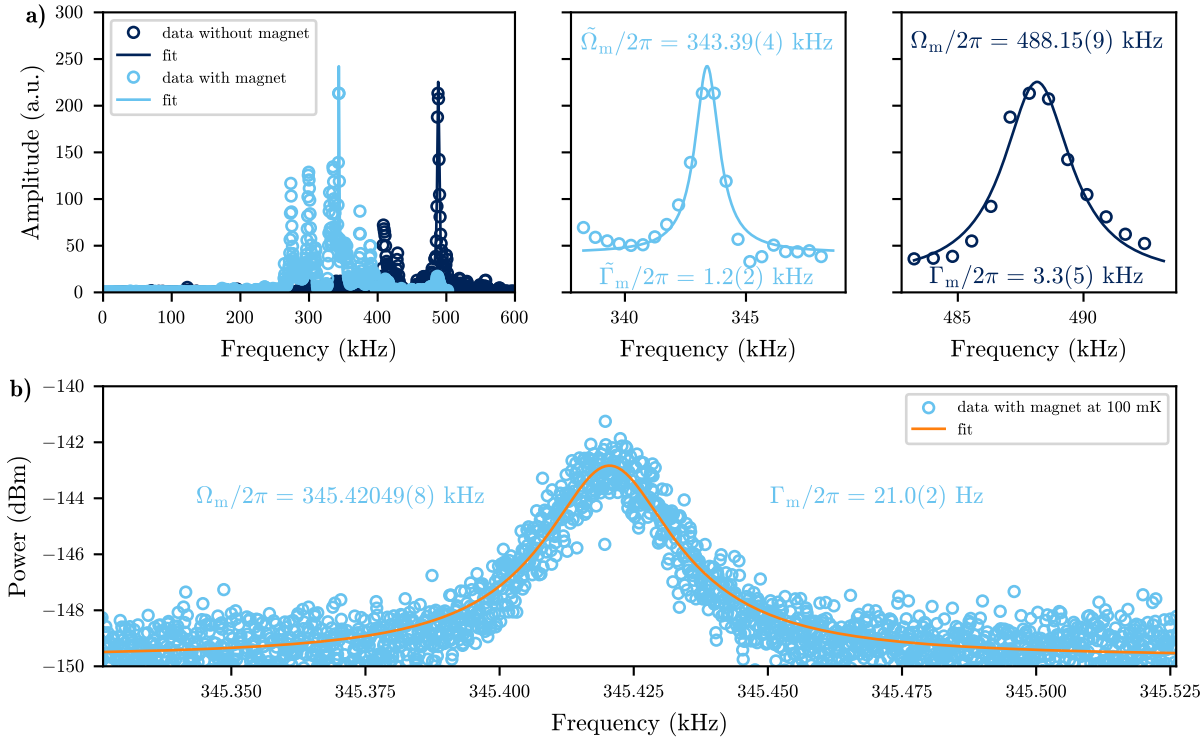

Fig. 4.3 **a)** Mechanical spectrum of cantilever *C3* before and after mounting of the magnetic particle. Spectra were measured at room temperature in an AFM, exciting the cantilever with a piezo. Plots on the right show zoom-ins on the highest amplitude peaks with respective Lorentzian fits. The origin of the additional visible peaks could not be fully clarified. They might result from vibrational noise that excites the cantilever during the piezo scan or stray reflections of the laser. **b)** Mechanical sideband at 100 mK, measured in the cryostat, after mounting *C3* on cavity *WSQ5*. The orange line shows a Lorentzian fit of the data.

Assuming the particle is light enough not to change the spring constant, we can use Eq. (2.98) and Eq. (2.103) to derive

$$\frac{m_{\mathrm{p,eff}}}{m_{\mathrm{eff}}} = \left(\frac{\Omega_{\mathrm{m}}}{\tilde{\Omega}_{\mathrm{m}}}\right)^2 - 1. \tag{4.2}$$

In case of cantilever *C3*, this yields an effective particle mass of $m_{\mathrm{p,eff}}/m_{\mathrm{eff}} = 1.0208(9)$ times the effective mass of the cantilever. This corresponds to about $m_{\mathrm{p,eff}}/m_{\mathrm{beam}} = 0.2552(2)$ times the actual mass of the cantilever. From the approximate mass of the cantilever, we get $m_{\mathrm{p,eff}} = 0.2552(2) \cdot m_{\mathrm{beam}} = 8.0(1.6)\,\mathrm{ng}$. Using the density of $7.6(2) \cdot 10^3\,\mathrm{kg/m^3}$ for NdFeB [97], this would correspond to a sphere with a diameter of $12.6(8)\,\mu\mathrm{m}$.

This is smaller than expected from the image in Fig. 4.1, which shows that the particle has a dimension of about $25(2)\,\mu\mathrm{m}$ x $25(2)\,\mu\mathrm{m}$ x $9(1)\,\mu\mathrm{m}$. Assuming the particle is shaped like an ellipsoid, this would correspond to a mass of $m_{\mathrm{p}} = 22(4)\,\mathrm{ng}$. However, we have to consider that the obtained value of $m_{\mathrm{p,eff}} = 8.0(1.6)\,\mathrm{ng}$ is only the effective mass of the particle.

The microscope image in Fig. 4.1 shows that the particle does not sit at the very end of the cantilever, but at a distance of about $l_{\mathrm{beam}} - l_{\mathrm{p}} = 26(2)\,\mu\mathrm{m}$ from the tip of the cantilever. Using Eq. (2.104) and the fundamental mode shape of the cantilever, plotted in Fig. 2.14 b), we get a ratio of $m_{\mathrm{p,eff}}/m_{\mathrm{p}} \approx (D_1(l_{\mathrm{p}}))^2 = 0.42(4)$. This yields that the real mass of the particle is $m_{\mathrm{p}} = m_{\mathrm{p,eff}}/0.42(4) = 19(4)\,\mathrm{ng}$, which is consistent with the mass of $m_{\mathrm{p}} = 22(4)\,\mathrm{ng}$, estimated from the dimensions of the particle.

Besides the change in mechanical frequency due to the added mass, we also observe a decreased mechanical linewidth after attaching the particle. At atmospheric pressure, the mechanical quality factor of cantilevers is usually limited by damping by the surrounding air [98, 99]. This damping force scales with the area $l_{\mathrm{beam}} w_{\mathrm{beam}}$ of the cantilever. Since adding a particle on top of the cantilever does not change this area but decreases the velocity of the cantilever's motion, the damping force is reduced. At the same time, the effective mass increases, leading to an overall decrease in damping.

4.1.2 Mechanical properties in the cryostat

After mounting the cantilever *C3* on a SQUID cavity and cooling it down in the cryostat, we were able to measure the mechanical signal shown in Fig. 5.7 b). The Lorentzian fit (orange line) yields a mechanical frequency of $\Omega_m = 345\,420.49(8)\,\mathrm{Hz}$ and a mechanical linewidth of $\Gamma_{\mathrm{m}} = 21.0(2)\,\mathrm{Hz}$. Note that this measurement was performed such that optomechanical backaction (discussed in Section 5.4) does not influence the mechanical properties.

Comparing the measured linewidth of $21.0(2)\,\mathrm{Hz}$ at 100 mK to the linewidth of $1.2(2)\,\mathrm{kHz}$ at atmospheric pressure and room temperature, we observe a significant reduction in damping. This reduction primarily results from the high vacuum environment in the cryostat, which effectively eliminates air damping. In vacuum, intrinsic loss mechanisms such as clamping losses and thermoelastic dissipation limit the mechanical quality factor. It has been observed that decreasing the temperature significantly reduces these intrinsic loss mechanisms [98]. For a more detailed discussion on intrinsic loss mechanisms, we refer the reader to Ref. [99].

Comparing the measured mechanical frequency at 100 mK to the value at room temperature,

we observe an increase of 2.03(4) kHz. This frequency shift could be attributed to an increase in the cantilever's spring constant due to a rise in the Young's modulus at lower temperatures. According to Ref. [100], decreasing the temperature from room temperature to near absolute zero leads to an increase in Young's modulus of approximately $\Delta E = 2.2(3)$ GPa, corresponding to a relative change of $\Delta E/E = 1.3(2)$ %. However, this estimate should be interpreted with caution, as the reference extrapolates Young's modulus for temperatures below 80 K rather than relying on direct measurements. Nevertheless, assuming this extrapolation holds, we can estimate the effect on the cantilever's frequency.

As the cantilever's spring constant is proportional to Young's modulus (see Eq. (2.99)) and the mechanical frequency is proportional to the square root of the spring constant, we get

$$\frac{\Omega_{\mathrm{m,cold}}}{\Omega_{\mathrm{m,warm}}} = \sqrt{1 + \frac{\Delta E}{E}} = 1.0065(9). \tag{4.3}$$

For cantilever *C3*, this corresponds to an absolute increase in frequency of 2.2(3) kHz, which very well matches the measured value of 2.03(4) kHz.

Note that a change in damping can also lead to a shift in mechanical frequency. However, even for the rather strong damping at room temperature, this only leads to a change on the order of 1 mHz, which is negligible and cannot account for the observed frequency shift of 2 kHz.

4.2 Mounting of AFM cantilevers on tunable cavities

After modifying the cantilever with a magnetic particle, it is placed above the SQUID of the microwave cavity. This is done using a flip-chip approach, where the cantilever chip is flipped and placed onto the silicon substrate of the SQUID cavity. GE varnish is used to hold the cantilever chip in place.

To achieve strong coupling between the cantilever and the cavity, precise alignment of the two chips on the scale of a few µm is required. For all samples prepared prior to this thesis, alignment was performed manually with tweezers under an optical microscope. This approach, though functional, was challenging and often resulted in suboptimal alignment in the xy-plane, very limited control over the z-distance and a significant number of destroyed cantilevers.

This substantially improved with the design of a mounting stage by L. F. Deeg, shown in Fig. 4.5. The mounting stage consists of two separate parts: a cantilever holder and a cavity holder. The cantilever holder, shown in Fig. 4.5 a), is connected to a vacuum pump that holds the cantilever chip in a machined groove. The cantilever holder can then be flipped and screwed onto the cavity holder. The complete assembly is shown in Fig. 4.5 b). A SQUID cavity is placed on the cavity holder, which is mounted on a two-dimensional translation stage with micrometre screws for precise alignment in the xy-plane. Above the cavity, the cantilever holder is mounted on a vertical translation stage. This allows for carefully lowering the cantilever onto the SQUID cavity while simultaneously observing and fine-tuning its alignment in the xy-plane using an optical microscope.

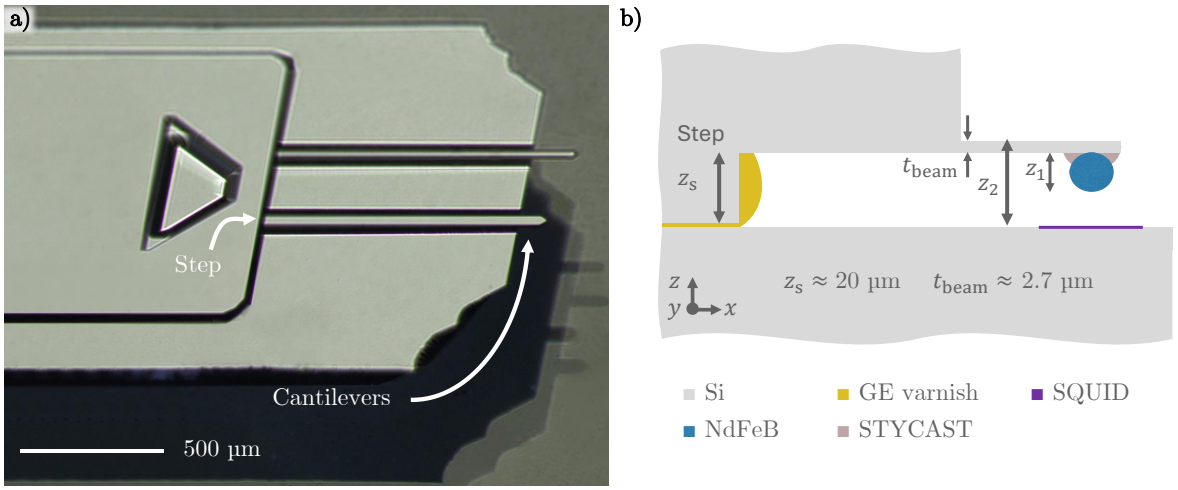

Fig. 4.4 **a)** Optical microscope image of a cantilever chip with two visible cantilevers of different lengths. Only the shorter ≈ 100 µm, higher frequency one is used. The visible step is utilised as a spacer when mounting the cantilever onto a cavity chip. **b)** Schematic view from the side of a cantilever chip, flipped and mounted onto a cavity. Step with a height of $z_s \approx 20$ µm allows for a reproducible distance between the cantilever and the SQUID loop.

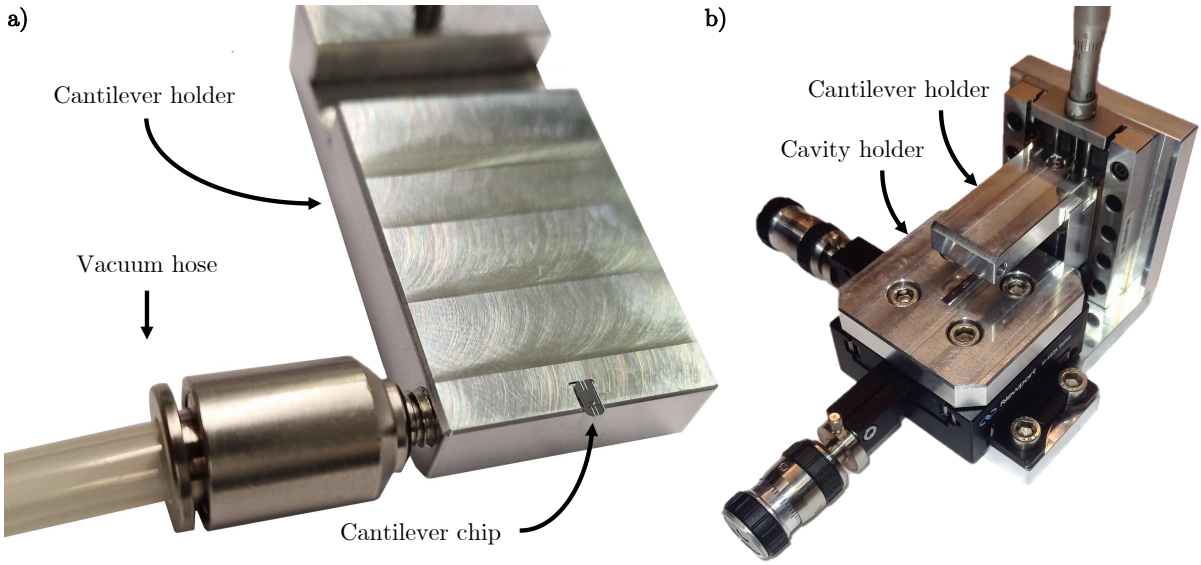

Fig. 4.5 Mounting stage for precise placement of the cantilever over the SQUID loop. **a)** The cantilever holder, connected to a vacuum pump, holds the cantilever chip in a machined groove. **b)** Complete mounting stage, with the cantilever holder mounted to a vertical translation stage above the cavity holder. A SQUID cavity is placed on the cavity holder, which is mounted onto a xy-translation stage. The micrometer screws allow precise alignment of the chips under an optical microscope. Picture taken by L. F. Deeg.

Fig. 4.6 shows five different cantilever chips mounted on SQUID cavities. To verify the proper alignment of the magnetic particles with respect to the SQUID loop, we overlaid images of the mounted cantilevers (Fig. 4.1 b)) with mirrored and correctly scaled images of the cantilever backsides taken before mounting (Fig. 4.1 a)). Additionally, the SQUID loop area is marked with a dashed orange line, allowing a direct comparison with the particle positions.

The images confirm that all particles are well aligned with the SQUID loop, with only minor offsets for cantilevers *C3* and *C5*. However, cavity *WSQ5*, which initially had cantilever *C5* mounted on it, showed only a very weak mechanical signal. Cantilever *C5* was consequently replaced by *C3*. We suspect that the weak coupling to cantilever *C5* may be due to the different structure of its particle. While other particles appear monolithic and shiny, the particle of *C5* appears porous and dark in the optical microscope image.

To ensure consistent spacing in the z-dimension, a step originating from the fabrication process of the cantilever chip is utilised. This step has a height of 20 µm and is visible in the optical microscope image in Fig. 4.4 a). Fig. 4.4 b) shows a schematic representation with the relevant dimensions in the z-direction.

Looking at the obtained distances z_2 between the backside of the cantilever and the SQUID loop in Fig. 4.6, we see that the step allows for quite consistent distances with a mean of 22 µm and a standard deviation of 3 µm. The remaining variations in z_2 are most probably given by the varying and sometimes uneven thickness of the GE varnish layer underneath the cantilever chip. For cantilevers *C12* and *C24*, a slight tilt of the cantilever chip about the y-axis toward the SQUID loop could explain the distances smaller than the step height. This can happen if the initially applied GE varnish is not centrally applied beneath the body of the cantilever chip.

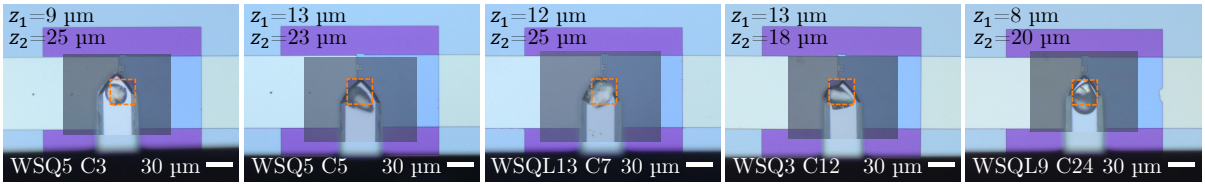

Fig. 4.6 Overlay of the optical microscope images shown in Fig. 4.1 a) and b). The orange line marks the area of the SQUID loop. As can be seen from the images, the magnetic particles are well aligned with the SQUID loop.

Using these distances, we can roughly estimate the magnetic field at the SQUID from the remanent field of about $B_{\mathrm{rem}} = 1.2\,\mathrm{T}$ for NdFeB [101]. For a spherical particle with a diameter z_1, the field at the SQUID for a given distance z_2 can be approximated as

$$B = \frac{2}{3}\frac{(z_1/2)^3}{(z_2 - t_{\mathrm{beam}} - z_1/2)^3} B_{\mathrm{rem}} \tag{4.4}$$

For the obtained dimensions, this yields values in the order of 10 - 100 mT at the SQUID.

CHAPTER 5

Characterisation of magnetomechanical samples

In this chapter, we discuss the results from the characterisation of the prepared magnetomechanical samples. We begin by describing the experimental setup, which, apart from the components already used in Chapter 3, includes a vibration isolation setup and additional microwave components required to measure the motion of the cantilevers.

We then explain the detection principle of the mechanical motion and introduce a calibration method required to obtain the mechanical occupation. This is followed by a discussion of improvements made to the thermalisation of the vibration isolated setup.

Subsequently, we investigate the influence of the magnetic cantilever on the SQUID cavities, including modifications to their tuning behaviour and the impact on internal quality factors.

Finally, we present measured mechanical signatures and discuss the obtained mechanical properties of the various samples. We analyse how these properties change with applied flux bias and temperature. We complete the chapter with measurements of optomechanical backaction cooling performed on one of the prepared samples and a discussion of the corresponding results.

5.1 Experimental setup

To characterise the prepared optomechanical samples, we use the same waveguide setup as described in Section 3.1. As the bare microwave cavities, the samples with cantilevers are mounted in copper clamps and placed in a waveguide. As shown in Fig. 5.1, the microwave wiring inside the cryostat and the DC wiring remain identical to the one used for characterisation of samples without mechanics. As before, the VNA is used to measure the cavity scattering parameter.

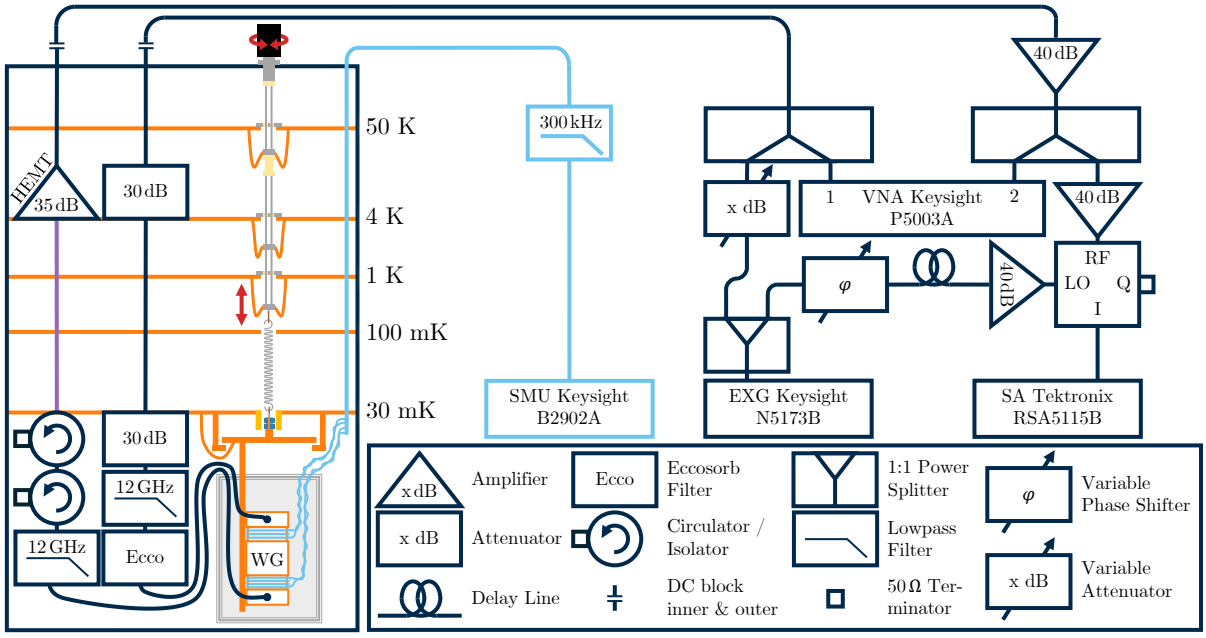

Fig. 5.1 Measurement setup for characterisation of mechanics samples. Parallel to the VNA, a signal generator and analyser are used for optomechanical cooling and detection of the cantilever motion. For calibration of the phonon occupation, the signal is mixed down to baseband with an IQ-mixer. More details on the microwave setup are discussed in the main text.

To isolate the mechanics samples from vibrations of the pulse tube cooler, the waveguide and the magnetic shields are suspended on a spring [9]. To avoid sustained oscillations, the spring-mass system is damped with an eddy current damper, consisting of a brass tube (gold) mounted to the baseplate and NdFeB magnets (blue) attached to the top of the can. To thermalise the suspended setup, it is thermally anchored to the base plate with flexible copper braids. For faster thermalisation during cooldown, a mechanical vacuum feedthrough allows for lowering the setup onto copper pieces, which are rigidly connected to the baseplate. To avoid excessive headload on the upper stages, we use stainless steel rods interrupted by Teflon spacers (beige) to connect the spring and the feedthrough. To connect the spring, we use nylon wire (brown).

5.1.1 Measurement of the mechanical motion

For optomechanical cooling and detection of the cantilever motion, an additional microwave setup is connected in parallel to the VNA. A signal generator *Keysight N5173B* creates a coherent probe tone. One part of this tone is sent into the cryostat, while the other part is used as the local oscillator (LO) of an IQ-mixer *Marki MMIQ-0416LS*. The probe tone power entering the cryostat is controlled using a variable attenuator *Mini-Circuits RCDAT-30G-30*. After interacting with the optomechanical system, the transmitted probe tone is sent to the RF port of the IQ-mixer. The down-mixed signal at the I port is recorded and transformed to a spectrum using a signal analyser *Tektronix RSA5115B*. To match the electrical delay and phase of the signals at the LO and RF ports of the mixer, a delay line and a variable phase shifter *Vaunix LPS-123* are used.

As described in the appendix of Ref. [7], the interaction of the probe tone with the cavity can be understood as an amplitude and phase modulation. As illustrated in Fig. 5.2, tuning the SQUID cavity to a flux sensitive bias point Φ_{bias} causes the cantilever's motion to modulate the cavity's resonance frequency with a peak frequency deviation given by $\Delta\omega_{\mathrm{c}} = g_0\sqrt{\bar{n}_{\mathrm{m}}}$. This

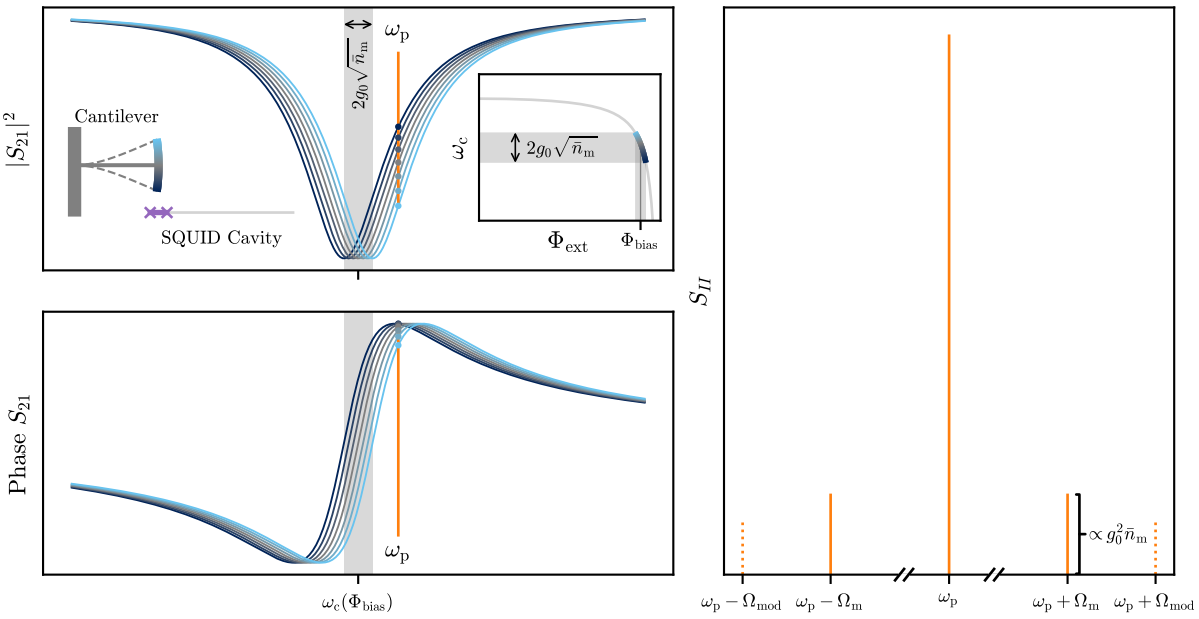

Fig. 5.2 Illustration of cantilever motion detection via a probe tone. After tuning the cavity to a flux-sensitive bias point, the cantilever's motion modulates the cavity frequency. This causes a periodic variation in the transmission through the waveguide. Therefore, a probe tone transmitting through the waveguide undergoes phase and amplitude modulation. For weak modulation $g_0\sqrt{\bar{n}_{\mathrm{m}}} \ll \kappa_{\mathrm{l}}$, this leads to two sidebands spaced by the mechanical frequency around the probe tone. The height (or, in case of finite mechanical linewidth, the area) of these sidebands is proportional to $g_0^2\bar{n}_{\mathrm{m}}$. As described in more detail in the main text, the corresponding proportionality factor can be obtained by weak frequency modulation of the probe tone at a frequency $\Omega_{\mathrm{mod}} \simeq \Omega_{\mathrm{m}}$ close to the mechanical frequency. This results in two additional sidebands (dotted lines) at $\omega_{\mathrm{p}} \pm \Omega_{\mathrm{mod}}$, which can be used to calibrate the mechanical sidebands.

creates a periodic change in the S_{21} scattering parameter. Consequently, a probe tone that passes through the waveguide undergoes phase and amplitude modulation. For small variations of the cavity frequency $\Delta\omega_c \ll \kappa_l$, this results in two sidebands symmetrically spaced around the probe tone by the mechanical frequency. In the noise power spectrum S_{II}, the amplitude (or, for finite mechanical linewidth, the area) of these sidebands is proportional to $\Delta\omega_c^2 = g_0^2\bar{n}_m$.

In addition to g_0 and $\bar{n}_m$, the amplitude of the sidebands is also influenced by the shape of the cavity response. Tuning the probe tone further away from the cavity resonance, toward frequencies where the variation in S_{21} is reduced, leads to a smaller sideband amplitude, even for a weak probe tone that does not change the mechanical occupation. Additionally, the sideband amplitude depends on the gain of the output amplifier chain between the sample and the signal analyser. On top of that, the absolute height is affected by the probe tone power, which is set by the input attenuation between the signal generator and the sample. As a result, accurately extracting $g_0^2\bar{n}_m$ from the measured spectra requires determining the proportionality factor that relates the observed sideband amplitude to these parameters.

A calibration method that allows for obtaining this factor is described in Ref. [102]. A weak frequency modulation of the probe tone with a peak frequency deviation $\Delta\omega_p$ and a modulation frequency $\Omega_{mod} \simeq \Omega_m$ close to the mechanical frequency causes two additional sidebands to appear in the spectrum (dashed lines in Fig 5.2). Frequency modulating the probe tone mimics the effect of a modulation in cavity frequency caused by the cantilever, as both correspond to a relative frequency change between the cavity and the probe tone. Assuming the cavity response and the output amplifier chain are flat enough over the small frequency difference $\Omega_m - \Omega_{mod} \ll \kappa_l$ (we typically use 300 Hz), such that both the mechanical and the modulation sidebands are equally affected, the latter can be used to calibrate the measured spectra.

To suppress higher-order frequency modulation sidebands, plotted in Fig. 5.3, the modulation index $\Delta\omega_p/\omega_{mod}$ must remain well below 1. Additionally, in case of strong backaction, keeping the peak frequency deviation $\Delta\omega_p$ as small as possible is important to avoid washing out the cooling feature by averaging over different detunings. This is in particular important in the nonlinear cavity regime, where a small change in detuning can significantly alter the cooling performance (see Fig. 2.5 b)). We therefore choose $\Delta\omega_p$ as small as possible (typically $\Delta\omega_p/\omega_{mod} \lesssim 0.4$), but still big enough for a calibration tone at least 3 dB above the noise floor.

As the probe tone, and consequently the signal at the LO, is frequency modulated, it is crucial to match not only the phase but also the electrical delay between the signals at the LO and RF ports. This ensures that the signal returning from the cryostat is mixed down with the same signal that was initially sent into the cryostat. To ensure this, we use the VNA to measure the electrical delay between the output of the signal generator and the LO and RF ports. By adjusting the length of the delay line, we match the delay of the two signal paths to <10 ps, which is smaller than one period of an 8 GHz microwave signal ($\approx$ 125 ps). We then use the variable phase shifter to adjust for the remaining phase difference. As the transmission through the fridge and the delay line has phase ripples, the phase has to be adjusted for every probe tone frequency. To ensure proper phase matching, we send in a frequency-modulated probe tone, detune the cavity from this tone, and then adjust the phase until the modulation sideband on the I-port of the mixer cancels below the noise floor. After tuning the cavity back on resonance, the modulation sideband reappears and allows for calibration of the mechanical sideband.

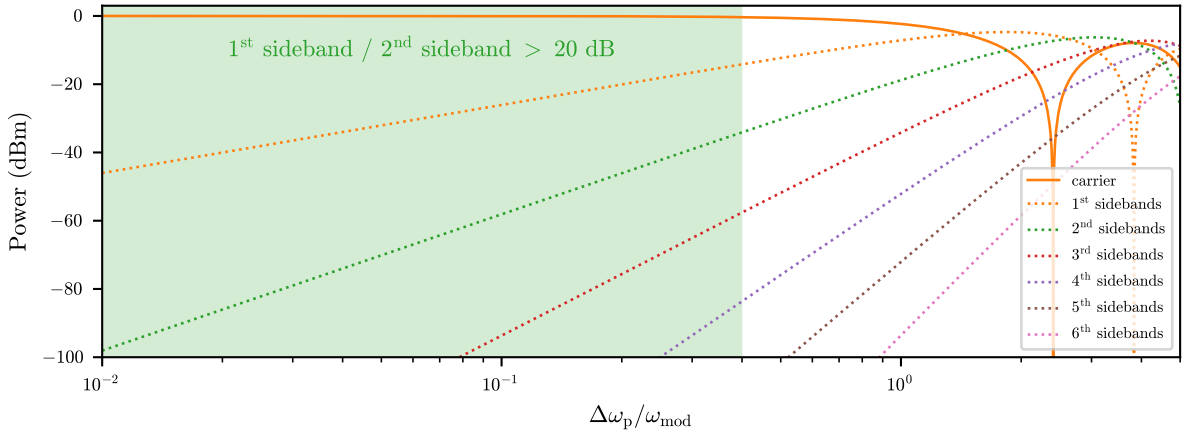

Fig. 5.3 Spectral components of a frequency modulated signal, given by the Bessel functions of the first kind, normalised to a total signal power of 0 dBm. Sideband powers represent the total power in both the upper and lower sidebands at $\omega_\mathrm{p} \pm n\omega_\mathrm{mod}$ for each order n. The green shaded region indicates the range of modulation indices where the power in the 2nd sideband is more than 20 dB lower than that of the 1st sideband.

After matching the phase, the product of the optomechanical coupling strength and the mechanical occupation can be extracted from the mixed down spectrum at the I port as

$$g_0^2 \bar{n}_\mathrm{m} = \frac{1}{2}\frac{\Delta\omega_\mathrm{p}^2}{2}\frac{S_\mathrm{II}(\Omega_\mathrm{m})\Gamma_\mathrm{m}/(4\cdot\mathrm{ENBW})}{S_{II}(\Omega_\mathrm{mod})}, \tag{5.1}$$

where ENBW is the effective noise bandwidth of the signal analyser in Hz and all other quantities are in angular frequencies [102]. The numerator of the last fraction corresponds to the area of the mechanical sideband, while the denominator is given by the height of the calibration tone.

5.1.1.1 Temperature ramp - Extraction of g_0

In order to obtain $\bar{n}_\mathrm{m}$ via the cavity, the coupling rate g_0 must be known. Assuming the mechanical mode is thermalised to the temperature of the cryostat, we can use Eq. (2.17) to determine the mechanical occupation independently.

To verify thermalisation, the product $g_0^2\bar{n}_\mathrm{m}$ can be measured at different cryostat temperatures. To avoid any influence on $\bar{n}_\mathrm{m}$ from optomechanical backaction, a low-power probe tone, resonant with the cavity, is used. If the mechanical mode is thermalised, one observes that

$$g_0^2\bar{n}_\mathrm{m} = g_0^2\frac{1}{e^{\hbar\Omega_\mathrm{m}/k_\mathrm{B}T}-1} \approx g_0^2\frac{k_\mathrm{B}T}{\hbar\Omega_\mathrm{m}} \quad \text{for} \quad k_\mathrm{B}T \gg \hbar\Omega_\mathrm{m}. \tag{5.2}$$

Plotting $g_0^2\bar{n}_\mathrm{m}$ against T and applying a fit allows one to obtain g_0.

5.1.2 Vibration isolation setup

To isolate the mechanics samples from vibrations of the pulse tube cooler, L. F. Deeg implemented a vibration isolation setup [9]. As illustrated in Fig. 5.1, the waveguide with the

surrounding can for magnetic shielding is suspended on a spring, hanging from the 1 K plate of the cryostat. To avoid coupling in of vibrations, extra flexible microwave cables *Elspec MK5005* and thin superconducting DC wires *Supercon Inc. 54S43* are used to connect to the waveguide.

Without additional damping, the freely suspended can forms a spring-mass system with a high quality factor. This is undesirable, as a high quality factor amplifies vibrational noise near the system's resonance frequency, leading to sustained oscillations. To mitigate this effect, an eddy current damping setup was implemented, consisting of a brass tube and permanent magnets [9]. As schematically shown in Fig. 5.1, the brass tube is fixed to the baseplate of the cryostat and the permanent magnets are attached to a copper block on top of the can.

5.1.2.1 Thermalisation of the suspended setup

To allow thermalisation of the suspended setup, it is connected to the base plate with flexible copper braids. As can be seen in Fig. 5.4, the usual cooldown time with a rigid screw connection (two M3 screws) is about 1.5 days (grey trace), here the temperature of the setup directly follows the temperature of the base plate. With the suspended setup, it takes almost 7 days to reach 100 mK (dark blue trace). Furthermore, the setup prevents the baseplate from reaching the final temperature for about 6 days.

To reduce cooldown time, we replaced the flexible copper braids with thin annealed copper braids that L. F. Deeg received from the University of Chalmers. Furthermore, we implemented a mechanical vacuum feedthrough, schematically shown in Fig. 5.1. The feedthrough allows for lowering the setup with a weight of about 6 kg onto three copper pieces that are rigidly connected (one M3 screw per piece) to the base plate. To prevent excessive thermal coupling between the upper cryostat plates, we use stainless steel rods with Teflon spacers to interrupt thermal conduction. At each stage, the stainless steel rods are thermalised with copper braids.

As can be seen in Fig. 5.4, the combination of annealed copper braids and lowering the setup during cooldown (light blue trace) significantly reduces cooldown time. The improved setup reaches 100 mK in under 4.5 days, an improvement of approximately 2.5 days over the initial suspended setup. Furthermore, the base plate reaches its final temperature after only 3.5 days, allowing measurements on other rigidly connected experiments to begin earlier.

The small, sudden temperature increase at 5.5 days corresponds to lifting the setup. From that point on, the setup is only thermalised via the copper braids. We observe that the subsequent temperature decrease is still faster than with the previous setup. This suggests that the new annealed copper braids perform better than the previous ones. However, this conclusion must be treated with caution, as we do not measure the temperature of the superconducting magnetic shield. Previous measurements have shown that the temperature of the shield lags. This means that the observed cooling rate after lifting the setup may still be influenced by an already lower temperature of the shield.

To isolate the contribution of the annealed copper braids, we would need to perform a cooldown with the setup lifted throughout, ensuring that thermalisation occurs only via the braids. However, due to time constraints, this has not been done yet. Nevertheless, we can do some calculations to estimate what limits thermalisation of the setup.

Thermal conductivity (or its inverse, thermal resistance) can be separated into two contributions: the thermal conductivity of the bulk material and the thermal conductivity at contact interfaces.

In metals, bulk thermal conductivity has two contributions: electrons and phonons. Around room temperature, thermal conductivity does not show a strong temperature dependence. This is because the increasing number of available phonons is counteracted by increased electron–phonon and phonon–phonon collisions. At lower temperatures, a reduction in those collisions initially leads to increased thermal conductivity. At those temperatures, thermal conductivity becomes sensitive to material impurities, such as the oxygen content. At even lower temperatures, phonon contributions freeze out, and thermal conductivity is dominated by electrons. [103]

At cryogenic temperatures, annealed copper has one of the highest thermal conductivities among materials [104]. Unlike many metals, copper does not become superconducting [105], which is advantageous as Cooper pairs do not contribute to thermal conduction [106]. From room temperature down to approximately 100 K, the bulk thermal conductivity of copper remains nearly constant at about 400 $\mathrm{W/(K \cdot m)}$ [103]. Below this temperature, thermal conductivity begins to vary significantly and becomes dependent on impurities. Commercially available oxygen-free high conductivity (OFHC) copper without additional annealing exhibits a peak thermal conductivity of approximately 2000 $\mathrm{W/(K \cdot m)}$ around 20 K, followed by a linear decrease towards lower temperatures [107].

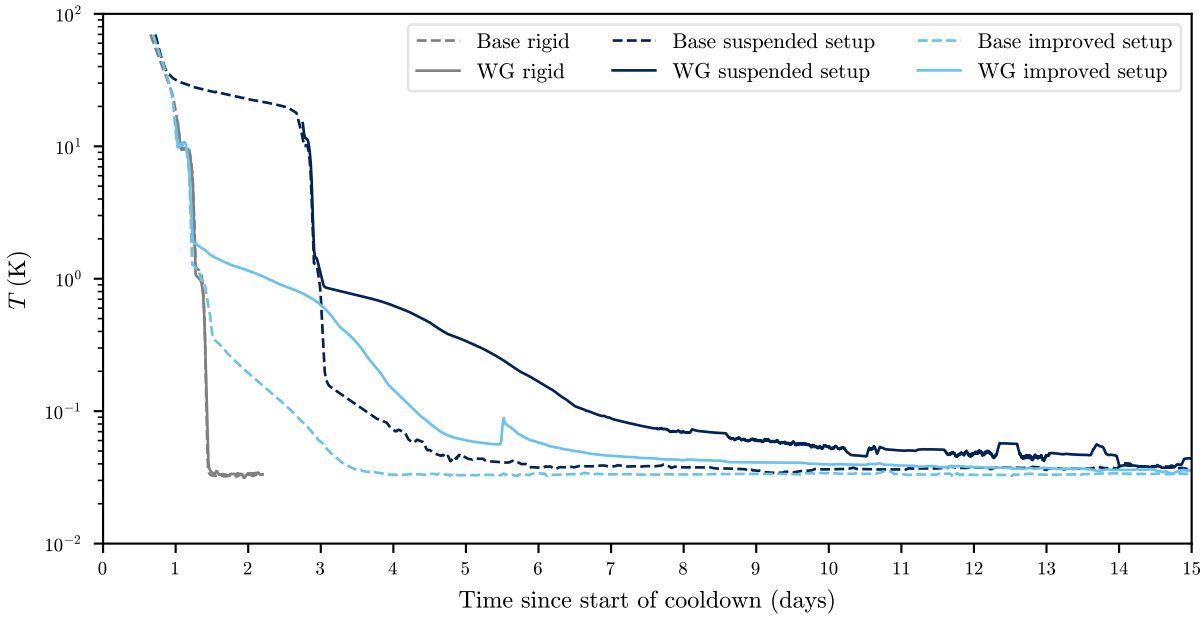

Fig. 5.4 Comparison of temperatures after starting a cooldown with a setup that is rigidly connected to the base plate, the initial version with a suspended setup and the improved version with a mechanical vacuum feedthrough. The dashed lines show the temperature measured by a ruthenium oxide (RuO_2) temperature sensor on the base plate, while the solid lines show the temperature measured by a RuO_2 sensor mounted on the waveguide (WG).

Using those material properties, we can estimate the thermal bulk resistance for each of the three copper pieces used to thermalise the setup. Each copper piece has a cross section of about 15 mm x 5 mm and a length of 10 cm, which yields the values listed in Table 5.1 and plotted with orange markers in Fig. 5.5.

Since the setup only rests on the copper pieces, we also need to consider the thermal contact resistance of the copper-copper interfaces. Thermal contact resistance decreases approximately linearly with the applied force and increases with surface roughness [108]. This means that for a given surface, the achievable contact resistance is given by the applied force.

Comparing the gravitational force of about 60 N for our setup to the nominal preload force of a single stainless steel M3 screw of about 1.5 kN [109], we see that the thermal contact resistance is about 25 times larger in the case of the resting setup. Using these forces and assuming a surface roughness of about 1.6 µm, we can use the surface contact resistance measured in Ref. [108] to calculate the thermal contact resistances at room temperature given in Table 5.1.

With decreasing temperature, the thermal contact resistance also increases. For clean metal-metal contacts, the contact resistance typically scales as $\propto 1/T$. In the presence of oxide layers, thick enough to prevent electrons from passing, but still transparent to phonons, scaling with $\propto 1/T^2$ is typically observed. Note that even a slight exposure to air is usually sufficient to build oxide layers that lead to a scaling with $\propto 1/T^2$. [110]

In Refs. [110, 111], thermal contact resistances between different materials below ambient temperatures are reviewed. The thermal contact resistance of copper-copper interfaces at cryogenic temperatures has been measured in several experiments. However, the measurement results vary significantly and are difficult to compare, as information on surface preparation or the applied force is often not given. However, we can use the measurement results in Ref. [112] to estimate the thermal contact resistances at cryogenic temperatures, which is done in Table 5.1. The resulting values are plotted in Fig. 5.5, with dark and light blue markers for the respective contact forces of 60 N and 1.5 kN.

Comparing the thermal resistances in Fig. 5.5, we see that at room temperature, the bulk thermal resistance dominates over the contact resistance. This changes at lower temperatures. At 20 K the thermal contact resistance of the rigid connection using one properly tightened M3 screw (≈1.5 kN) is of the same order of magnitude as the bulk thermal conductivity, while the contact resistance of the setup resting on the copper pieces (≈60 N) already dominates the total thermal resistance. Due to the quadratic increase in thermal contact resistance, this gets even more pronounced at lower temperatures. Below 10 K, the thermal resistance is completely dominated by interfaces.

Looking at the measured temperatures for our setup in Fig. 5.4, we see that the main improvement in cooldown time is achieved above 1.5 K. At these temperatures, the additional thermal contact by resting the can on the copper pieces and annealing of the copper braids improves thermalisation. However, below 1.5 K, the temperature of the setup and the base plate still start to deviate. Considering our calculations, this is most likely due to the superlinear increase in thermal contact resistance.

This increase probably also affects the performance of the copper braids used, whose ends are pressed into solid copper pieces for screw mounting. Measurements of similar copper braids show that below 1.5 K, thermal resistance is primarily limited by the contact resistance of the pressed connection, as discussed in Ref. [113]. In this reference, a significant improvement was observed after electron beam welding of the connection.

To further improve thermalisation, we could reduce surface oxidation and roughness by polishing, chemical etching, or noble metal encapsulation. For example, improvements by more than one order of magnitude have been observed with gold plating [112].

T (K)	Bulk OFHC copper 15 x 5 mm, 10 cm	Contact 60 N copper-copper 1.6 µm roughness	Contact 1.5 kN copper-copper 1.6 µm roughness
300	3.3	$6.9 \cdot 10^{-1}$	$2.7 \cdot 10^{-2}$
20	$6.7 \cdot 10^{-1}$	6.5	$2.6 \cdot 10^{-1}$
10	1.1	$2.6 \cdot 10^{1}$	1.0
1	$1.1 \cdot 10^{1}$	$2.6 \cdot 10^{3}$	$1.0 \cdot 10^{2}$
0.1	$1.1 \cdot 10^{2}$	$2.6 \cdot 10^{5}$	$1.0 \cdot 10^{4}$

Tab. 5.1 Estimated thermal resistances (in K/W) for untreated, commercially available OFHC copper [107] and untreated copper–copper contacts with a surface roughness of 1.6 µm at different applied forces at room [108] and cryogenic temperatures [112]. Bulk values correspond to a copper piece with 15 x 5 mm cross section and 10 cm length.

A contact force of 60 N approximately represents the weight of our setup resting on the copper pieces, while 1.5 kN roughly corresponds to the preload force of a single M3 screw tightened to 1 Nm torque [109].

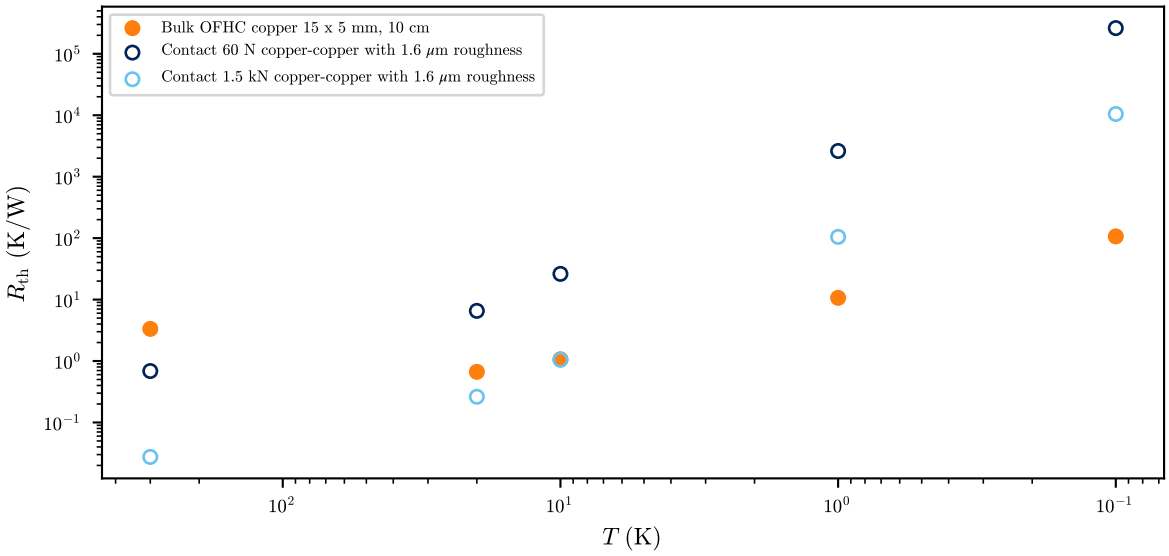

Fig. 5.5 Estimated thermal resistances listed in Table 5.1. At cryogenic temperatures, the total thermal resistance is increasingly dominated by contact interfaces.

5.1.2.2 Performance of the vibration isolation setup

While good thermalisation requires a rigid connection to the baseplate, effective isolation from vibrations needs mechanical decoupling. Ultimately, a compromise between optimal thermalisation and vibration isolation must be found.

With the current setup, the experiment is well isolated from vibrations. This becomes evident when comparing the measured tuning behaviour of one of the prepared optomechanical samples before and after suspending the setup, shown in Fig. 5.6. Before suspending the setup, the cantilever is highly excited due to vibrations of the pulse tube cooler. Besides the flux sweetspot, the cavity is barely visible. This significantly changes after suspending the setup, using the mechanical vacuum feedthrough. Here, a clear cavity response can be measured, even with the pulse tube cooler running. Further details are discussed in Section 5.3. For example, Fig. 5.12 compares data with running and stopped PT cooler.

Quantitative data demonstrating the setup's performance, like a measurement of the mechanical occupation with running and stopped pulse tube, can be found in the supplementary material of Ref. [9].

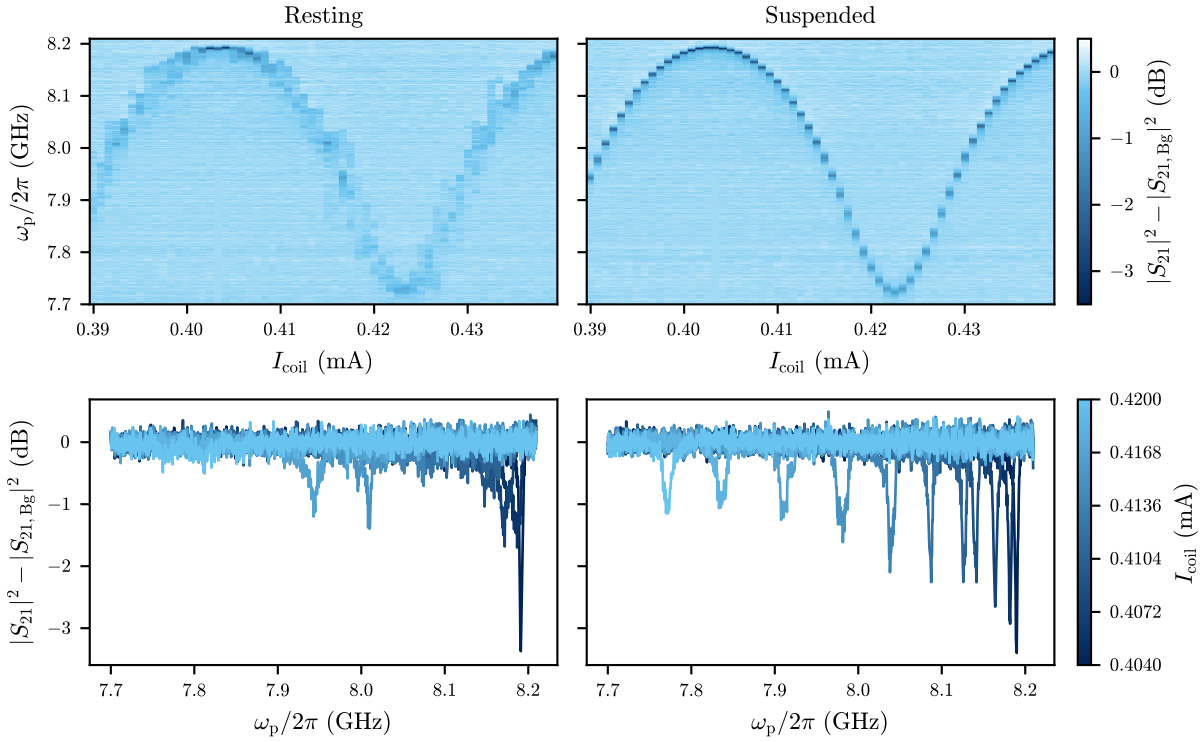

Fig. 5.6 Measured tuning behavior of cavity *WSQL9* with cantilever *C7* before and after suspending the setup. Both datasets were obtained while the PT cooler was on. Plots in the bottom row correspond to line cuts at different applied coil currents, showing that the cavity response is washed out by the cantilever motion at increasingly sensitive flux bias points. After suspending the setup, this effect gets significantly less pronounced, indicating a reduced mechanical occupation.

5.2 Effects of magnetic AFM cantilever on SQUID cavity

Before analysing measurements of the mechanical motion, we first discuss the effects that mounting a cantilever with an attached magnetic particle has on the SQUID cavity. Measurements of the cavity scattering parameter at different flux bias points, before and after mounting a magnetic cantilever, are shown in Fig. 5.7. As can be seen, after coupling the cavity to a cantilever, some of the prepared samples (in particular cavity *WSQL9* and *WSQL13*) show a resonance that is broadened and washed out by the magnetic field of the oscillating cantilever.

Besides this inherent sign of optomechanical coupling, the presence of the cantilever chip and the particle's static magnetic bias field also alter the cavity's intrinsic properties. Most notably, this results in a decrease in internal quality factor, which we will discuss in detail in Subsection 5.2.3, and changes in the cavity tuning behaviour, which we focus on in the following subsection.

5.2.1 Cavity tuning behaviour after mounting a magnetic AFM cantilever

As shown in Fig. 5.7, mounting a magnetic cantilever leads to several changes in the cavity tuning behaviour. These include a decrease in overall resonance frequency, reduced hysteresis and, in some samples, sinusoidal (e.g. *WSQL9*) or asymmetric tuning lobes (e.g. *WSQL13*).

The decrease in overall resonance frequency can be attributed to two main effects. First, the added dielectric of the cantilever chip increases the capacitance of the microstrip, thereby lowering the cavity frequency. Second, the in-plane component of the particle's magnetic field, normal to the tunnelling direction of Cooper pairs in the Josephson junctions, can lead to a reduction of the Junction critical current, which in turn increases their inductance (see Eq. (2.43)).

As explained in Section 2.3.1.1, the tuning period of the individual junction critical current is given by the relatively small area of the junction's oxide barrier. Estimating the effective area of the oxide barrier is challenging, as flux focusing and shielding effects of the superconducting aluminium and niobium films need to be considered. Using the simplified assumption that half of the superconducting film with a total thickness of about 600 nm (see Section 3.1.4) focuses the in plane field of the particle through the junction oxide barrier, we get an effective area of 300 nm x 3 µm. Assuming a dipole field and typical magnetic particle sizes, the corresponding in-plane magnetic field would result in a flux $\Phi_{\mathrm{j,ip}}$ of up to $2\Phi_0$. Hence, dependent on the distance between the particle and the SQUID, the critical current of the junctions might significantly change after the mounting of a cantilever.

This change in critical current not only leads to a shift of the overall cavity frequncy, but alos increases the SQUID participation ratio β_{r} (Eq. (2.57) and (2.50)) and reduces the shielding parameter β_{L} (Eq. (2.55)). As a result, the tuning behaviour becomes less hysteretic, which is evident for all samples except for *WSQ3*. As the cantilever chip for *WSQ3* had fallen off after warm up, we suspect the cantilever had already moved further away from the cavity during cooldown, resulting in a weak change in β_{L} and β_{r}.

Furthermore, different in-plane fields at the location of the two junctions can lead to different critical currents. This might explain the sinusoidal tuning behaviour of *WSQL9*, which shows an additional lower sweetspot, typical for an asymmetric SQUID [5, 57].

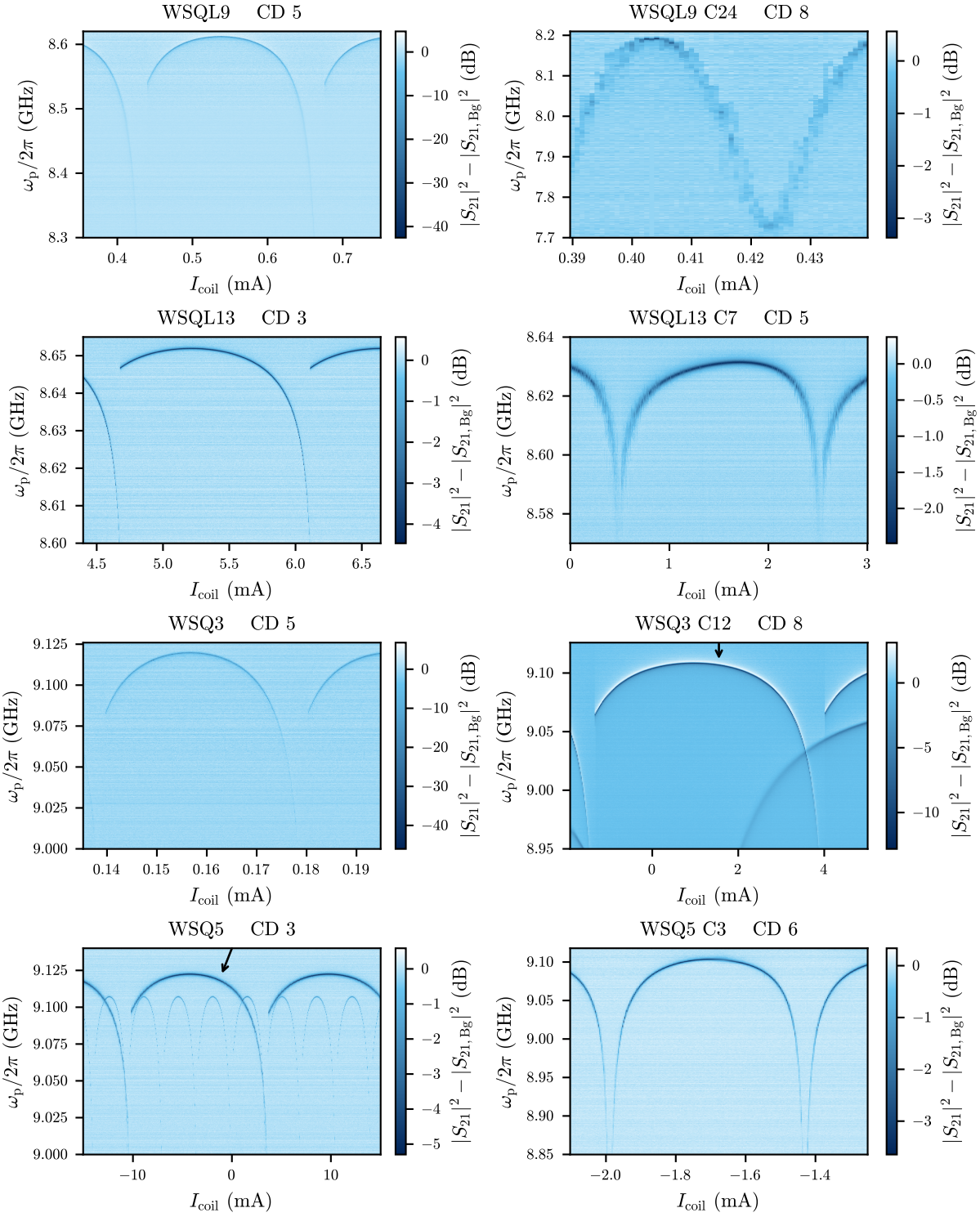

Fig. 5.7 Tuning behaviour with externally applied bias field of cavities before (left) and after (right) mounting a cantilever with magnetic particle. In datasets showing additional resonances from other cavities in the waveguide, the relevant one is marked with an arrow. As coil setup and sample positions changed between cooldowns, coil currents in individual subplots are not directly comparable. Note that the setup was not suspended, and the pulse tube cooler was turned on during the measurements that are shown here.

For cavity *WSQL13* and also less pronounced for *WSQ5*, we see that the individual tuning lobes after mounting a cantilever become asymmetric about the sweet spot. The right side of each periodic lobe has a different slope from the left side. Even though it is not entirely clear yet what causes this asymmetry, we suspect this might be related to a change in the cantilever's resting position.

When detuning the cavity from the sweetspot, a current builds up in the SQUID loop to ensure flux quantisation is still fulfilled. This loop current leads to a static force and hence to a deflection of the cantilever [5]. Depending on whether we tune down to the right or left side of the lobe, the loop current will either flow clockwise or anticlockwise. Therefore, the cantilever is pulled towards or pushed away from the SQUID. This in turn changes the flux threading the SQUID loop. To fulfil flux quantisation, the SQUID will react to this changed loop flux with a different loop current, which again will lead to a change in the resting position of the cantilever. This continues until the static force due to the loop current is in balance with the restoring force of the cantilever. Considering the magnetic field directions and the corresponding orientation of the force on the cantilever, this leads to an apparent reduction in the shielding parameter. However, up to the first order in the resting position, this does not lead to asymmetric lobes.

One aspect not yet considered is that the change in the cantilever's resting position might also affect the critical current of the Josephson junctions. Due to the area of the junction oxide barrier, which is small compared to the area of the SQUID loop, relatively large magnetic fields are required to induce a single flux quantum. However, after mounting the cantilever, the static magnetic field of the particle may bias the junction at a point where the critical current exhibits a steep dependence on the applied flux, i.e. where $\partial I_\mathrm{c}/\partial\Phi_\mathrm{j,ip}$ is large (see. Eq. (2.42)). In this case, even a small change on the order of a fraction of one Φ_0 through the junction could result in a significant change in the critical current. Thus, a change in the resting position of the cantilever might suffice to cause a significant change in critical current.

Including this change in critical current with resting position, we get different tuning behaviours on the left and right sides of the lobe. Depending on the sign of $\partial I_\mathrm{c}/\partial\Phi_\mathrm{j,ip}$, pulling the cantilever closer can either increase or decrease the critical current, while pushing it away has the opposite effect. A decrease in I_c increases the junction inductance, thereby lowering the cavity frequency. On the other side of the tuning lobe, an increase in I_c leads to a reduced inductance and thus a higher cavity frequency.

5.2.2 Change of cavity tuning behaviour with thermal cycling

As shown in Fig. 5.8, an asymmetric lobe (as seen during CD 5) is not the only feature observed for cavity *WSQL13* after mounting cantilever *C7*. Despite no changes being made to the prepared sample or the mounted cantilever, we observe substantially different tuning behaviours across different cooldowns.

The only changes between cooldowns involved slight variations in the cavity–waveguide coupling and rewinding the waveguide coils after CD 5. For the first two cooldowns, CD 4 and CD 5, the sample was placed in the same slot of the same waveguide, and the same coil was used to tune the magnetic field. The absolute change in current should therefore correspond to the same change in bias field, enabling a direct comparison of the flux tuning period. For CD 8, the sample was moved to another waveguide, which allows for stronger coupling to the sample.

Note that *WSQL13* was also cooled down during CD 7 using the same configuration as in CD 8, but due to a broken cable inside the fridge, proper measurements were not possible. Based on the weak and noisy signal that was still detectable, the tuning behaviour appeared similar to that observed during CD 5.

In Fig. 5.8 b), the tuning behaviours observed during the different cooldowns are overlaid by extracting the cavity frequency at each coil current and manually offsetting and rescaling the current axes to match the overall observed tuning period. The same scaling factor was used for the data from CD 4 and 5. As can be seen, for CDs 4, 6 and 8, additional dips in the tuning behaviour appear. These dips periodically repeat with the overall flux period, are not dependent on the direction of the magnetic field sweep and remain stable throughout each individual cooldown. For CDs 4 and 6 the tuning behaviour is very similar, with a dip at 0.6, while for CD 8 a dip at 0.2 appeared.

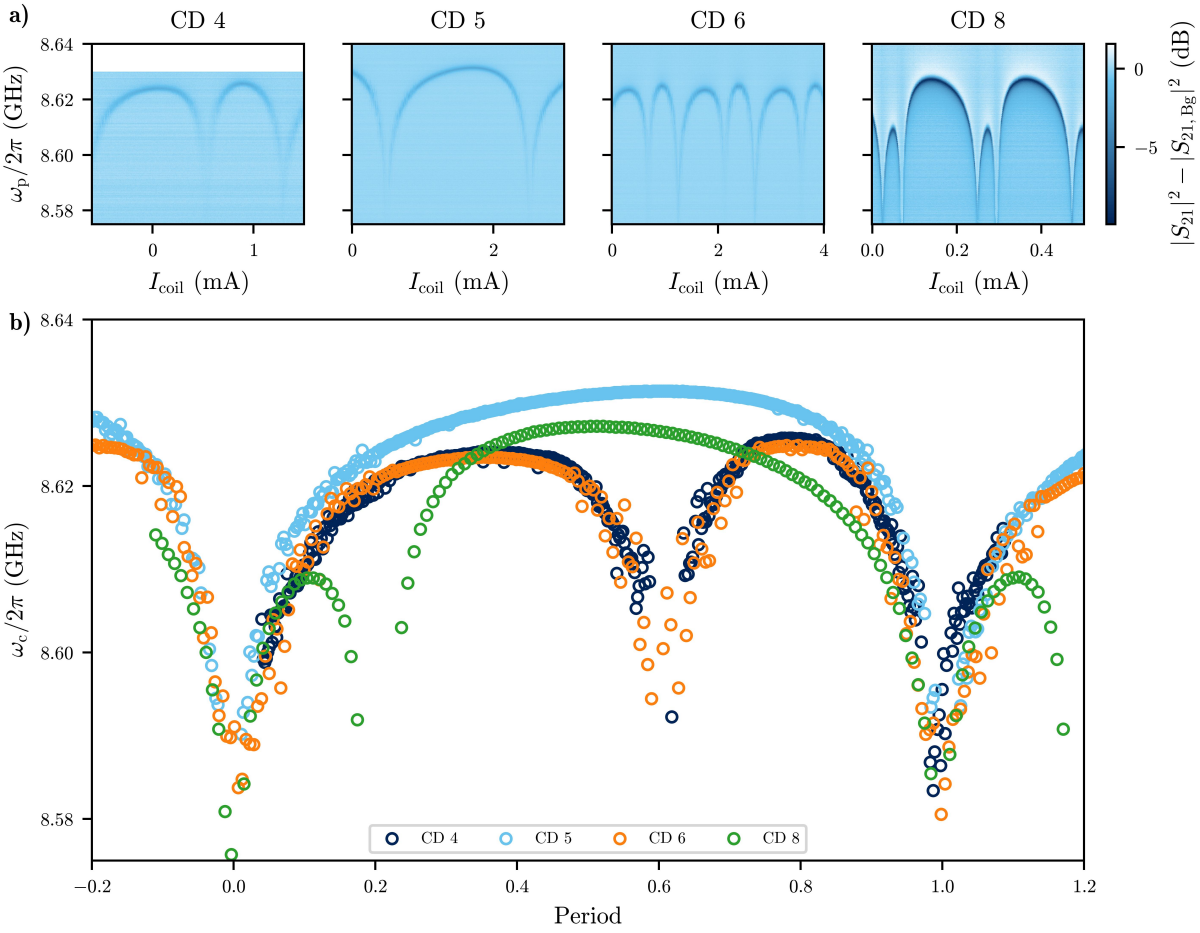

Fig. 5.8 **a)** Tuning behavior of WSQL13 after mounting cantilever C7 over subsequent cooldowns. For CD 4, 6 and 8, additional dips in resonance frequency appear, repeating periodically with the overall flux period. For CDs 4 and 5, identical coil setups and sample positions allow for direct comparison of coil current. **b)** Overlaid tuning behaviours across CDs, with coil current axes rescaled to match the overall tuning periods. For CD 4 and 5, with identical coil setup and sample position, the same scaling factor was used.

One possible explanation for the disappearance and reappearance of these dips involves low-temperature changes in the magnetisation of the NdFeB particle. At a temperature of about 130 K, NdFeB undergoes a spin reorientation transition, where the easy magnetisation direction changes from a single axis to a cone [114–117]. As the temperature decreases further below the transition, the cone's opening angle increases from 0° up to about 31°. Reorientation of the magnetisation to an axis on this cone might lead to different magnetisation directions between cooldowns, potentially altering the static bias field seen by the junctions.

If this bias field tunes the junction critical current close to a zero crossing of I_c, the change in resting position due to loop currents in the SQUID might be sufficient to drive the junction through zero critical current. This would significantly increase the junction inductance and, in turn, lead to the observed additional dip in cavity frequency. However, attempts to simulate this effect could not yet reproduce the observed behaviour.

Another possible explanation for a change in the bias field seen by the junctions might be a change in the cantilever's position due to thermal cycling of the sample. If the GE varnish used to fix the cantilever chip on the cavity was not fully cured, thermal cycling might cause a change in the position of the cantilever chip. However, this explanation seems less likely, as the observed dips in cavity frequency seem to appear or disappear entirely rather than evolve gradually. For example, CD 4 and CD 6 showed essentially the same tuning behaviour, while in between for CD 5, no additional dip was observed. This suggests a discrete rather than continuous effect, making a gradual shift of the cantilever chip position a less plausible explanation.

5.2.3 Cavity quality factor after mounting of a cantilever

As discussed in Section 2.1.2, a small cavity linewidth is crucial for efficient cooling of the mechanical mode. In Section 3.2.2, we showed that the characterised batch of SQUID cavities without a cantilever reaches internal quality factors up to $35{\cdot}10^3$. This would result in an optomechanical system close to the resolved sideband regime. However, after mounting a cantilever, we observe a significant reduction in the internal quality factor.

Figure 5.9 shows the internal quality factors of various SQUID cavities before (empty markers) and after (filled markers) mounting a cantilever. The cavities were tuned to first-order flux-insensitive bias points to minimise the influence of external flux noise and cantilever excitation. In all samples, we observe a clear reduction in the internal quality factor after mounting a cantilever with a magnetic particle. In the following, we will discuss possible origins of this added loss.

As mentioned in Section 2.5, exposing superconducting materials to magnetic fields increases the number of normal-conducting charge carriers. To expel the magnetic field via the Meißner effect, the binding energy of Cooper pairs is used to generate shielding currents [56]. This can lead to pair breaking and the generation of normal-conducting electrons, creating microwave loss. For type II superconductors such as niobium, magnetic fields exceeding the first critical field allow magnetic flux to penetrate the material in the form of vortices, before superconductivity ultimately breaks down at the second critical field [56]. Interaction of vortices with microwave fields has been shown to be a source of dissipation in superconducting cavities [63].

In high-purity bulk niobium, the first critical field is approximately 170 mT, while the second

critical field is around 400 mT [85]. This is slightly higher than the typical magnetic field generated by the particle, which is usually on the order of 10-100 mT at the SQUID (see Eq. (4.4)). In cavities made from thin niobium films, however, reduced internal quality factors due to flux vortices have already been observed at much lower fields [64]. To reduce such effects in future devices, patterning the niobium film with arrays of antidots has been demonstrated to substantially improve the quality factors of coplanar niobium cavities in magnetic fields [64].

In addition to magnetic effects, the NdFeB magnetic particle is a normal-conducting material in which eddy currents can be induced, potentially introducing further microwave loss [65].

Beyond the magnetic particle, the silicon cantilever chip itself can contribute to additional loss, for instance, through dielectric loss or two-level systems (TLSs) [62]. Usually, TLSs are predominantly located in native surface oxides. However, impurities, crystal defects and dopants can also lead to a major contribution of the bulk [118].

To distinguish between the loss mechanisms introduced by the magnetic particle and the silicon cantilever, we cooled down two samples with bare silicon cantilevers, i.e. without attached magnetic particles (half-filled markers in Fig. 5.9). We find that even mounting a bare cantilever significantly reduces the cavity quality factor. Since this reduction is much larger than expected for pure high-resistivity silicon, we contacted the manufacturer of the cantilever chips [93].

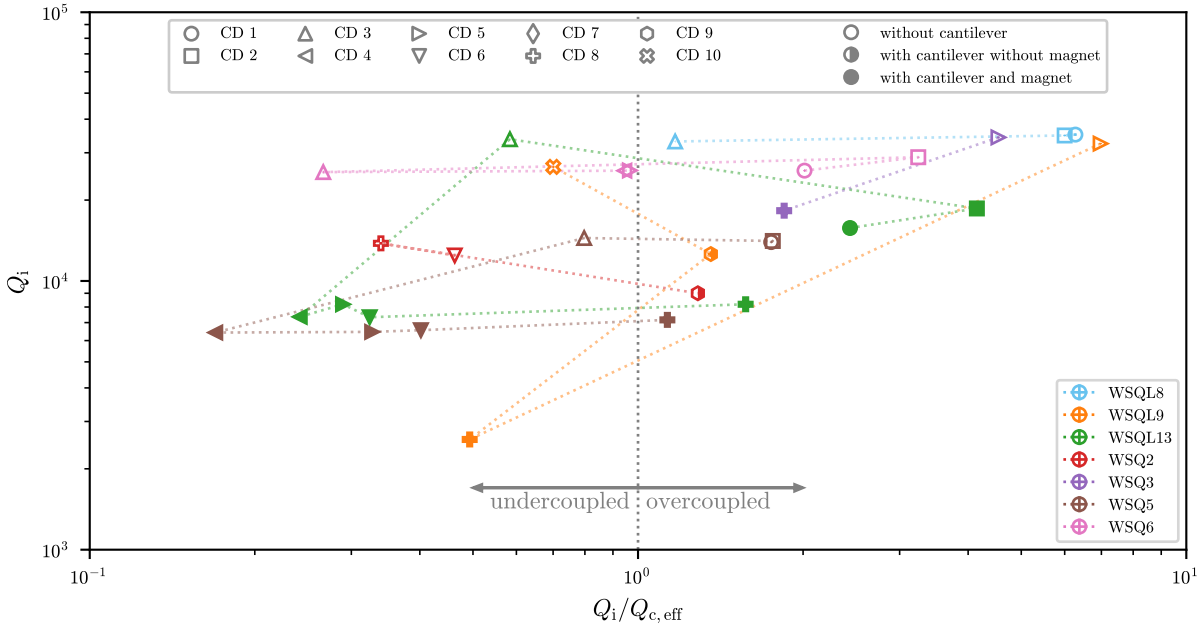

Fig. 5.9 Internal quality factors of various SQUID cavities before and after mounting a cantilever. Different markers represent different cooldowns, and markers belonging to the same sample are connected in the order of successive cooldowns. Empty markers indicate samples without a cantilever, half-filled markers represent samples with a cantilever but no magnet, and fully filled markers correspond to samples with a cantilever and magnet. Uncertainties of the fit are smaller than the marker size.

According to the manufacturer, the cantilevers are made from n-doped silicon with a room-temperature resistivity of only 0.01 Ωcm to prevent static charging during usually intended AFM operation. Considering that undoped, high-resistivity silicon has a room-temperature resistivity of approximately 10 kΩcm, and comparing this to reported microwave cavity losses on doped silicon substrates in Ref. [118], this explains the large additional loss introduced by the cantilever chip. It turns out that most commercially available silicon cantilevers are fabricated from heavily doped silicon to avoid static charging. To overcome this limitation, future optomechanical devices would require custom-fabricated cantilevers from undoped, high-resistivity silicon or other materials with low dielectric loss.

Adding a magnetic particle causes an additional reduction in quality factor in addition to that caused by the cantilever. Interestingly, no mechanical signal could be detected in any sample that maintained an internal quality factor above $10{\cdot}10^3$. This suggests that the magnetic field strength plays a significant role in limiting the cavity quality factor, as a reduced magnetisation of the particle might explain the weak optomechanical coupling.

To address these limitations, we are currently working on coupling the cantilever to the SQUID cavity via a flux transformer. In a flip-chip configuration, this would allow only the small changes in magnetic field associated with cantilever motion to be coupled to the SQUID cavity, while the static magnetic bias field could be significantly reduced by moving the cantilever further away. Increasing the distance would also mitigate the dielectric and conductive losses introduced by the cantilever chip. However, this comes at the cost of reduced optomechanical coupling, as parasitic inductances in the flux transformer loop will limit the flux transfer efficiency.

5.3 Measurement of mechanical sidebands

Even though the discussed limitations have not yet allowed us to prepare a sample in the sideband resolved regime, we were able to measure mechanical signatures on four out of five prepared optomechanical samples (two of them reusing the same SQUID cavity). As described in Section 5.1.1, we tune the cavity to a flux-sensitive spot and probe it with a coherent tone. When interacting with the cavity, this tone gets modulated by the cantilever's motion, creating sidebands that can be measured using a signal analyser.

In Fig. 5.10, sidebands measured on the optomechanical samples are shown. To confirm that these sidebands indeed originate from mechanical motion rather than other spurious noise, several verification steps were performed. Detuning the cavity leads to the disappearance of the peak, which rules out electrical noise sources such as switching power supplies in the laboratory. To exclude flux noise as a cause, we compare the spectra with those from a cavity without a cantilever in the same waveguide. Furthermore, additional mechanical excitation, such as turning on the pulse tube cooler or directly knocking on the cryostat, leads to a clear increase in the observed peak height when the setup is not suspended. As we will show later in Section 5.4, an even more definitive indicator of mechanical origin is the observation of backaction effects for *WSQL13*. Strongly probing the cavity blue detuned can help in the initial identification of the mechanical peak. For the spectra shown here, the cavity is weakly probed on resonance to avoid any influence of optomechanical backaction on the mechanical properties. Since the spectra are not calibrated, only the sideband's linewidth, frequency and shape are relevant here.

Cantilever *C12*, mounted on cavity *WSQ3*, was the only sample from which no mechanical sideband was observed. As discussed in Section 5.2, this is most likely due to the cantilever becoming misaligned during cooldown and ultimately falling off during warmup.

For the cantilever C5 that was initially mounted on WSQ5, a mechanical sideband could be observed at elevated temperatures or under additional mechanical excitation. This suggests a weak optomechanical coupling. For the subsequent cooldown, we replaced cantilever *C5* with *C3*. As can be seen, this cantilever has a significantly larger linewidth and frequency than the original cantilever. This can be explained by the relatively small (effective) mass of the magnetic particle (see Section 5.2.2). Despite the particle being smaller, we were able to measure a mechanical signal without additional mechanical or thermal excitation during this cooldown. In subsequent cooldowns of *WSQ5* with cantilever *C3*, no mechanical signal could be observed. As the cantilever was still in place after warmup, the reason for this remains unclear. One possible explanation under investigation is that the particle was demagnetised by stray magnetic fields.

After mounting cantilever *C24* on cavity *WSQL9*, we observe a clear mechanical signature. Similart to the signature measured for *C3* on *WSQ5* during CD 6, we see that the shape of the mechanical sideband slightly deviates from a Lorentzian. Similar mechanical peak shapes have been observed with the previous batch of SQUID cavities and are simulated in the appendix

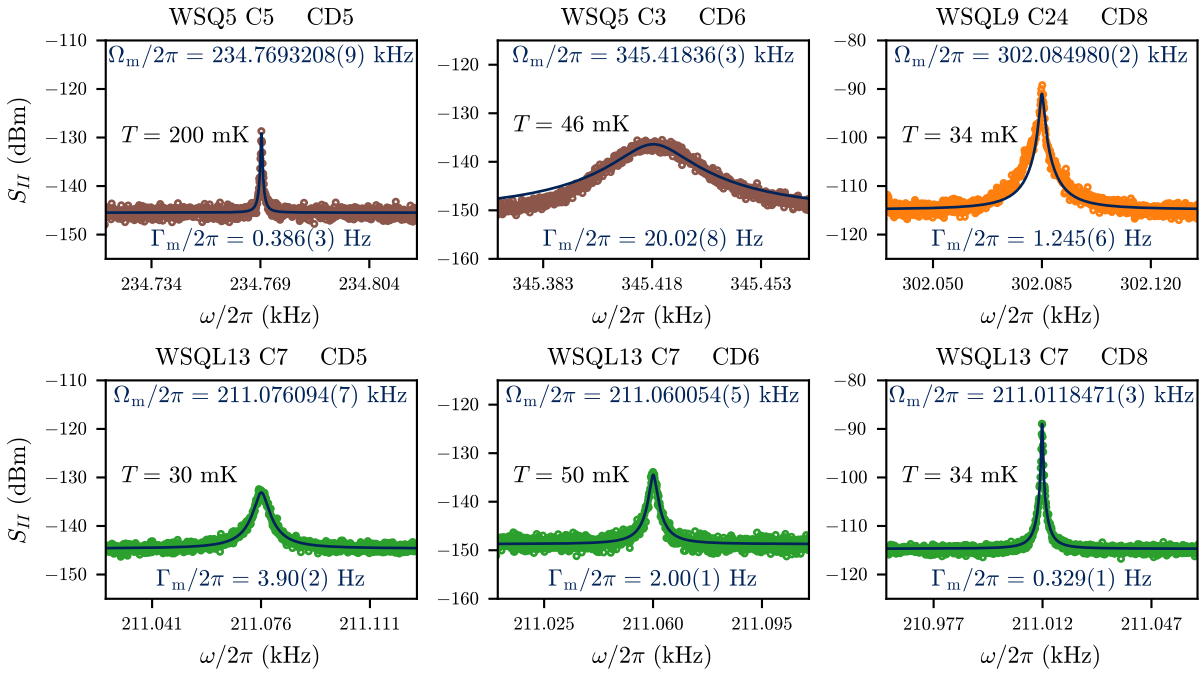

Fig. 5.10 Mechanical sidebands measured on four of the five prepared optomechanical samples. The dark blue lines show Lorentzian fits to the data. Varying levels of the noise floor for the different cooldowns are due to changes in the microwave output chain, like the absence of an additional room-temperature amplifier on the RF port of the IQ-mixer (see Fig. 5.1) or different SMA cables in the room temperature microwave setup. The given temperatures are measured with a RuO_2 sensor mounted on the waveguide.

of Ref. [7]. In this reference, Gaussian frequency fluctuations of the flux-tunable cavity under strong backaction were shown to lead to non-Lorentzian peak shapes. If the cavity frequency varies during the spectrum acquisition time (about 10 s for a spectral resolution of 0.1 Hz), the measured peak becomes an average over different cavity detunings. As optomechanical backaction varies the mechanical frequency and linewidth, this averaging distorts the lineshape. However, this should not be the case for the peaks shown here, as a rather weak probe tone was used. Notably, at higher cryostat temperatures ($\geq$ 100 mK) we observe that this asymmetry vanishes. Unfortunately, C24 had fallen off after warmup, and as already mentioned, no mechanical signature could be measured in the subsequent cooldowns of *WSQ5*. As a result, further investigation of the observed asymmetric resonance shape was not possible.

The most promising mechanical signature was observed for cavity *WSQL13* with cantilever *C7*. This sample survived several thermal cycles and shows a Lorentzian mechanical signature. The narrow linewidth gives a mechanical quality factor of up to $6.42(2)\cdot10^5$. As can be seen from Fig. 5.10, the mechanical properties change across subsequent cooldowns. Furthermore, we also observe relatively small changes in the mechanical properties at different flux bias points, which we will discuss in the following section.

5.3.1 Mechanical properties at different flux bias and after thermal cycling

Beyond the changes in cavity tuning behaviour of *WSQL13* with thermal cycling (discussed in Section 5.2.2), we also observe variations in the mechanical properties between different cooldowns.

As shown in Fig. 5.10, the mechanical linewidth and resonance frequency decrease with each thermal cycle. These changes appear gradual, in contrast to the more discrete changes in cavity tuning behaviour, suggesting that the two effects may not be correlated. As mentioned during the discussion on varying tuning behaviour, no modifications were made to the sample between cooldowns.

Possible effects that could explain the gradual change in mechanical properties could be the incomplete curing of the applied glue or local detachment from differential thermal contraction. In particular, changes in the stiffness of the Stycast droplet at the tip of the cantilever could influence the resonance frequency and mechanical quality factor.

As discussed in Chapter 4, after attaching a magnetic particle, we place the cantilever chip on a hot plate at 50 °C for at least 2 h to cure the Stycast. After mounting the cantilever chip to the SQUID cavity using GE varnish, we put the sample in a desiccator and let it dry in vacuum overnight. However, this may not fully remove the solvents from the applied glues. Once the sample is cooled, the low temperature prevents further curing, which leads to stable mechanical properties. But, warm phases between successive thermal cycles may allow for gradual solvent outgassing and slow continued curing. Besides incomplete curing, differential contraction during thermal cycling may lead to local detachment and stress relaxation of the applied glue, allowing the cantilever to bend more freely and thus modifying its mechanical properties.

We also observe changes in the mechanical properties with the flux bias point of the cavity. As can be seen from Fig. 5.11 and 5.12, these changes are rather small compared to the changes with thermal cycling. During each individual cooldown, these properties were stable.

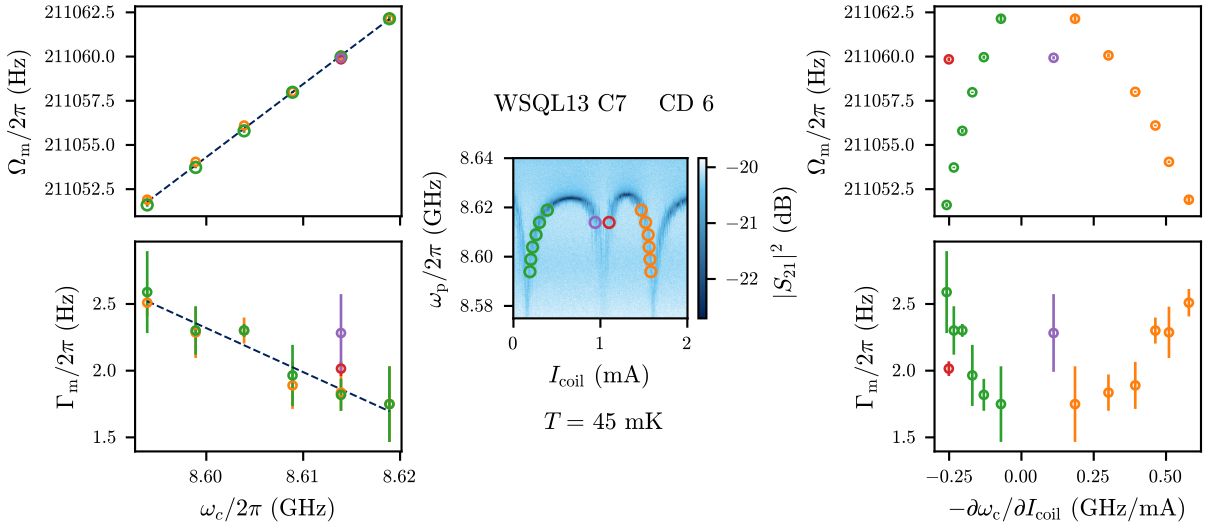

Fig. 5.11 Mechanical properties of cantilever *C7* at different flux bias points of cavity *WSQL13* during CD 6. To avoid backaction, the cavity is weakly probed on resonance. The dashed blue lines show linear fits of the data. The slope $\partial\omega_c/\partial I_{coil}$ is proportional to g_0 (see Eq. (2.91)).

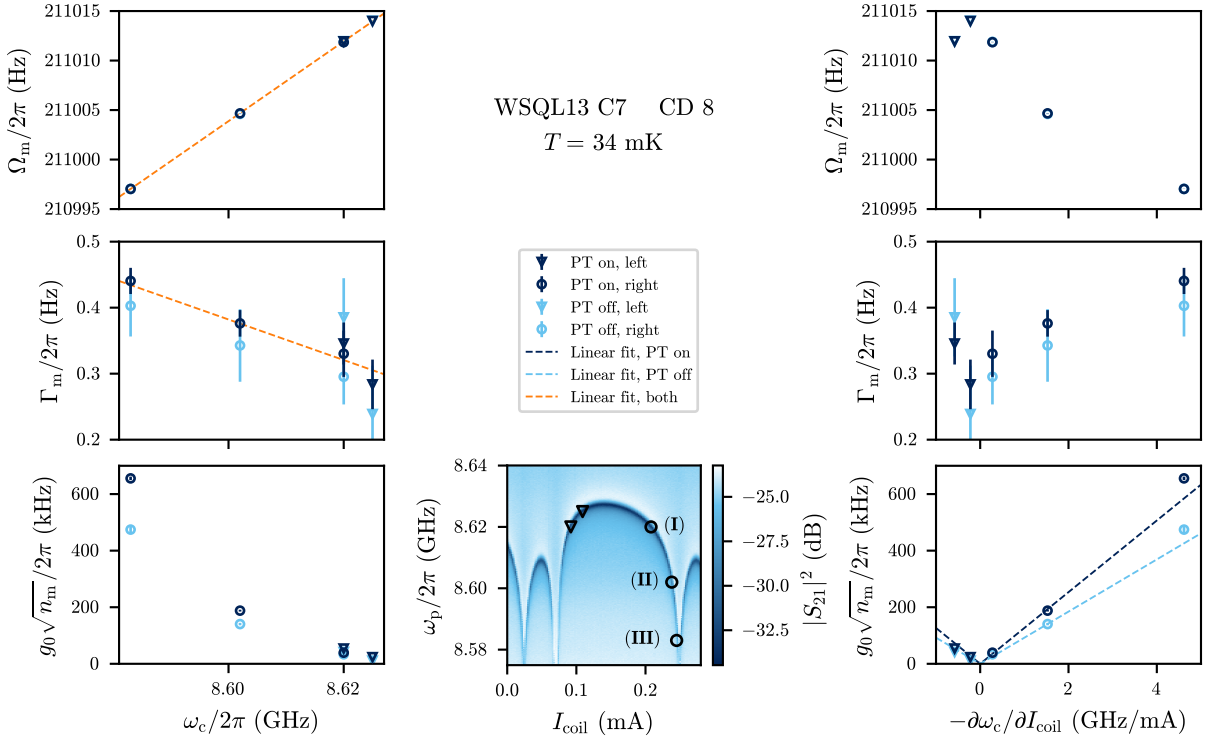

Fig. 5.12 Mechanical properties of cantilever *C7* at different flux bias points of cavity *WSQL13* during CD 8. To avoid backaction, the cavity is weakly probed on resonance. The setup was suspended during the measurement. Flux bias points marked with **(I)**, **(II)** and **(III)** are later used for cooling of the mechanical mode (see Fig. 5.15).

A closer look at the obtained data shows that the mechanical frequency changes linearly with the cavity frequency. This was also observed for samples using the previous batch of microwave cavities (see the supplementary of Ref. [6]). Initially, this shift was interpreted as a dispersive shift scaling with the optomechanical coupling. However, as visible on the right side in Fig. 5.11, the asymmetric tuning lobes of *WSQL13*, which exhibit different slopes and thus different optomechanical couplings at the same cavity frequency, show that the mechanical frequency shift cannot be directly attributed to variations in the optomechanical coupling. Instead, it appears that the mechanical frequency is more directly linked to the cavity frequency itself, which in turn is determined by the current circulating in the SQUID loop.

This observation is consistent with the interpretation presented in Refs. [5, 7], where the changes in the mechanical resonance frequency are explained by shifts in the cantilever's resting position due to magnetic forces generated by the SQUID loop current. The circulating current produces a magnetic gradient field, which alters the effective spring constant of the cantilever and thereby shifts the resonance frequency. Simulations of this effect can be found in the supplementary material of Ref. [7], where the mechanical frequency shift is simulated and plotted versus external flux. The simulation shows a roughly quadratic dependence on external flux. Since the cavity frequency scales approximately as the inverse square root of external flux (Eq. (2.59)), this leads to a linear dependence of mechanical frequency on cavity frequency, matching our experimental observations.

In addition to the mechanical frequency shift, there also seems to be a linear trend in the mechanical linewidth, which increases as the cavity frequency decreases. Since this increased linewidth does not directly correlate with the slope of the cavity tuning behaviour, it is unlikely that this broadening is caused by increased sensitivity to flux noise of the cavity. A possible explanation that would fit the observed trend is increased damping of the cantilever motion due to stronger magnetic field gradients generated by the circulating SQUID loop current. As the cantilever oscillates within this spatially varying magnetic field, eddy currents can be induced either in the normal-conducting magnetic particle or in the doped silicon cantilever. These eddy currents would dissipate energy and thus contribute to an increased mechanical linewidth at lower cavity frequencies.

As the data shown in Fig. 5.12 was obtained using the calibration method described in Section 5.1.1, the measured spectra allow us to determine $g_0\sqrt{n_\mathrm{m}}$ using Eq. (5.1). As can be seen from the data, $g_0\sqrt{n_\mathrm{m}}$ increases linearly with the slope of the cavity tuning behaviour. This is expected, as the optomechanical coupling strength is proportional to the flux sensitivity of the cavity (see Eq.(2.91)). This allows for tuning g_0 in situ with the applied magnetic flux bias.

Comparing the data obtained with running and stopped PT cooler (dark and light blue markers, respectively), we see that even with the suspended setup, vibrations of the PT cooler influence the mechanical occupation, though this influence is significantly reduced compared to the resting or rigidly connected setup. Without suspension and running PT cooler, the mechanical excitation is so strong that the cavity response is too washed out for meaningful operation of the system, even at moderate optomechanical couplings (see, for example, the response of *WSQL9* in Fig. 5.6). Notably, the ability to operate the suspended system with the PT on represents a substantial improvement, as measurement times were previously limited to the short periods during which the PT could be turned off.

5.3.2 Mechanical properties at different temperatures

To determine g_0, we increase the temperature of the setup using a PID-controlled heater on the cryostat's baseplate. As explained in Section 5.1.1.1, for a thermalised mechanical mode, the temperature-dependent occupation $\bar{n}_\mathrm{m}(T)$ should follow a Bose–Einstein distribution. This enables the extraction of g_0 by performing a linear fit to the product $g_0^2\bar{n}_\mathrm{m}(T)$.

However, as shown in Fig. 5.13 c), measuring $g_0^2\bar{n}_\mathrm{m}$ across different temperatures at the same cavity bias point, assuming constant g_0, shows that the mechanical occupation does not increase as expected with temperature. Instead, it stays constant or even tends to decrease with increasing temperature. This indicates that the mechanical mode is not thermalised to the temperature of the cryostat.

Slight deviations from the expected thermal occupation towards low temperatures have also been observed for samples from the previous batch of SQUID cavities. This is, for example, shown in the supplementary of Ref. [9]. Effects, such as a bottoming out of the thermal occupation, have also been reported for other optomechanical systems operating at millikelvin temperatures, for instance, capacitively coupled SiN resonators [38, 73]. A straightforward explanation in such cases is that the mechanical resonator does not fully thermalise to the cryostat temperature and instead remains at a higher temperature.

However, as can be seen from the data in Fig. 5.13 a) and b), in the case of *WSQL13*, changing the temperature of the setup leads to a change in the mechanical properties. While the mechanical frequency increases roughly linearly, the linewidth increases $\propto \sqrt{T}$. This scaling of the mechanical linewidth matches the behaviour of a micromechanical resonator at millikelvin temperatures observed in Ref. [119]. In this reference, the scaling with temperature is explained and modelled with a damping mechanism originating from tunnelling TLSs. Bending of the material brings TLSs residing in the mechanical structure out of equilibrium. This causes a relaxation process that leads to energy dissipation. Because the time constant of this relaxation process tends to decrease at higher temperatures, the mechanical damping rate increases with temperature. As the linewidth follows this predicted behaviour, we think that the cantilever chip is thermalised to the set temperature of the cryostat. So the higher mode temperature is most probably not caused by an elevated internal cantilever temperature.

This conclusion is further supported by the observation that the mechanical occupation does not just bottom out and remain constant, but even seems to increase towards lower temperatures. Such behaviour was also observed in measurements on previous batch samples with running PT and without vibration isolation [50]. Here, excessive mechanical excitation from the PT cooler led to a high mechanical occupation, which increased towards lower temperatures. This increase was attributed to the reduction in mechanical linewidth, which leads to a slower decay of externally driven excitations. However, for the measurements on the new batch sample presented here, the setup was suspended, and the remaining influence of the PT cooler (comparing PT on vs. off data) is not sufficient to explain the high temperature of the mode.

In the past, several setup improvements to reduce vibrational and electrical noise were made [50]. For instance, the helium lines were routed through a sandbox to prevent vibrations of the pumps from reaching the cryostat. Additionally, the lines were clamped to the ceiling with vibration-absorbing foam. To prevent electrical noise on the tuning coils from exciting the cantilever, the

DC filter box on top of the cryostat was properly shielded and grounded. Furthermore, custom-built π-type-lowpass steel powder filters for the DC lines were mounted on the baseplate. Just before the start of this thesis, the cryostat had to be moved to a different laboratory room. During the move, not every setup improvement was carried over. For example, the sandbox is currently not implemented, as it was thought to be obsolete after the implementation of the vibration isolation setup. The powder filters broke and have yet to be replaced.

To verify that the changed experimental environment still allows samples to thermalise, we cool down *WSQL13* together with a sample from the previous batch used in Refs. [7, 9]. In addition, we include a nominally identical sample prepared by O.-M. Tardif in Sherbrooke. The wafer with the samples for this thesis was ordered together with M. L. Juan's group at the University of Sherbrooke, and samples with nominally identical designs were shared between the two labs. The Sherbrooke sample was prepared using the same cantilever chip from *Budget Sensors* [93], and the only notable differences are the use of magnetic NdFeB powder from a different supplier and a slightly larger amount of GE varnish to mount the cantilever. Apart from that, the sample shows a similar sub-Hz mechanical linewidth and a relatively large mechanical resonance frequency of 316 kHz.

Cooling down these samples together in the same waveguide, we find that the mechanical mode of the Sherbrooke sample thermalises well, reaching a mode temperature of 35 mK. Also, for the previous batch sample, the mode temperature follows the cryostat temperature down to approximately 100 mK. At this temperature, it starts to deviate slightly, consistent with earlier observations [9]. In contrast, for *WSQL13*, the mechanical mode still does not thermalise. Note that an additional test with *WSQL13*, after applying more GE varnish to potentially improve thermalisation of the cantilever chip, led to the same result. Interestingly, the mechanical resonance frequencies are around 211 kHz for *WSQL13*, 287 kHz for the previous batch sample, and 316 kHz for the Sherbrooke sample. As this appears to correlate with the degree of thermalisation, increased electrical or vibrational noise at lower frequencies may excite the mechanical modes. To mitigate electrical noise, we plan to repair or rebuild the broken steel powder filters in the near future.

Despite the mechanical mode not being thermalised, we were still able to cool it via optomechanical backaction, as discussed in the next section.

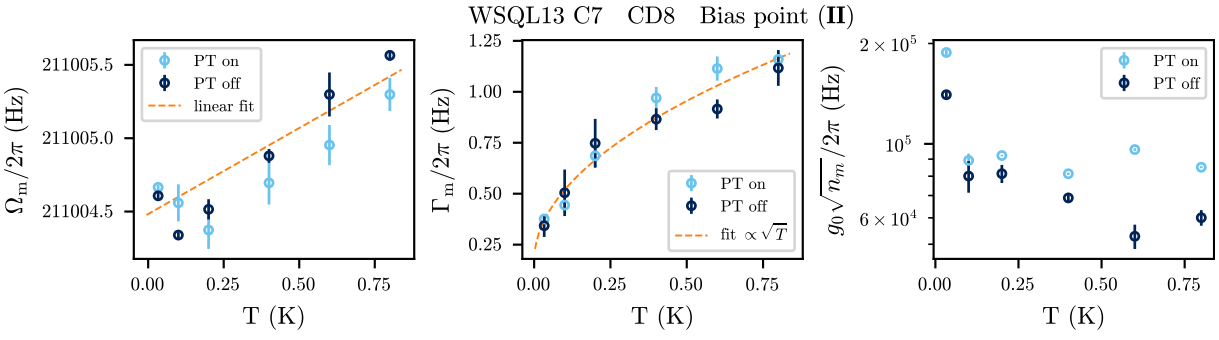

Fig. 5.13 Change of mechanical frequency, linewidth and occupation when ramping the temperature of the cryostat. While the frequency shows a linear trend and the linewidth matches the behaviour of a micromechanical resonator at mK temperatures observed in Ref. [119], $g_0\sqrt{n_\mathrm{m}}$ does not show the expected increase.

5.4 Cooling of the mechanical mode

For cooling of the mechanical mode, we use a strong probe tone. To find the point of optimal cooling, we measure the mechanical sideband at different detunings of the cavity and the probe.

To allow for calibration of the spectra, we apply a weak frequency modulation to the probe tone, as discussed in Section 5.1.1. For the measurements at flux bias points **(I)** and **(II)** (see Fig. 5.12), we use a peak frequency deviation of $\Delta\omega_\mathrm{p} = 30\,\mathrm{kHz}$ and a modulation frequency of $\Omega_\mathrm{mod} = \Omega_\mathrm{m} + 300\,\mathrm{Hz}$. With a mechanical frequency of about 211 kHz, this corresponds to a frequency modulation index of about 0.15, which is large enough for a calibration tone clearly above the noise floor, yet small enough to keep higher-order modulation sidebands well below it. Due to the broader cavity response at bias point **(III)**, a slightly larger peak frequency deviation of $\Delta\omega_\mathrm{p} = 37\,\mathrm{kHz}$ is used to ensure that the calibration peak remains clearly above the noise floor.

To avoid having to re-match the delay line at each detuning Δ, we keep the probe tone's carrier frequency fixed and instead tune the cavity frequency via the magnetic flux bias [7].

As discussed in Section 5.3.1, changing the flux bias point of the cavity tunes the optomechanical coupling strength g_0. Consequently, when varying the cavity frequency to find the optimal detuning to cool the mechanical mode, the area of the mechanical sideband varies even in the absence of optomechanical backaction. However, as the detuning for optimal cooling in the unresolved sideband regime lies within the range of a cavity linewidth (see Section 2.1.2), the cavity frequency is only varied over the range of a few MHz. Thus, the resulting change in g_0 is relatively small. To correct for this slight variation of g_0, we fit the cavity tuning behaviour locally around the chosen bias point with a polynomial and normalise the data using the slope of this fit.

Additionally, we showed that changing the flux bias slightly changes the mechanical properties (see Fig. 5.12). While the mechanical linewidth does not vary significantly over a cavity tuning range of a few MHz and thus requires no correction, the mechanical frequency does shift appreciably. To only obtain the mechanical frequency shift due to the optical spring effect $\delta\Omega_\mathrm{m}$ (Eq. (2.23) and (2.32)), we compare the mechanical frequency under backaction to low-power, backaction-free reference measurements taken at the same cavity frequency.

To ensure a stable cavity frequency and compensate for eventual slow drifts, we use an automated routine that uses the VNA to check the cavity frequency before and after each measurement of a mechanical spectrum [7]. If required, the cavity is retuned to the targeted frequency after measuring a group of five spectra. For each detuning, we measure four such groups, giving a total of 20 spectra per detuning. Each spectrum is measured with an $ENBW$ of 0.1 Hz to resolve the peak with sub-Hz linewidth, resulting in a measurement time of about 10 s per spectrum. We use a span of 800 Hz and take 8001 frequency points. To verify proper matching of the phase and delay, we also measure a spectrum with a completely detuned cavity, before and after each group. If the signal paths to the LO and RF ports of the mixer are properly matched, the calibration tone cancels and vanishes in the noise floor of the spectrum.

In the analysis of the data, the obtained cavity frequency right before starting a spectrum measurement is used to bin all 20 spectra into new groups of five spectra. Groups where the standard

deviation in cavity frequency exceeds 100 kHz are disregarded. The spectra within the remaining groups are then averaged and fitted with a Lorentzian to obtain the mechanical frequency and linewidth. To ensure the Lorentzian fit properly conveys the area of the mechanical peak, the averaged spectrum of each group is numerically integrated, and the resulting value is compared to the corresponding area of the Lorentzian fit. Groups for which the obtained areas differ by more than 25 % are excluded. Note that for the datasets presented in the following, more than 99 % of the groups fulfil the given criteria.

The measurement and analysis code for backaction measurements was written by D. Zopfel and later improved and adapted by L. F. Deeg. The same code was used in Refs. [7, 9], which give additional details on the measurement procedure and data treatment.

Fig. 5.14 shows the calibrated and averaged mechanical sideband at different detunings of the probe tone. As can be seen, red detuning the probe tone by about 1.5 MHz leads to a reduction of the mechanical sideband area. Furthermore, the mechanical linewidth increases and the mechanical frequency decreases. This is a clear indication of optomechanical backaction cooling and matches the expected behaviour discussed in Section 2.1.2.

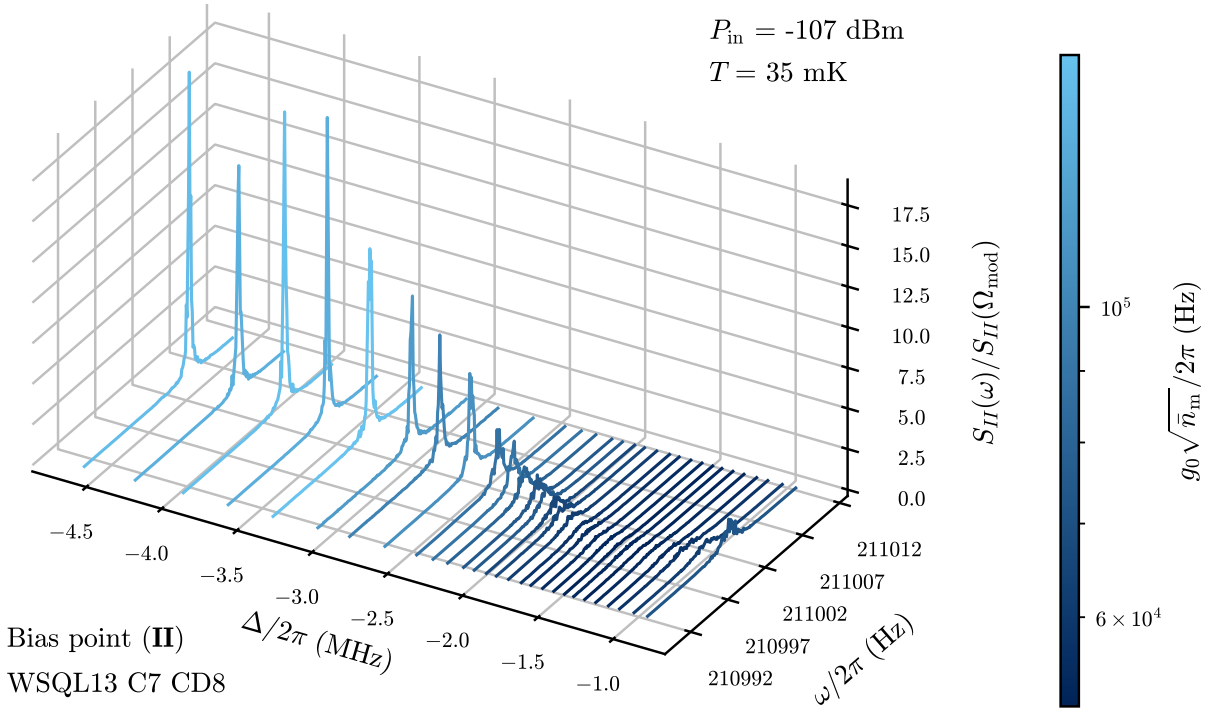

Fig. 5.14 Mechanical sideband measured on *WSQL13* with cantilever *C7* at different detunings of a strong probe tone. The spectra are divided by the height of the calibration tone to calibrate the data for the shape of the cavity resonance (see Section 5.3). Frequency axes of the individual spectra are corrected for the slight linear shift in mechanical frequency when changing the flux bias point of the cavity. More details on the treatment of the data are given in the main text.

Fig. 5.15 shows measured data on cooling and heating of the mechanical mode at three different cavity bias points. Different colors correspond to different powers of the probe tone.

As expected, for a red detuned probe tone, the mechanical linewidth increases due to optomechanically induced damping, while the optical spring effect leads to a reduction in the mechanical resonance frequency. The mechanical occupation, extracted from the area of the mechanical sideband, decreases. In contrast, for a blue detuned probe tone, both the mechanical occupation and resonance frequency increase, while the linewidth decreases. At detunings where the effective mechanical damping becomes negative, the system becomes unstable, and the mechanical occupation increases until it is limited by nonlinearities of the mechanical resonator.

Consistent with the simulated backaction traces presented in Section 2.1.3, increasing the probe tone power increases the photon-enhanced optomechanical coupling strength g and leads to stronger optomechanical backaction. Due to the Kerr shift of the cavity, the detuning for optimal cooling shifts to more negative values and the cooling feature becomes narrower.

Using the nonlinear cooling theory discussed in Section 2.1.3, we fit the observed shifts in mechanical frequency and linewidth. All traces with different probe tone powers at a given bias point are fitted simultaneously, using a single set of values for $\mathcal{K}$ and g_0. As can be seen, the theoretical model matches the experimental data well. The uncertainties of the extracted parameters are relatively large. This is primarily because the intracavity photon number is obtained from the input attenuation measured at room temperature and the output power of the signal generator, which leads to an estimated uncertainty of ± 1 dBm in the microwave power P_{in} reaching the sample.

An independent determination of g_0 from ramping the temperature of the setup is not possible, as the mechanical mode is not thermalised to the cryostat temperature. However, as can be seen in Fig. 5.16 a), comparing the obtained values for g_0 with the slope of the tuning behaviour, we find good agreement with the expected linear trend (Eq. (2.91)).

Compared to a sample using the previous batch of microwave cavities (measured g_0 of up to 7.5 kHz, see Ref. [7]), the values of g_0 obtained here are relatively small. This may be attributed to the limited frequency tuning range of cavity *WSQL13*, possibly caused by its relatively low SQUID participation ratio (see Fig. 3.8). However, compared to other optomechanical systems in the microwave regime, a single-photon coupling strength of 0.24(3) kHz is still considerable [38, 73].

Using the values of $\mathcal{K}$ and g_0 at each bias point, we fit all the mechanical occupation data to a common effective mode temperature using the nonlinear cooling model. As discussed in Section 5.3.2, the mechanical mode does not thermalise to the temperature of the cryostat, which was 35 mK during these measurements. From the fit, we extract an effective mode temperature of $T_{\mathrm{mode}} = 42(9)$ K, corresponding to a mechanical occupation of $\bar{n}_{\mathrm{m}} = 4.2(9) \cdot 10^6$ phonons, in contrast to the expected thermal occupation of about $\bar{n}_{\mathrm{th}} = 3456$ phonons. We suspect that this discrepancy is due to electrical noise on the tuning coils or an as-yet unidentified source of vibrational noise (other than the pulse tube cooler, which we could rule out as a major contribution for the suspended setup, see Fig. 5.12), which may excite the cantilever.

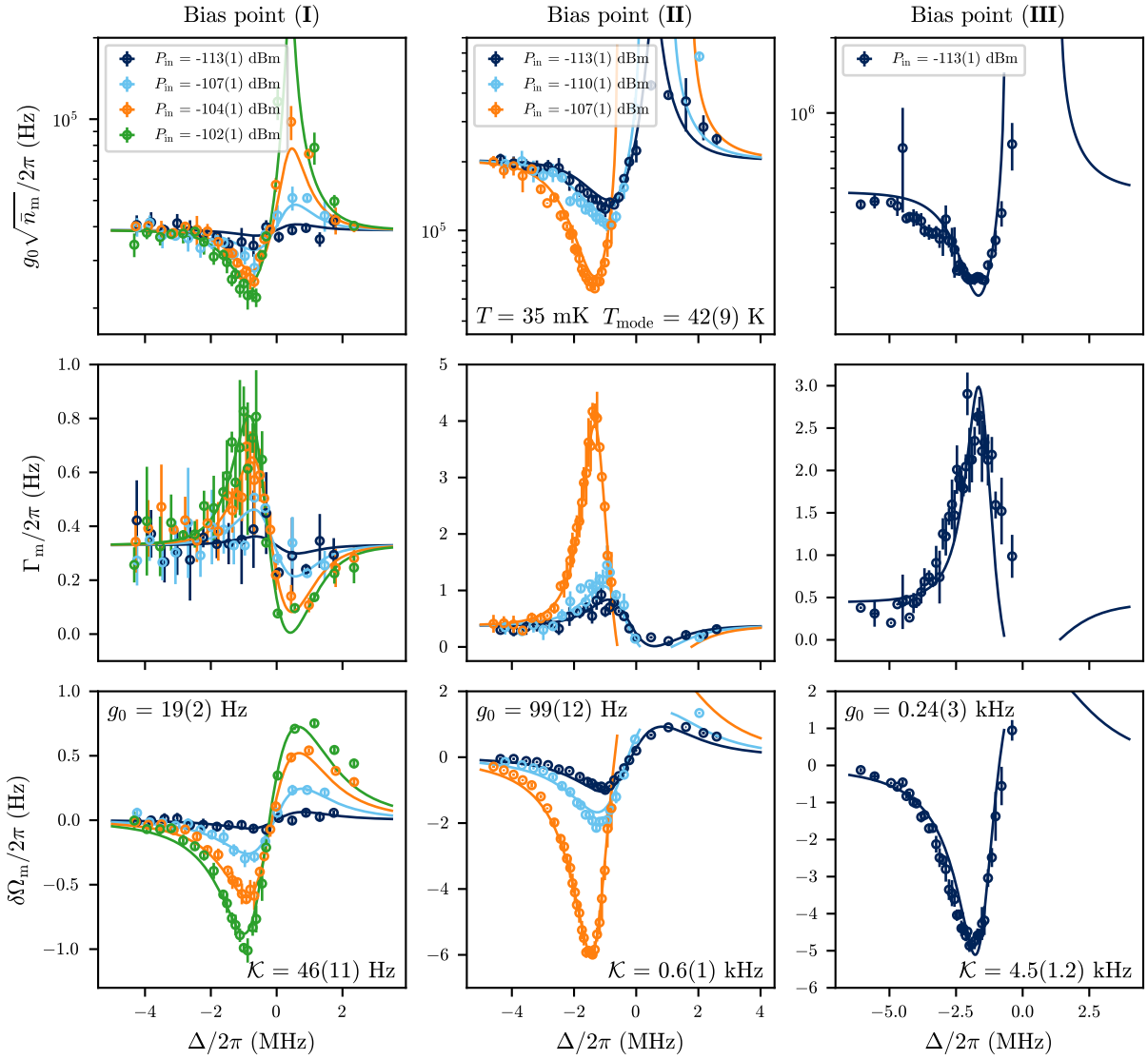

Fig. 5.15 Backaction cooling of cantilever C7 on cavity *WSQL13* at flux bias points **(I)**, **(II)** and **(III)** (see Fig. 5.12) for different powers of the probe tone. Error bars correspond to the standard deviation of repeated measurements. The solid lines show fits with the theoretical model discussed in Section 2.1.3. We first fit the mechanical frequency and linewidth at each bias point using the same g_0 and $\mathcal{K}$ for all probe tone powers. We then fix these parameters and fit all the obtained mechanical occupation data to one common effective mode temperature T_{mode}. Uncertainties of fit parameters correspond to the combined uncertainty of the fit and the systematic uncertainty of ± 1 dBm in P_{in}, whereby the systematic uncertainty dominates over the uncertainty of the fit.

In Fig. 5.16 b), the Kerr obtained from fitting the backaction traces is plotted against the detuning of the cavity from the flux sweetspot. For comparison, the plot also shows the Kerr obtained with the nonlinear circlefit before mounting the cantilever, initially shown for all characterised samples in Fig. 3.14. After mounting a cantilever, the additional feature in the tuning behaviour prevents us from obtaining Φ_{loop} using the derived model for a cavity without a mounted cantilever. We therefore plot $\mathcal{K}$ against the detuning from the individual sweetspot frequencies instead of loop flux. As can be seen, at the same detunings from the individual sweetspot frequencies, we find that mounting the cantilever does not change the Kerr constant.

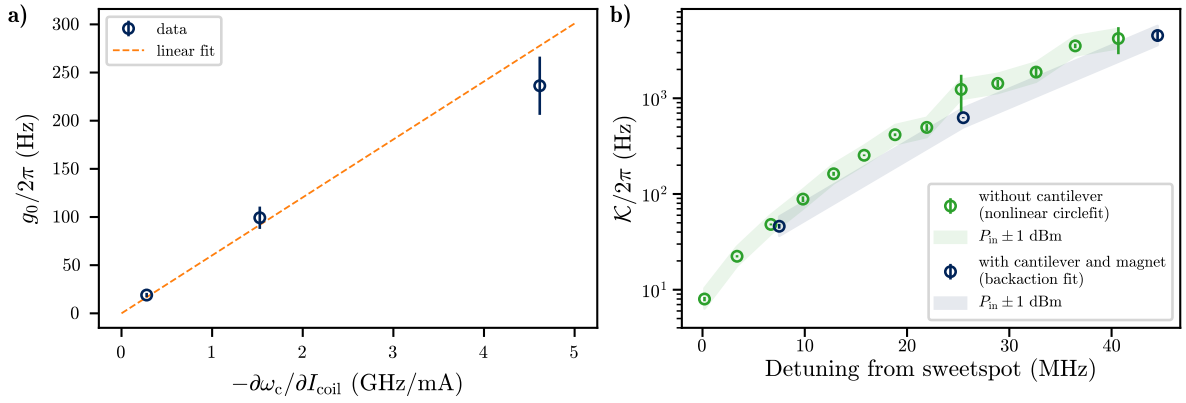

Fig. 5.16 **a)** single-photon coupling strength at different slopes of the cavity tuning behaviour, obtained from fitting the data in Fig. 5.15. **b)** Comparison of the Kerr constant of *WSQL13* at different detunings from the flux sweetspot, before and after mounting a magnetic particle.

CHAPTER 6

Conclusion and Outlook

In this work, we developed experimental and theoretical tools to characterise SQUID cavities for a magnetomechanical system. By analysing the hysteretic flux tuning behaviour, we were able to extract parameters such as the SQUID participation ratio and shielding parameter. Furthermore, we worked out a nonlinear circle fit routine to determine the Kerr nonlinearity from measurements of the cavity scattering parameter at different probe powers. With a simulation of the lumped element circuit model, we confirm the validity of the derived theoretical models for Kerr and the cavity tuning behaviour and examine the impact of the simplifying assumption of neglecting the junction capacitance. The derived models and worked-out tools should allow for quantitative comparison of SQUID cavities and will also be useful for future sample generations.

For the latest batch of StarCryo SQUID cavity samples characterised in this thesis, we find a substantial on-wafer spread in SQUID participation ratio, shielding parameter and Kerr nonlinearity. The obtained sample parameters did not show a clear correlation with the position of the individual samples on the wafer. To further investigate the reproducibility of the fabrication process, a comparison to samples from different fabrication runs would be of interest.

When comparing the experimentally obtained Kerr values at various flux bias points with the expected values from fitting the tuning behaviour, we find a reasonable agreement for most samples. The remaining discrepancies could be attributed to deviations of the actual input attenuation from the value measured at room temperature, and particularly for samples with higher SQUID participation ratios, to simplifications, such as neglecting the junction capacitance, in the theoretical model.

Using a waveguide that allows for tunable coupling to the cavities, we confirm that within the tested coupling range, the internal cavity quality factors obtained in our setup are not significantly affected by Fano interference. The latest batch of devices fabricated on high-resistivity

silicon wafer showed an up to fivefold improvement in internal quality factor compared to the previous batch. This improvement, while being a promising step towards reaching the sideband resolved regime, still appears to be limited by the insulating SiO_2 layer used in the junction fabrication process. An important observation in this regard is a drop in the internal quality factor with increased flux sensitivity. Here, further investigations are necessary to determine whether the reduction reflects an actual increase in internal loss (e.g., due to increased participation of lossy elements) or is only due to a broadening caused by flux noise, which could be mitigated through improved magnetic shielding or enhanced filtering of the tuning coils. Performing faster VNA scans or ringdown measurements should allow us to distinguish between those effects.

Using a custom-designed mounting stage, the preparation process of magnetomechanical samples could be substantially improved. Compared to the previous hand-mounting technique, where about every second cantilever was destroyed during the mounting process, the mounting stage increased the survival rate to essentially 100 %. Moreover, the enhanced precision and reproducibility of the cantilever placement achieved through this stage pave the way for more reliable and scalable sample preparation moving forward.

A process that still has room for optimisation is the preparation of cantilevers with magnetic particles. In particular, the selection of particles turned out to be challenging due to the large spread in grain size of the magnetic powder and the lack of a size reference under the optical microscope. In the future, we aim to increase the current yield, where only about one out of five prepared cantilevers has a suitably sized magnetic particle, by using the fabricated sapphire wafer with a patterned grid for size reference during particle selection. Further possible solutions would involve the use of a more homogeneous power or direct deposition of magnetic material.

After preselecting cantilevers with suitably sized magnetic particles based on optical microscope images, four out of five prepared samples showed a clear mechanical signature. In the future, extending the presented room-temperature cantilever characterisation in the AFM to all cantilevers would enable an additional, more quantitative assessment of particle size based on the observed frequency shift upon attaching a particle. Additionally, this might allow for more accurate predictions of the mechanical resonance frequency after cooldown.

Despite four mechanics samples showing a mechanical signature, variations with thermal cycling remain a challenge. While some cantilevers detached from the SQUID cavity, other samples appeared visually unchanged, yet exhibited substantially different tuning behaviour or mechanical properties for subsequent cooldowns. The origin of these variations is not yet fully understood. However, literature research suggests that a spin reorientation transition of the magnetic particle could alter the magnetisation and/or its direction. Additionally, incomplete curing of the glue used in mounting the particle or thermally induced changes, such as local detachment due to differential thermal contraction, might contribute to the observed effects.

Different cavity parameters, even before mounting a cantilever, complicate a systematic comparison of the changes in tuning behaviour introduced by the mounted cantilevers. However, common effects such as a reduced overall cavity frequency and a reduction in the SQUID shielding parameter were observed across all samples. These changes may be explained by the dielectric of the cantilever chip and a reduction of the junction critical current due to the in-plane magnetic bias field of the particle. To gain a deeper understanding of those effects, further investigations

will be carried out. For instance, performing in-situ magnetisation of the initially unmagnetised particle at cryogenic temperatures might help isolate the influence of the particle's magnetic field. Additionally, measuring the behaviour of bare SQUID cavities under externally applied high magnetic fields could provide insight into whether the observed changes are related to the magnetic field of the particle or the cantilever chip.

Performing such magnetic field tests might also help to clarify the role of the particle's magnetic field in the reduction of the internal quality factor. After mounting a cantilever with a magnetic particle, all samples showed a significant drop in internal quality factor. Additional tests with bare cantilevers and subsequent contact with the manufacturer revealed that the cantilevers are made from highly doped silicon, which itself contributes significantly to microwave loss.

With the implementation of a mechanical feedthrough, cycling the cryostat with the vibration isolation setup could be made faster. Based on literature research and temperature measurements of the setup over time, we identified oxidised copper surfaces and the pressed end-contacts of the copper braids as the remaining limiting factors for the thermalisation of the suspended setup. Possible solutions, such as (e-beam) welding of the braids to the solid copper end contacts, as well as polishing and/or gold coating of contact interfaces, will be tested. Hopefully, implementing these additional improvements will allow similar cooldown times as with a rigidly connected setup. Besides the improved thermalisation, the feedthrough also allows for an in situ evaluation of the performance of the vibration isolation setup.

Despite the implementation of vibration isolation, we observed an elevated mechanical mode temperature. Because the mechanical linewidth and frequency showed the expected behaviour when varying the temperature of the setup, we conclude that the increased mode temperature is not due to an elevated internal temperature of the cantilever chip. As higher-frequency cantilevers appear to thermalise better, the increased mode temperature is potentially due to low-frequency noise. It is not yet clear whether this noise is of electrical or vibrational origin. However, for the suspended setup, the pulse tube cooler could be ruled out as the main source, as turning it off did not lead to a substantial reduction in mechanical occupation. Reimplementing the cryogenic DC-filters or the sandbox to dampen vibrations of the gas lines to and from the cryostat, as existed at the previous location of the experimental setup, might be a solution.

Regardless of the high mode temperature, we demonstrated backaction cooling on one of the new samples with a single-photon coupling strength of up to 0.24(3) kHz. While the drop in internal quality factor after mounting a cantilever still prevented us from preparing samples in the sideband resolved regime and ground state cooling of the mechanical mode, the progress made in sample preparation and the identification of the main contributions to loss mark an important step towards a resolved system.

Reaching the sideband resolved regime will most likely necessitate separating the magnetic cantilever from the microwave cavity via a flux transformer. With recent progress in in-house fabricated SQUID cavities that reach intrinsic quality factors above 10^5, we are confident that a resolved system can soon be prepared. As an alternative to combining high-Q SQUID cavities with a flux transformer, we also pursue an approach based on hybridisation between the low-Q optomechanical system and the high-Q mode of an additional cavity [120, 121]. This could yield an effectively resolved system and ultimately enable access to the macroscopic quantum regime.

Bibliography

1. Via, G., Kirchmair, G. & Romero-Isart, O. Strong Single-Photon Coupling in Superconducting Quantum Magnetomechanics. *Physical Review Letters* **114,** 143602. https://www.doi.org/10.1103/PhysRevLett.114.143602 (2015).
2. Usenko, O., Vinante, A., Wijts, G. & Oosterkamp, T. H. A superconducting quantum interference device based read-out of a subattonewton force sensor operating at millikelvin temperatures. *Applied Physics Letters* **98,** 133105. https://www.doi.org/10.1063/1.3570628 (2011).
3. Vinante, A. & Falferi, P. Feedback-Enhanced Parametric Squeezing of Mechanical Motion. *Physical Review Letters* **111,** 207203. https://www.doi.org/10.1103/PhysRevLett.111.207203 (2013).
4. Vinante, A. Superconducting inductive displacement detection of a microcantilever. *Applied Physics Letters* **105,** 032602. https://www.doi.org/10.1063/1.4891173 (2014).
5. Schneider, C. M. F. *Magnetic coupling between superconducting circuits and a cantilever* PhD thesis (Unversität Innsbruck, 2021). https://diglib.uibk.ac.at/urn:nbn:at:at-ubi:1-85331.
6. Zoepfl, D., Juan, M. L., Schneider, C. M. F. & Kirchmair, G. Single-Photon Cooling in Microwave Magnetomechanics. *Physical Review Letters* **125,** 023601. https://www.doi.org/10.1103/PhysRevLett.125.023601 (2020).
7. Zoepfl, D. *et al.* Kerr Enhanced Backaction Cooling in Magnetomechanics. *Physical Review Letters* **130,** 033601. https://www.doi.org/10.1103/PhysRevLett.130.033601 (2023).
8. Diaz-Naufal, N. *et al.* Kerr-enhanced optomechanical cooling in the unresolved-sideband regime. *Physical Review A* **111,** 053505. https://www.doi.org/10.1103/PhysRevA.111.053505 (2025).
9. Deeg, L. F. *et al.* Optomechanical backaction in the bistable regime. *Physical Review Applied* **23,** 014082. https://www.doi.org/10.1103/PhysRevApplied.23.014082 (2025).
10. Aspelmeyer, M., Kippenberg, T. J. & Marquardt, F. Cavity optomechanics. *Reviews of Modern Physics* **86,** 1391–1452. https://www.doi.org/10.1103/RevModPhys.86.1391 (2014).
11. Heisenberg, W. Über quantentheoretische Umdeutung kinematischer und mechanischer Beziehungen. *Zeitschrift für Physik* **33,** 879–893. https://www.doi.org/10.1007/BF01328377 (1925).

12. A year to celebrate quantum physics. *Nature Reviews Physics* **7,** 1–1. https://www.doi.org/10.1038/s42254-024-00800-6 (2025).
13. Zurek, W. H. Decoherence, einselection, and the quantum origins of the classical. *Reviews of Modern Physics* **75,** 715–775. https://www.doi.org/10.1103/RevModPhys.75.715 (2003).
14. Schrödinger, E. Die gegenwärtige Situation in der Quantenmechanik. *Naturwissenschaften* **23,** 807–812. https://www.doi.org/10.1007/BF01491891 (1935).
15. Arndt, M. & Hornberger, K. Testing the limits of quantum mechanical superpositions. *Nature Physics* **10,** 271–277. https://www.doi.org/10.1038/nphys2863 (2014).
16. Schlosshauer, M. Decoherence, the measurement problem, and interpretations of quantum mechanics. *Reviews of Modern Physics* **76,** 1267–1305. https://www.doi.org/10.1103/RevModPhys.76.1267 (2005).
17. Monroe, C., Meekhof, D. M., King, B. E., Itano, W. M. & Wineland, D. J. Demonstration of a Fundamental Quantum Logic Gate. *Physical Review Letters* **75,** 4714–4717. https://www.doi.org/10.1103/PhysRevLett.75.4714 (1995).
18. Arndt, M. *et al.* Wave–particle duality of C60 molecules. *Nature* **401,** 680–682. https://www.doi.org/10.1038/44348 (1999).
19. Anderson, M. H., Ensher, J. R., Matthews, M. R., Wieman, C. E. & Cornell, E. A. Observation of Bose-Einstein Condensation in a Dilute Atomic Vapor. *Science* **269,** 198–201. https://www.doi.org/10.1126/science.269.5221.198 (1995).
20. Jaklevic, R. C., Lambe, J., Silver, A. H. & Mercereau, J. E. Quantum Interference Effects in Josephson Tunneling. *Physical Review Letters* **12,** 159–160. https://www.doi.org/10.1103/PhysRevLett.12.159 (1964).
21. Nakamura, Y., Pashkin, Y. A. & Tsai, J. S. Coherent control of macroscopic quantum states in a single-Cooper-pair box. *Nature* **398,** 786–788. https://www.doi.org/10.1038/19718 (1999).
22. Hammerer, K. *et al. Nonclassical States of Light and Mechanics* 2012. https://www.doi.org/10.48550/arXiv.1211.2594.
23. Degen, C. L., Reinhard, F. & Cappellaro, P. Quantum sensing. *Reviews of Modern Physics* **89,** 035002. https://www.doi.org/10.1103/RevModPhys.89.035002 (2017).
24. Yang, I., Agrenius, T., Usova, V., Romero-Isart, O. & Kirchmair, G. Hot Schrödinger cat states. *Science Advances* **11,** eadr4492. https://www.doi.org/10.1126/sciadv.adr4492 (2025).
25. O'Connell, A. D. *et al.* Quantum ground state and single-phonon control of a mechanical resonator. *Nature* **464,** 697–703. https://www.doi.org/10.1038/nature08967 (2010).
26. Wilson-Rae, I., Nooshi, N., Zwerger, W. & Kippenberg, T. J. Theory of Ground State Cooling of a Mechanical Oscillator Using Dynamical Backaction. *Physical Review Letters* **99,** 093901. https://www.doi.org/10.1103/PhysRevLett.99.093901 (2007).
27. Metzger, C. H. & Karrai, K. Cavity cooling of a microlever. *Nature* **432,** 1002–1005. https://www.doi.org/10.1038/nature03118 (2004).
28. Mancini, S., Vitali, D. & Tombesi, P. Optomechanical Cooling of a Macroscopic Oscillator by Homodyne Feedback. *Physical Review Letters* **80,** 688–691. https://www.doi.org/10.1103/PhysRevLett.80.688 (1998).

29. Cohadon, P. F., Heidmann, A. & Pinard, M. Cooling of a Mirror by Radiation Pressure. *Physical Review Letters* **83,** 3174–3177. https://www.doi.org/10.1103/PhysRevLett.83.3174 (1999).

30. Teufel, J. D. *et al.* Sideband cooling of micromechanical motion to the quantum ground state. *Nature* **475,** 359–363. https://www.doi.org/10.1038/nature10261 (2011).

31. Chan, J. *et al.* Laser cooling of a nanomechanical oscillator into its quantum ground state. *Nature* **478,** 89–92. https://www.doi.org/10.1038/nature10461 (2011).

32. Delić, U. *et al.* Cooling of a levitated nanoparticle to the motional quantum ground state. *Science* **367,** 892–895. https://www.doi.org/10.1126/science.aba3993 (2020).

33. Marquardt, F., Chen, J. P., Clerk, A. A. & Girvin, S. M. Quantum Theory of Cavity-Assisted Sideband Cooling of Mechanical Motion. *Physical Review Letters* **99,** 093902. https://www.doi.org/10.1103/PhysRevLett.99.093902 (2007).

34. Stannigel, K. *et al.* Optomechanical Quantum Information Processing with Photons and Phonons. *Physical Review Letters* **109,** 013603. https://www.doi.org/10.1103/PhysRevLett.109.013603 (2012).

35. Gröblacher, S., Hammerer, K., Vanner, M. R. & Aspelmeyer, M. Observation of strong coupling between a micromechanical resonator and an optical cavity field. *Nature* **460,** 724–727. https://www.doi.org/10.1038/nature08171 (2009).

36. Teufel, J. D. *et al.* Circuit cavity electromechanics in the strong-coupling regime. *Nature* **471,** 204–208. https://www.doi.org/10.1038/nature09898 (2011).

37. Verhagen, E., Deléglise, S., Weis, S., Schliesser, A. & Kippenberg, T. J. Quantum-coherent coupling of a mechanical oscillator to an optical cavity mode. *Nature* **482,** 63–67. https://www.doi.org/10.1038/nature10787 (2012).

38. Seis, Y. *et al.* Ground state cooling of an ultracoherent electromechanical system. *Nature Communications* **13,** 1507. https://www.doi.org/10.1038/s41467-022-29115-9 (2022).

39. Bowen, W. P. & Milburn, G. J. *Quantum Optomechanics* ISBN: 978-1-4822-5915-5 (Taylor & Francis, 2015).

40. Katz, I., Lifshitz, R., Retzker, A. & Straub, R. Classical to quantum transition of a driven nonlinear nanomechanical resonator. *New Journal of Physics* **10,** 125023. https://www.doi.org/10.1088/1367-2630/10/12/125023 (2008).

41. Palomaki, T. A., Harlow, J. W., Teufel, J. D., Simmonds, R. W. & Lehnert, K. W. *State Transfer Between a Mechanical Oscillator and Microwave Fields in the Quantum Regime* 2012. https://arxiv.org/abs/1206.5562v1.

42. Liao, J.-Q. & Law, C. K. Parametric generation of quadrature squeezing of mirrors in cavity optomechanics. *Physical Review A* **83,** 033820. https://www.doi.org/10.1103/PhysRevA.83.033820 (2011).

43. Rugar, D. & Grütter, P. Mechanical parametric amplification and thermomechanical noise squeezing. *Physical Review Letters* **67,** 699–702. https://www.doi.org/10.1103/PhysRevLett.67.699 (1991).

44. Wollman, E. E. *et al.* Quantum squeezing of motion in a mechanical resonator. *Science* **349,** 952–955. https://www.doi.org/10.1126/science.aac5138 (2015).

45. Khalil, M. S., Stoutimore, M. J. A., Wellstood, F. C. & Osborn, K. D. An analysis method for asymmetric resonator transmission applied to superconducting devices. *Journal of Applied Physics* **111,** 054510. https://www.doi.org/10.1063/1.3692073 (2012).

46. Vogel, M., Mooser, C., Karrai, K. & Warburton, R. J. Optically tunable mechanics of microlevers. *Applied Physics Letters* **83,** 1337–1339. https://www.doi.org/10.1063/1.1600513 (2003).

47. Peterson, R. W. *et al.* Laser Cooling of a Micromechanical Membrane to the Quantum Backaction Limit. *Physical Review Letters* **116,** 063601. https://www.doi.org/10.1103/PhysRevLett.116.063601 (2016).

48. Clark, J. B., Lecocq, F., Simmonds, R. W., Aumentado, J. & Teufel, J. D. Sideband cooling beyond the quantum backaction limit with squeezed light. *Nature* **541,** 191–195. https://www.doi.org/10.1038/nature20604 (2017).

49. Diaz-Naufal, N. *Kerr-enhanced optomechanics* PhD thesis (KIT, 2024). https://doi.org/10.5445/IR/1000180879.

50. Zöpfl, D. *Demonstration of nonlinear enhanced backaction cooling in microwave magnetomechanics* PhD thesis (University of Innsbruck, 2022). https://diglib.uibk.ac.at/urn/urn:nbn:at:at-ubi:1-116886.

51. Zöpfl, D. *Characterisation of stripline resonators in a waveguide* MA thesis (Innsbruck, 2017). https://diglib.uibk.ac.at/urn:nbn:at:at-ubi:1-6766.

52. Zoepfl, D. *et al.* Characterization of low loss microstrip resonators as a building block for circuit QED in a 3D waveguide. *AIP Advances* **7,** 085118. https://www.doi.org/10.1063/1.4992070 (2017).

53. Vool, U. & Devoret, M. Introduction to quantum electromagnetic circuits. *International Journal of Circuit Theory and Applications* **45,** 897–934. https://www.doi.org/10.1002/cta.2359 (2017).

54. Wallquist, M., Shumeiko, V. S. & Wendin, G. Selective coupling of superconducting charge qubits mediated by a tunable stripline cavity. *Physical Review B* **74,** 224506. https://www.doi.org/10.1103/PhysRevB.74.224506 (2006).

55. Tinkham, M. *Introduction to Superconductivity* 2nd ed. (Dover Publications Inc., New York, 1996).

56. Gross, R. & Marx, A. *Festkörperphysik* ISBN: 978-3-11-035870-4. https://doi.org/10.1524/9783110358704 (De Gruyter Oldenbourg, 2014).

57. Clarke, J. & Braginski, A. I. *The SQUID Handbook* (Wiley-VCH, 2004).

58. Pogorzalek, S. Hysteretic Flux Response and Nondegenerate Gain of Flux-Driven Josephson Parametric Amplifiers. *Physical Review Applied* **8.** https://www.doi.org/10.1103/PhysRevApplied.8.024012 (2017).

59. Groszkowski, P. & Koch, J. Scqubits: a Python package for superconducting qubits. *Quantum* **5,** 583. https://www.doi.org/10.22331/q-2021-11-17-583 (2021).

60. Pozar, D. M. *Microwave engineering* 4th ed. ISBN: 978-0-470-63155-3 (Wiley, Hoboken, NJ, 2012).

61. Saito, K. Temperature Dependence of the Surface Resistance of Niobium at 1300 MHz - Comparison to BCS Theory - (1999).

62. McRae, C. R. H. *et al.* Materials loss measurements using superconducting microwave resonators. *Review of Scientific Instruments* **91,** 091101. https://www.doi.org/10.1063/5.0017378 (2020).

63. Song, C. *et al.* Microwave response of vortices in superconducting thin films of Re and Al. *Physical Review B* **79,** 174512. https://www.doi.org/10.1103/PhysRevB.79.174512 (2009).

64. Bothner, D. *et al.* Reducing vortex losses in superconducting microwave resonators with microsphere patterned antidot arrays. *Applied Physics Letters* **100,** 012601. https://www.doi.org/10.1063/1.3673869 (2012).

65. Goetz, J. *et al.* Loss mechanisms in superconducting thin film microwave resonators. *Journal of Applied Physics* **119,** 015304. https://www.doi.org/10.1063/1.4939299 (2016).

66. Lisenfeld, J. *et al.* Electric field spectroscopy of material defects in transmon qubits. *npj Quantum Information* **5,** 105. https://www.doi.org/10.1038/s41534-019-0224-1 (2019).

67. Müller, C., Cole, J. H. & Lisenfeld, J. Towards understanding two-level-systems in amorphous solids: insights from quantum circuits. *Reports on Progress in Physics* **82,** 124501. https://www.doi.org/10.1088/1361-6633/ab3a7e (2019).

68. Martinis, J. M. *et al.* Decoherence in Josephson Qubits from Dielectric Loss. *Physical Review Letters* **95,** 210503. https://www.doi.org/10.1103/PhysRevLett.95.210503 (2005).

69. Probst, S., Song, F. B., Bushev, P. A., Ustinov, A. V. & Weides, M. Efficient and robust analysis of complex scattering data under noise in microwave resonators. *Review of Scientific Instruments* **86,** 024706. https://www.doi.org/10.1063/1.4907935 (2015).

70. Cuthbertson, B. D., Tobar, M. E., Ivanov, E. N. & Blair, D. G. Parametric back-action effects in a high-Q cyrogenic sapphire transducer. *Review of Scientific Instruments* **67,** 2435–2442. https://www.doi.org/10.1063/1.1147193 (1996).

71. LaHaye, M. D., Buu, O., Camarota, B. & Schwab, K. C. Approaching the Quantum Limit of a Nanomechanical Resonator. *Science* **304,** 74–77. https://www.doi.org/10.1126/science.1094419 (2004).

72. Regal, C. A., Teufel, J. D. & Lehnert, K. W. Measuring nanomechanical motion with a microwave cavity interferometer. *Nature Physics* **4,** 555–560. https://www.doi.org/10.1038/nphys974 (2008).

73. Rocheleau, T. *et al.* Preparation and detection of a mechanical resonator near the ground state of motion. *Nature* **463,** 72–75. https://www.doi.org/10.1038/nature08681 (2010).

74. Massel, F. *et al.* Microwave amplification with nanomechanical resonators. *Nature* **480,** 351–354. https://www.doi.org/10.1038/nature10628 (2011).

75. Etaki, S. *et al.* Motion detection of a micromechanical resonator embedded in a d.c. SQUID. *Nature Physics* **4,** 785–788. https://www.doi.org/10.1038/nphys1057 (2008).

76. Schmidt, P. *et al.* Sideband-resolved resonator electromechanics based on a nonlinear Josephson inductance probed on the single-photon level. *Communications Physics* **3,** 1–7. https://www.doi.org/10.1038/s42005-020-00501-3 (2020).

77. Bera, T., Majumder, S., Sahu, S. K. & Singh, V. Large flux-mediated coupling in hybrid electromechanical system with a transmon qubit. *Communications Physics* **4,** 1–7. https://www.doi.org/10.1038/s42005-020-00514-y (2021).

78. Luschmann, T. *et al.* Mechanical frequency control in inductively coupled electromechanical systems. *Scientific Reports* **12,** 1608. https://www.doi.org/10.1038/s41598-022-05438-x (2022).

79. Schmidt, P. *et al.* Remote sensing of a levitated superconductor with a flux-tunable microwave cavity. *Physical Review Applied* **22,** 014078. https://www.doi.org/10.1103/PhysRevApplied.22.014078 (2024).

80. Cleland, A. N. *Foundations of Nanomechanics: From Solid-State Theory to Device Applications* ISBN: 978-3-540-43661-4. https://link.springer.com/book/10.1007/978-3-662-05287-7 (Springer Berlin, 2003).

81. Heinrich, S. M. & Dufour, I. in *Resonant MEMS* 1–28 (John Wiley & Sons, Ltd, 2015). ISBN: 978-3-527-67633-0. https://doi.org/10.1002/9783527676330.ch1.

82. *2.1.6 Effective mass and eigenfrequency of the cantilever* https://www.ntmdt-si.com/resources/spm-theory/theoretical-background-of-spm/2-scanning-force-microscopy-(sfm)/21-cantilever/216-effective-mass-and-eigenfrequency-of-the-cantilever.

83. *AFM Probes - BudgetSensors* https://www.budgetsensors.com/afm-probes.

84. Farrokh Payam, A. & Fathipour, M. Study of the tip mass and interaction force effects on the frequency response and mode shapes of the AFM cantilever. *The International Journal of Advanced Manufacturing Technology* **65,** 957–966. https://www.doi.org/10.1007/s00170-012-4231-z (2013).

85. Finnemore, D. K., Stromberg, T. F. & Swenson, C. A. Superconducting Properties of High-Purity Niobium. *Physical Review* **149,** 231–243. https://www.doi.org/10.1103/PhysRev.149.231 (1966).

86. Balshaw, N. H., Oxford Instruments Group & Scientific Research Division. *Practical cryogenics: an introduction to laboratory cryogenics* ISBN: 978-0-9527594-0-9 (Oxford Instruments, Scientific Research Division, Eynsham, 1996).

87. Batey, G. & Teleberg, G. *Principles of dilution refrigeration* 2015. https://nanoscience.oxinst.com/assets/uploads/NanoScience/Brochures/Principles%20of%20dilution%20refrigeration_Sept15.pdf.

88. Rieger, D. *et al.* Fano Interference in Microwave Resonator Measurements. *Physical Review Applied* **20,** 014059. https://www.doi.org/10.1103/PhysRevApplied.20.014059 (2023).

89. Daser, J. *Fabrication and characterization of Manhattan Style Josephson Junctions for superconducting quantum bits* MA thesis (University of Innsbruck, 2024). https://ulb-dok.uibk.ac.at/urn/urn:nbn:at:at-ubi:1-145406.

90. Muthusubramanian, N. *et al.* Wafer-scale uniformity of Dolan-bridge and bridgeless Manhattan-style Josephson junctions for superconducting quantum processors. *Quantum Science and Technology* **9,** 025006. https://www.doi.org/10.1088/2058-9565/ad199c (2024).

91. Brock, B. L., Blencowe, M. P. & Rimberg, A. J. Frequency Fluctuations in Tunable and Nonlinear Microwave Cavities. *Physical Review Applied* **14,** 054026. https://www.doi.org/10.1103/PhysRevApplied.14.054026 (2020).

92. Kurpiers, P., Walter, T., Magnard, P., Salathe, Y. & Wallraff, A. Characterizing the attenuation of coaxial and rectangular microwave-frequency waveguides at cryogenic temperatures. *EPJ Quantum Technology* **4,** 1–15. https://www.doi.org/10.1140/epjqt/s40507-017-0059-7 (2017).

93. *All-In-One-Tipless AFM Probe - BudgetSensors* https://www.budgetsensors.com/multipurpose-afm-probe-no-tip-all-in-one-tipless.

94. Potticary, J., Avery, M. P., Mills, D. & Hall, S. R. DONALD: A 2.5 T wide sample space permanent magnet. *HardwareX* **3,** 39–48. https://www.doi.org/10.1016/j.ohx.2018.01.002 (2018).

95. Henins, I. Precision density measurement of silicon. *Journal of Research of the National Bureau of Standards Section A: Physics and Chemistry* **68A,** 529. https://www.doi.org/10.6028/jres.068A.050 (1964).

96. Hopcroft, M. A., Nix, W. D. & Kenny, T. W. What is the Young's Modulus of Silicon? *Journal of Microelectromechanical Systems* **19,** 229–238. https://www.doi.org/10.1109/JMEMS.2009.2039697 (2010).

97. *Custom Rare Earth Magnets* https://www.advancedmagnets.com/custom-magnets/.

98. Yasumura, K. *et al.* Quality factors in micron- and submicron-thick cantilevers. *Journal of Microelectromechanical Systems* **9,** 117–125. https://www.doi.org/10.1109/84.825786 (2000).

99. Imboden, M. & Mohanty, P. Dissipation in nanoelectromechanical systems. *Physics Reports. Dissipation in nano-electromechanical systems* **534,** 89–146. https://www.doi.org/10.1016/j.physrep.2013.09.003 (2014).

100. Liu, Z. Temperature-Dependent Elastic Constants and Young's Modulus of Silicon Single Crystal. *Proceedings of the 11th Mechanical Engineering Design of Synchrotron Radiation Equipment and Instrumentation* **MEDSI2020.** https://www.doi.org/10.18429/JACOW-MEDSI2020-WEPC09 (2021).

101. *Read more about Neodymium magnets* https://www.euromag-magnets.com/en/neodymium-characteristics/.

102. Gorodetksy, M. L., Schliesser, A., Anetsberger, G., Deleglise, S. & Kippenberg, T. J. Determination of the vacuum optomechanical coupling rate using frequency noise calibration. *Optics Express* **18,** 23236–23246. https://www.doi.org/10.1364/OE.18.023236 (2010).

103. Calatroni, S. *Materials & Properties: Thermal & Electrical Characteristics* 2020. https://www.doi.org/10.48550/arXiv.2006.02842.

104. Ekin, J. *Experimental Techniques for Low-Temperature Measurements: Cryostat Design, Material Properties and Superconductor Critical-Current Testing* ISBN: 978-0-19-857054-7. https://doi.org/10.1093/acprof:oso/9780198570547.001.0001 (Oxford University Press, 2006).

105. Buzea, C. & Robbie, K. Assembling the puzzle of superconducting elements: a review. *Superconductor Science and Technology* **18,** R1. https://www.doi.org/10.1088/0953-2048/18/1/R01 (2004).

106. Bardeen, J., Rickayzen, G. & Tewordt, L. Theory of the Thermal Conductivity of Superconductors. *Physical Review* **113,** 982–994. https://www.doi.org/10.1103/PhysRev.113.982 (1959).

107. Valois, J. J., Nellis, G. F. & Pfotenhauer, J. M. Characterization of the thermal properties of OFHC copper at cryogenic temperature. *IOP Conference Series: Materials Science and Engineering* **1301,** 012167. https://www.doi.org/10.1088/1757-899X/1301/1/012167 (2024).

108. Tariq, A. & Asif, M. Experimental investigation of thermal contact conductance for nominally flat metallic contact. *Heat and Mass Transfer* **52,** 291–307. https://www.doi.org/10.1007/s00231-015-1551-1 (2016).

109. *Richtwerte für metrisches Regelgewinde VDI 2230* https://www.bossard.com/de-de/assembly-technology-expert/technische-informationen-und-tools/technische-informationen/vorspannkraefte-und-anziehdremomente/richtwerte-fuer-metrisches-regelgewinde-vdi-2230/.

110. Dhuley, R. C. Pressed copper and gold-plated copper contacts at low temperatures – A review of thermal contact resistance. *Cryogenics* **101,** 111–124. https://www.doi.org/10.1016/j.cryogenics.2019.06.008 (2019).

111. Gmelin, E., Asen-Palmer, M., Reuther, M. & Villar, R. Thermal boundary resistance of mechanical contacts between solids at sub-ambient temperatures. *Journal of Physics D: Applied Physics* **32,** R19. https://www.doi.org/10.1088/0022-3727/32/6/004 (1999).

112. Dillon, A., McCusker, K., Van Dyke, J., Isler, B. & Christiansen, M. Thermal interface material characterization for cryogenic electronic packaging solutions. *IOP Conference Series: Materials Science and Engineering* **278,** 012054. https://www.doi.org/10.1088/1757-899X/278/1/012054 (2017).

113. Dhuley, R. C., Ruschman, M., Link, J. T. & Eyre, J. Thermal conductance characterization of a pressed copper rope strap between 0.13 K and 10 K. *Cryogenics* **86,** 17–21. https://www.doi.org/10.1016/j.cryogenics.2017.07.001 (2017).

114. Herbst, J. F. R 2 Fe 14 B materials: Intrinsic properties and technological aspects. *Reviews of Modern Physics* **63,** 819–898. https://www.doi.org/10.1103/RevModPhys.63.819 (1991).

115. Rong, C.-b., Poudyal, N. & Liu, J. P. Size-dependent spin-reorientation transition in Nd2Fe14B nanoparticles. *Physics Letters A* **374,** 3967–3970. https://www.doi.org/10.1016/j.physleta.2010.07.061 (2010).

116. Kou, X. C., Dahlgren, M., Grössinger, R. & Wiesinger, G. Spin-reorientation transition in nano-, micro- and single-crystalline Nd2Fe14B. *Journal of Applied Physics* **81,** 4428–4430. https://www.doi.org/10.1063/1.364791 (1997).

117. Diez-Jimenez, E. *et al.* Magnetic and morphological characterization of Nd2Fe14B magnets with different quality grades at low temperature 5–300 K. *Journal of Magnetism and Magnetic Materials* **451,** 549–553. https://www.doi.org/10.1016/j.jmmm.2017.11.109 (2018).

118. Zhang, Z.-H. *et al.* Acceptor-Induced Bulk Dielectric Loss in Superconducting Circuits on Silicon. *Physical Review X* **14,** 041022. https://www.doi.org/10.1103/PhysRevX.14.041022 (2024).

119. Kamppinen, T., Mäkinen, J. T. & Eltsov, V. B. Dimensional control of tunneling two-level systems in nanoelectromechanical resonators. *Physical Review B* **105,** 035409. https://www.doi.org/10.1103/PhysRevB.105.035409 (2022).

120. Liu, Y.-C., Xiao, Y.-F., Luan, X., Gong, Q. & Wong, C. W. Coupled cavities for motional ground-state cooling and strong optomechanical coupling. *Physical Review A* **91,** 033818. https://www.doi.org/10.1103/PhysRevA.91.033818 (2015).

121. Guo, J. & Gröblacher, S. Coherent feedback in optomechanical systems in the sideband-unresolved regime. *Quantum* **6,** 848. https://www.doi.org/10.22331/q-2022-11-03-848 (2022).